THE TIMELESS TALE OF SAND IN AN HOURGLASS: MATHEMATICAL MODELLING OF GRANULAR FLOW IN A SILO.

A thesis presented in partial fulfilment of the requirements for the degree of

Doctor of Philosophy

in

Mathematics

at Massey University, Palmerston North,

New Zealand.

Samuel Kyle Irvine

2024

Contents

List of Tables

List of Figures

Abstract

Granular materials are an integral part of many processes vital to both nature and modern life. Improving our understanding of the behaviour of flowing granular materials is important for a wide variety of applications. Many models have attempted to capture the dynamics of granular flow, including discrete element models which model individual particles, models which analyse the stress in granular material, and models using the Navier-Stokes equation. Each of these models have various advantages and disadvantages, and while they each can be used to give unique insights into granular flows, no currently available model fully captures the multitude of phenomena that granular materials exhibit. This thesis focuses on the $\mu(I)$ model within silos, extending the model to capture more of the complexities of granular flow.

In this thesis, the $\mu(I)$ model is extended in a variety of ways. While the base $\mu(I)$ model is incompressible, granular material dilates while flowing. This work extends the $\mu(I)$ model to be pseudo-compressible. Another consideration is that the $\mu(I)$ model is also a purely local model. In contrast, experiments done with flows down slopes and in Couette cells have shown that granular materials exhibits nonlocal behaviour. To account for this, this work applies nonlocal fluidity to the $\mu(I)$ model. Finally, granular materials are often composed of many components, each with potentially different material parameters, so a model is developed to allow for multiple material types mixing within a silo.

The interaction of these effects are tested within complex domains including the double opening silo. The double opening silo is analysed, with the $\mu(I)$ model capable of replicating the 'flow rate dip' behaviour seen in DEM and physical experiments. The extensions to the $\mu(I)$ model also improve the dipping behaviour, allowing for greater replication of physical behaviour. These extensions are also applied to silos with inserts, where the model shows strong improvements in material mobility are possible within a silo with even small inserts.

The gestalt $\mu(I)$ model and the conclusions drawn within this thesis provide valuable insights for a variety of essential industrial and scientific fields, and pushes forward our collective understanding of continuum modelling for granular flow.

Acknowledgements

Firstly, I would like to thank my supervisors: Luke Fullard, Thomasin Lynch, Daniel Holland, and Daniel Clarke. Your insights into granular flow have enabled to me to understand this field, your helpful comments have made it possible for me to communicate my ideas clearly, and your constant encouragement has enabled me to finish this work. Thank you.

I would also like to thank Stéphane Popinet and other developers of Basilisk. This software enabled the bulk of the simulations done in this thesis, and this work is standing on the shoulders you have built. I would particularly like to acknowledge Pierre-Yves Lagrée, who helped introduce me to this software and explained many of the challenges that I faced throughout this work.

The Massey mathematics department as a whole has been a key part of my mathematical career. I would like to thank everyone who grew my knowledge in mathematics, encouraged my interest, and provided appropriate challenges. I would also like to thank them and associated organisations for the scholarships I have received and employment I have benefited from across my time as a student. I would also like to acknowledge the flexibility to finish my PhD while working afforded to me by Michaela Rose and Brent Watson at Horizons.

I would also like to thank the various student communities I have been part of during my time as a postgraduate. In particular, I would like to thank all the members of the Journal club, who helped me to understand many of the challenges of writing clear papers and communicating well.

Finally, for my family, friends, and fiancée; thank you for your encouragement, your patience, and your love.

Nomenclature

All constants and variables are used in this thesis are defined when they first appear in the text. For reference, these variables are named in the list below. In addition to symbols being associated with different quantities, a few additional points of notation should be clarified.

A bold symbol indicates a vector or tensor quantity. The quantity $\boldsymbol{a_g}$ indicates the gravity associated with a direction, while a_g indicates only the magnitude.

For tensors, the Einstein summation convention is used. For a tensor $\dot{\boldsymbol{\epsilon}}$, then a repeated index for an element of that tensor $\dot{\epsilon}_{ii}$ indicates a sum of all relevant repeated indices, i.e. $\dot{\epsilon}_{ii} = \dot{\epsilon}_{xx} + \dot{\epsilon}_{yy}$ for a $2D$ system. The tensor norm is calculated as

$$|\dot{\gamma}| = \sqrt{\frac{\dot{\gamma}_{ij}\dot{\gamma}_{ij}}{2}}, \tag{1}$$

The stress tensor $\boldsymbol{\sigma}$ with elements σ_{ij} has a few related attributes. The pressure P can be calculated as $P = \frac{1}{2}\sigma_{ii}$ for $2D$ domains and $P = \frac{1}{3}\sigma_{ii}$ for $3D$ domains, and the shear stress tensor $\boldsymbol{\tau}$ can be calculated as $\boldsymbol{\tau} = \boldsymbol{\sigma} - P\boldsymbol{I}$, where $\boldsymbol{I}$ is the identity tensor. The normal stress σ and shear stress τ could be referred to as only the magnitude in situations where only a specific axis is considered.

A dot accent on a symbol indicates a time derivative. Given velocity u, the acceleration could be represented as $\dot{u}$.

A circumflex accent on a symbol indicates the symbol is in another vector basis. Velocity $\boldsymbol{u}$ may represent the velocity in xy-coordinates, while $\hat{\boldsymbol{u}}$ represents the velocity in some other coordinate set.

A tilde accent on a symbol indicates a normalised value. A length L might be relevant only by comparison to some other distance d, so a normalised $\tilde{L} = L/d$ instead

a_g	Acceleration due to gravity
A	Nonlocal strength parameter
B	Kinematic model parameter
c	Tracer
c_o	Cohesion

C	Beverloo-Hagen flow rate parameter
d	Particle diameter
$\boldsymbol{d_s}$	Stochastic spot drift direction
$\mathbf{D}$	Strain rate tensor
$E(t)$	Residence time distribution
$\boldsymbol{F}$	Force vector
$F(t)$	Cumulative distribution
g	Granular fluidity
g_l	Local granular fluidity
I	Inertial number
I_0	Parameter of $\mu(I)$ model, Inertial transition
$\boldsymbol{I}$	Identity matrix
k	Beverloo-Hagen flow rate parameter
L	Two opening silo separation distance
L_s	Stochastic spot diameter
m	Mass
$\boldsymbol{p}$	Momentum vector
P	Pressure
$\boldsymbol{q}$	Deviatoric stress tensor
Q	Silo flow rate
Q_0	Two opening silo flow rate for degenerate zero separation case
r	Radius
t_s	Stochastic time scale
T_g	Granular temperature
$\boldsymbol{u}$	Velocity vector
V_λ	Weighting function normalisation constant
W	Silo opening diameter
W_d	Distance between front and back wall for pseudo-2D silo
$W(r)$	Weighting function on radius r

W_s	Width of the silo
α	Angle of repose
α_w	Effective angle of repose at wall
$\dot{\gamma}$	Shear rate
$\dot{\epsilon}$	Direct strain rate
η	Viscosity
$\eta_{\max}$	Maximum viscosity for regularisation
θ	Angle
λ	Characteristic length
λ_μ	Stress strain constant
μ	Coefficient of friction
μ_s	Parameter of $\mu(I)$ model, static friction component
μ_w	Coefficient of friction between wall and granular material
$\Delta\mu$	Parameter of $\mu(I)$ model, dynamic friction component
ρ	Density
ρ_b	Bulk density
ρ_s	Stochastic spot density
σ	Normal stress
σ_{maj}	Major normal stress from Mohr circle
$\sigma_{\min}$	Minor normal stress from Mohr circle
τ	Shear stress
ϕ	Packing fraction
$\phi_{\max}$	Undilated packing fraction
$\phi_{\min}$	Minimum packing fraction
ϕ_g	Dilatancy strength
ψ^*	Principal stress angle
Ω	Entire modelled domain

Chapter 1

Introduction

Sand, soil, salt, and seeds are all examples of granular materials encountered in everyday life. More precisely, granular materials are collections of many solid particles where interactions between particles lead to loss of kinetic energy. These powders, grains, soils, and other materials are essential to nature and human activity, with an estimated 10% of energy consumption worldwide being used to process granular materials [43]. Modelling these materials is essential to many areas of science and industry, and although several models exist that capture particular areas of granular mechanics these materials exhibit complex phenomena that make fully capturing their complicated behaviour difficult.

Granular materials can exhibit behaviour similar to solids, liquids, or gases depending on the forces applied to them. Early work done by Coulomb focused on understanding the stress and yield conditions of stationary 'solid-like' granular materials, seeking to prevent soil movement around structures [36, 110]. These principles were utilised by Jenike to understand mechanics of flowing 'liquid-like' granular material in a radial silo [90]. Analysis has also been done for 'gaseous-like' granular materials where long interactions between granules become rare, such as found in Saturn's rings [23, 70]. This work focuses on understanding the 'liquid-like' phase of granular flows, where the granular material is yielding yet still relatively dense in the area. The various states of granular flow are discussed in more detail in Section 2.2

Silos and silo-like domains are widely used in a variety of industrial applications, most notably in agriculture and mining. Silos also represent a complex domain where material can exhibit a

variety of phenomena that can be difficult to model accurately. In different locations within a single draining silo, the granular material could be exhibiting solid-like behaviour in the corners of the silo or the center of a 'plug' flow, liquid-like behaviour in the majority of the silo where the granular material is shearing as it approaches the orifice, and gaseous-like behaviour as the orifice is reached and the granules begin to fall freely with fewer interactions between particles. These dynamics can mean that many granular models are unsuitable for silos. Silos also exhibit nonlocal effects [42], dilatancy [113], segregation [154], and other phenomena that are frequently absent in models.

A basic granular silo is some contained volume of granular material with a single opening at the base, which is allowed to drain under gravity. Factors which can further complicate the already complex dynamics within the silo include: multiple openings from which the material can drain, inserts used to improve mixing or flow behaviours, and heterogeneous material loaded into the silo. For example, under certain conditions a silo with two openings can exhibit a 'flow rate dip', where the flow rate for the case with a small separation between openings is slower than the flow rate for both the case with no separation (i.e. a single large orifice) and a double orifice case with a large separation between the openings [50]. Multiple openings are covered in more detail in Section 4, inserts in Section 5, and heterogeneous material in Section 6.

Many models have been applied to granular flows, with the majority of models falling into one of two categories - discrete element modelling (DEM) or continuum modelling. Discrete element models track the motion of each granule individually, modelling collisions between each particle and letting the aggregate motion form in the same manner that practical flows do. This method is powerful and widely used in many applications, and gives many useful results. However discrete element modelling is highly computationally expensive. With powerful modern computers and sufficient time millions of particles can be simulated; however, many industrial and natural processes involve on the order of billions of particles. DEM models are examined more rigorously in Section 3.1.

The alternative to discrete element models is continuum models, such as the aforementioned radial model [90], kinematic model [129, 132], stochastic model [99, 102], and $\mu(I)$ model [125, 111]. Continuum models imagine the granular material as a continuous 'fluid' rather than

as discrete particles, modelling the aggregate flow directly. While these powerful models can each give useful insights into granular flows with much less computational overhead than discrete element models, they fail to fully capture the full dynamics of granular flows. Various continuum model are described in Section 3.2 onwards.

Many continuum models have a flow rate which is determined by a single parameter, either by directly inputting the expected flow rate or by choosing characteristic lengths and times. Of the continuum models examined in this work, only the $\mu(I)$ model has a flow rate that can not be determined by modifying a single parameter without affecting other aspects of the flow, and as such can give flow rate predictions. This thesis focuses on the $\mu(I)$ model, testing the capability of this model within a silo. The basic $\mu(I)$ model does not account for a variety of granular phenomena, including dilatancy, nonlocal effects, and components with different physical properties. This work extends the $\mu(I)$ model to account for these effects, and tests this enhanced model in complex domains such as the double slot silo and silos with inserts. Section 3.5 covers the $\mu(I)$ model more completely, with Section 3.6 explaining the extensions.

This thesis begins with a review of existing knowledge, with Chapter 2 covering some of the many phenomena that granular materials can exhibit and Chapter 3 covering a selection of dense granular flow models. These models are then applied to the granular silo and the double slot granular silo in Chapter 4, discussing which phenomena are needed to capture the complex flow behaviour exhibited in these domains. It is shown that the base $\mu(I)$ model predicts the expected behaviour of the Beverloo-Hagen relation and the double silo flow rate dip, which is further refined by the addition of dilatancy, nonlocal effects, and Hele-Shaw wall friction. In Chapter 5 the $\mu(I)$ model is applied to silos with inserts, finding that dilatancy and nonlocal effects are crucial for determining regions of the silo in which the flow is slow moving or static. Finally, in Chapter 6 the mixing behaviour of silos is analysed, showing that the shape of the domain is crucial for finding the mixing dynamics of a silo. It is also shown that granular materials with multiple components that have differing properties can have significantly different flow behaviour, which could impact the dynamics of segregation as well as industrial processes involving combining different sources of materials.

The $\mu(I)$ model is an existing model that has been applied to silos [125], and the non-local,

dilatancy, and Hele-Shaw wall friction extensions have previously been developed. The double slot silo has been examined experimentally and using DEM [50, 181]. The original contribution of this work includes combining these extensions, as well as applying them to the silo. Examining the double slot silo using a continuum model is novel, as well as the examination of the effect of different extensions and their parameters. Examination of silos with inserts using a continuum model also appears to be novel. Finally, the two component model with different material properties is also original.

Chapter 2

Properties of granular flow

This chapter discusses the general mechanics of granular material and the resulting phenomena displayed in different granular systems. Many mechanics of standard fluids also apply to granular flows and as such comparisons will be drawn often. Nonetheless, there are some key differences that lead to some counter-intuitive results.

The focus is on treating granular material as a continuum, with emphasis on a silo or silo-like domains. Some interactions at the granular level are examined, however the focus is on the applicability to the large-scale phenomena relevant to modelling granular materials as a continuum. Contact forces are discussed in detail in Section 3.1, though discussion of phenomena like force chains [140, 76] are omitted as they are outside the scope of this thesis.

2.1 Yield stress

When stresses are applied to a fluid, it begins to deform. For a Newtonian fluid, the deformation rate scales linearly with the shear stress applied, with the proportionality constant being the viscosity of the fluid. Some fluids are shear-thinning (such as paint) or shear-thickening (such as Ooblek), meaning their effective viscosity decreases or increases respectively as greater shear stress is applied. For each of these fluids, any net force will cause some deformation [83].

By contrast, granular materials do not deform if a small shear stress is applied. Granular material will resist deformation when any stress below a critical stress, known as the "yield

stress", is applied. Beyond this stress, granular material will flow analogously to a fluid, although the effective viscosity can take a more complicated form than the linear response of a standard fluid [133, 111].

An apt analogy for yield stress is friction. An object at rest on a table will not move if a light force is applied, but once the force exceeds the static friction the object will accelerate at a rate linearly related to the magnitude of the force. Similarly for a granular material, if the shear stress, τ, does not exceed the yield stress (given by $\mu\sigma$, where μ is the friction coefficient and σ is the normal stress) of the material, no deformation occurs. When the yield condition is met, i.e. $\tau \geq \mu\sigma$, the result is a visco-plastic flow [96].

When analysing whether the yield condition is met, it is important to consider that granular material does not just have one plane along which deformation might occur. Consider the soil under a building: there is confining pressure equally applying to each of the sides from the surrounding earth, and there is a larger confining stress from the load of the building above. If a horizontal plane is considered there is no shear stress, and as such it would seem that the soil could bear an arbitrarily heavy load. When we consider angled planes however, the soil fails at some finite load even though the material will not fail along the horizontal plane. This is covered in more detail in Section 3.2 and Appendix A, with a short description given here.

To examine the statics of granular material we consider a simple $2D$ case illustrated in Figure 2.1. In this case there is a compressive horizontal stress σ_{xx} and a greater vertical stress σ_{zz} with no shear stress τ_{xy}. When examining a line at angle θ to the horizontal plane, Nedderman [133] shows there is an effective shear and normal stress of

$$\sigma_\theta = \frac{1}{2}(\sigma_{xx} + \sigma_{zz}) + \frac{1}{2}(\sigma_{zz} - \sigma_{xx})\cos(2\theta), \tag{2.1}$$

$$\tau_\theta = \frac{1}{2}(\sigma_{zz} - \sigma_{xx})\sin(2\theta). \tag{2.2}$$

We then have the yield criterion which tells us that slip occurs along the line if $\tau_\theta \geq \mu\sigma_\theta$. Since any angled plane is a possible slip plane, we must consider planes at all possible angles, and find which maximises shear stress relative to normal stress. If and only if this line meets the yield

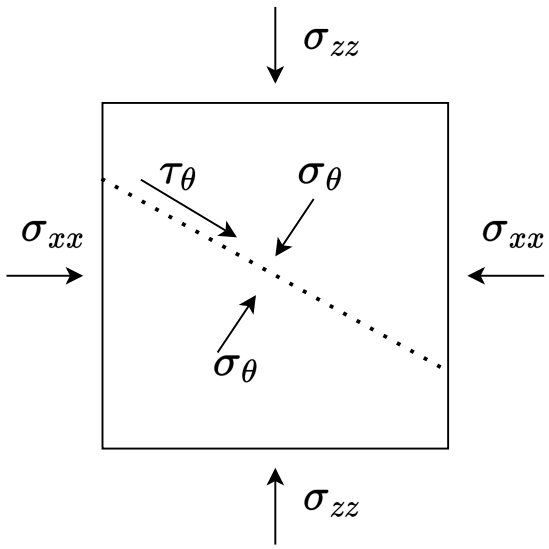

Figure 2.1: An illustration of shear stress introduced by normal stress. Even though along the xz-axis there is no shear stress, along a line at angle θ from horizontal there is an effective shear stress τ_θ.

criterion will the material deform. The point at which yield occurs is then

$$\sigma_{zz} \geq \Big(\frac{1+\mu}{1-\mu}\Big)\sigma_{xx}. \tag{2.3}$$

In cases where there is shear stress in addition to compressive stresses, a change of coordinates can be found in which all the shear stresses are eliminated and as such Equation 2.3 can also be applied. Doing this analysis for all possible coordinate choices results in what is called a Mohr circle [133]. A similar process can be applied for a $3D$ volume, where the correct choice of coordinates gives three 'principal stresses', with the largest and smallest principal stresses producing the yield condition when substituted into Equation 2.3. Further discussion of Mohr circles and the derivation of Equation 2.3 can be found in Appendix A.

One result of this yield stress is that when poured into a pile, granular material will form a cone with angle α called the angle of repose. When the pile is steeper than α, gravity causes the yield criterion to be met and material will cascade down the slope. The angle of repose, α, is related to the yield condition by $\mu = \tan(\alpha)$. It can also be the cause of some more complicated behaviour in a silo, where some zones are stagnant, while other zones flow freely [133].

It is important to note that flow can occur in locations where the yield condition is not met. Granular material can form a block of material which flows as a coherent mass with no shear in the inside of this block. In a silo this causes 'mass flow', where the center of the silo is mobilised but the shear occurs only in the sides of the silo [161].

2.2 States of granular flow

Granular material can be thought of as having properties of a fluid and a solid, with different properties being exhibited when different forces are applied. When shear stress is low relative to the confining stress, the granular material does not yield, and exhibits solid-like behaviour. An example of this is when walking on sand; the sand is capable of bearing the weight of a person and one experiences the sand to be fairly solid. If the sand acted as a liquid then people would sink to the point of neutral buoyancy. With a moderate shear stress relative to the confining stress, the granular material acts more like a liquid. This results in phenomena such as being able to 'pour' sand out of a cup. When shear stress is high relative to the confining stress, the granular material can enter a gas-like state. To determine whether a given material will exhibit 'solid-like', 'liquid-like', or 'gas-like' features, a widely used way of classifying the state of the flow is the dimensionless 'inertial number' [82, 38]. The inertial number (which is the square of the Savage number [155]) arises from dimensional analysis performed on a simple shear cell [5]. The inertial number is given by

$$I = \frac{\dot{\gamma} d}{\sqrt{P/\rho}}, \tag{2.4}$$

where $\dot{\gamma} = \sqrt{D_{ij} D_{ij}}$ is the norm of the strain rate tensor $\boldsymbol{D}$ with elements D_{ij}, d is the particle diameter, $P = \sigma_{ii}$ is the confining pressure, and ρ is the material density [125]. Low I (i.e. as $I \to 0$) is called the quasi-static limit and can be thought of as the 'solid' regime with plastic deformations. High I (i.e. $I \gtrapprox 1$) is the kinetic or 'gaseous' regime where particles move past each other relatively easily. In between these two extremes, moderate values for I indicate the dense or 'liquid' regime. It should be noted that these are not formally defined regimes, and do not have clear transitions in intermediate values.

The value of the inertial number can be interpreted as a ratio of two timescales, the microscopic timescale $d/\sqrt{P/\rho}$ and the macroscopic timescale, $\dot{\gamma}^{-1}$. The microscopic timescale represents the time taken for rearrangements to occur, while the macroscopic timescale represents the time taken for deformations to occur [5]. When the microscopic timescale is dominant, corresponding to low I, granules are forced into contacting other particles and 'solid' features occur. When the macroscopic timescale is dominant, corresponding to high I, granules move past each other easily and 'gaseous' features occur.

2.2.1 Quasi-Static regime

When a granular material is flowing slowly relative to the speed of grain rearrangements due to confining pressure ($I \to 0$), the flow is called quasi-static. The quasi-static regime is an important and long studied part of granular flow [146]. Two important areas of investigation in this regime are understanding what forces a static granular material can resist before yielding, and understanding the slow plastic deformations that can occur when these forces are applied. These factors are particularly applicable to soil, where engineers need to understand the load-bearing capability of land used for construction projects.

A model often used in this regime is the Mohr-Coulomb model [133]. This model takes the yield condition given by Equation 2.3 and makes the assumption that at every point the material is at minimum shear stress where yield is possible. This is called 'incipient yield' and is given by $\tau = \mu\sigma$. From this relation, a plasticity rule can be defined to give the dynamics of a material undergoing stress. The strain of the material is assumed to be linearly related to the deviatoric stress $\boldsymbol{\tau}$, which is the stress $\boldsymbol{\sigma}$ of the material less the pressure P. This is known as a coaxial flow rule [133] and gives the relation

$$\dot{\boldsymbol{\epsilon}} = \lambda_\mu \boldsymbol{\tau} = \lambda_\mu(\boldsymbol{\sigma} - P\boldsymbol{I}) \tag{2.5}$$

with some constant λ_μ and identity matrix $\boldsymbol{I}$. This flow rule can be thought of as the material expanding along the minor principal stress axis (the smallest normal stress), and contracting along the major principal stress axis (the largest normal stress).

Taking the norm of Equation 2.5, the value of λ_μ can be found to be $||\dot{\boldsymbol{\epsilon}}||/||\boldsymbol{\tau}||$. Either the Mohr-Coulomb or Drücker-Prager criterion can be used. The Drücker-Prager is chosen for convenience. By assuming the Drücker-Prager criterion [41, 5], the deviatoric stress can be found to be $||\boldsymbol{\tau}|| = \mu P$, which results in the relation

$$\boldsymbol{\tau} = \mu \frac{\dot{\boldsymbol{\epsilon}}}{||\dot{\boldsymbol{\epsilon}}||} P, \tag{2.6}$$

which when combined with the incompressibility assumption $\dot{\epsilon}_{ii} = 0$ defines a plasticity flow rule.

This plasticity flow rule results in a flow that is rate independent. Unlike a Newtonian fluid, where λ_μ is constant, the form of λ_μ means that doubling the shear will double the flow velocity, without otherwise affecting the flow behaviour.

The plasticity model is not without problems however. Some issues are:

- The coaxial flow rule predicts absurd results in some limit cases, such as the 'active' 2D silo [102].
- The assumption of incipient yield at every point is questionable across an entire silo, or other complex domain.
- The predictions of rate independence only hold for relatively slow flows (with faster flows entering the dense or dilute regimes).

Nonetheless this plasticity model has been widely used, especially for soil mechanics, proving accurate enough for many applications of quasi-static flow.

2.2.2 Dilute regime

When a granular flow is flowing rapidly compared to its confining pressure ($I \gtrapprox 1$), it is considered to be in the dilute regime [5]. One model describes dilute flow as taking the form of the Navier-Stokes equations, but with an extra term in the energy equation to account for the dissipation of energy by inelastic collisions [70]. However, this model does assume that the particles

are relatively densely packed, and is not appropriate for when the packing fraction significantly deviates from the static packing fraction [5].

Another model, the kinetic theory of granular flow, better models less dense flow [117, 5]. The kinetic theory is based on the Boltzmann equations and treats dilute granular flow similarly to an ordinary gas, however 'granular temperature' is used instead of regular thermodynamic temperature. In the same way that thermodynamic temperature represents the energy of the random motions of molecules, granular temperature T_g represents the energy of the random motion of granules, given by $T_g = \langle u'^2 \rangle$, where u' is the deviation from the mean flow velocity, and $\langle\ \rangle$ represents taking an average over an appropriate domain [25].

An important distinction from standard gas thermodynamic theory is that dilute granular flow is not assumed to have elastic collisions. In a standard gas, collisions between particles do not raise the temperature, with kinetic energy of the system and thermal energy being indistinguishable. Because collisions in a dilute granular flow are not perfectly elastic, some energy is dissipated as heat. Granules are relatively large compared to ordinary gas molecules, and as such the fluctuations of velocity resulting from heat are negligible. These factors result in kinetic energy being lost from the granular system.

The kinetic theory of granular flow has been successfully applied in a variety of situations, such as fluidised beds, granular jets, and Saturn's rings [157, 79, 80]. However, kinetic theory is based on the assumption that collisions are instantaneous or near-instantaneous. This works well in fluidised systems or systems with little constraining pressure, however many granular systems involved prolonged contact between granules. This limits the usefulness of this theory to applications where the granular material is predominately in the 'dilute' state.

2.2.3 Dense regime

When a granular flow is flowing rapidly compared to its confining pressure, the flow is said to be in the 'dense' regime. Dense flows are found in a variety of situations. Agricultural product storage, pharmaceutical production, and mining are examples of industrial operations in which granular material is processed in the dense regime. In particular, flow in silo-like domains is mostly in the dense regime.

Some examples of experiment set ups that can display dense granular flow are: planar shear, annular shear, vertical chute flow, inclined plane, heap flow, and rotating drum. Many mathematical models have been developed in an attempt to describe granular flow in each of these experimental setups. Some models are single purpose, only suiting a particular domain such as the radial and kinematic models which apply to the silo [132, 90]. A comprehensive model displaying all of the necessary phenomena for modelling complex dense granular flow has yet to be designed, though the $\mu(I)$ model is a promising base model [125]. As this is the focus of this work this regime is given more detail in Section 3, where some of the existing models which have been developed are described in more detail.

2.3 Nonlocal effects

Local flows are flows that are determined solely by the state at any given point. If the relevant properties (such as stress) are known at a point, then how the material flows at that point can be determined and does not depend on the flow in nearby regions. In contrast, granular flows can exhibit 'nonlocal effects', where the behaviour at a point is reliant on the flow characteristics at nearby points [153, 98].

One domain where nonlocal effects can be observed is in a flow down a slope [5, 144, 153]. If granular flows were purely local, then there would be a specific slope θ above which flow would occur and below which flow would not occur (potentially related to the angle of repose). Instead, the flow exhibits hysteresis, with a greater angle required to start flow down a slope than to stop a flow. Experiments show that there are two distinct angles $\theta_{\text{stop}} < \theta_{\text{start}}$, between which the material can either flow or remain stationary. If the slope is above θ_{start}, then flow will always occur, and if the slope is lowered, flow will continue to occur until the slope hits θ_{stop}. If the slope is below θ_{stop}, flow will not occur, and if the slope is raised then flow will only occur when raised to the angle θ_{start}. In this way, the behaviour of slopes of angles between θ_{stop} and θ_{start} are not solely determined by conditions at the point; if nearby granules are flowing, then stationary granules may be excited into motion.

Nonlocal effects can also be seen in annular shear, where an annulus is filled with granular

material and either the inner or outer wall is rotated with respect to the other [66, 101, 145]. In a wide channel with high shear rate a local model may give an accurate prediction. However if the shear rate is low, local models fail to give accurate predictions. In the quasi-static limit, where the shear rate approaches 0, a purely local model predicts an infinitely thin shear zone (equivalent to slipping at the wall). However, experiments show that for very low shear rates there is still a relatively wide zone where shear occurs. Nonlocal effects could also be important for a silo. Silos can contain areas which remain static while other parts are flowing, which could be provoked into flowing by nonlocal effects.

Models exist for nonlocal effects. In one such model the local $\mu(I)$ model is used to find the 'local' flow, which acts as a source of 'granular fluidity' [98]. This granular fluidity diffuses over the neighbourhood of the source, activating the particles and allowing flow where the local model would predict no flow. For example, in the annular shear case, the local model predicts flow only at the wall for the quasi-static limit. This creates fluidity, which diffuses to a region near the wall, allowing for the wider shear zone seen in reality [166]. This nonlocal granular fluidity model will be discussed in more detail in Section 3.6.3.

2.4 Segregation

Granular materials come in various sizes, from large icebergs to fine powders. Some granular materials, such as rice and sand, have a relatively small size distribution, while others, such as gravel, can have particle sizes multiple orders of magnitude apart.

One phenomena that arises in a granular material with multiple particle types is segregation, where particles 'self-sort' and tend to form groups of similar particles. A typical example is the 'Brazil nut effect', where larger particles in an agitated material will accumulate at the top of the material, resulting in the material being segregated by particle size, often studied in drums [67, 77] or along slopes [179]. Particles can also be segregated by density, with heavier elements sinking to the bottom of the flow [40, 126, 156]. The process of segregating can be quite complex, creating chaotic patterns [136, 122].

Segregation appears in flowing material, such as a free surface in a rotating drum [174] or

discharge from a silo [105, 6]. This can impact industrial uses, such as pharmaceuticals and glass production, since a homogeneous material is generally desired for the production of consistent products [31, 130, 103].

Segregation can also occur in a vibrating material, such as on a horizontal vibrating plate [2]. Under the correct conditions, an agitated plate with two different sizes of particles form clusters, where the different types form crystal structures, or a 'segregation liquid' where particles are segregated, yet the structures are constantly forming and breaking apart [147].

Several segregation mechanisms have been proposed. One such mechanism that causes size segregation is that voids are temporarily created when a mixture is agitated. Smaller particles can fit into these voids more easily, meaning there is a net flow of smaller particles flowing with the body force (such as gravity), while the larger particles are displaced and move against the body force [178].

Another mechanism that causes segregation is wall induced 'convection' [107]. This occurs when wall friction causes a flow along the wall, inducing opposing currents in the rest of the domain. The boundary flow is only a few particles thick, so while smaller particles may travel along both the boundary flow and the induced convection flow, larger particles can only follow the convection flow in the non-boundary region. As such, the larger particles tend to accumulate at the edge of a boundary flow. The direction of the boundary flow, and hence the convection currents, depends heavily on the shape of the container, and can force large particles in either direction depending on the container geometry. Figure 2.2 shows a rectangular domain with downwards wall currents, which forces small particles down the domain while large particles which do not fit in the thin downwards current as easily are left to accumulate at the top of the domain.

Segregation can also occur without a body force [12, 44]. In a bidisperse material, when a large particle is surrounded by small particles, it is agitated in all directions, feeling no net force. However, when a large particle is near another large particle, these particles interact less than the small particles that would otherwise be in the place of that large particle. As a result there is a net attractive force between the larger particles, which leads to clumps of large particles surrounded by smaller particles.

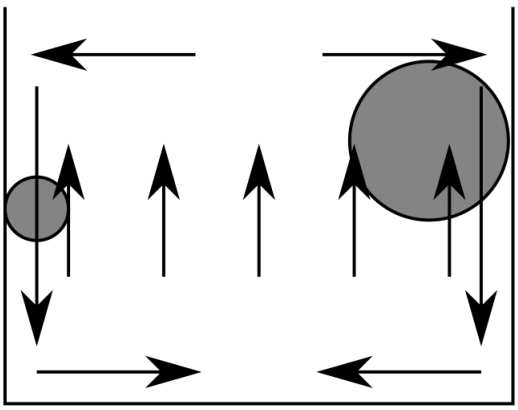

Figure 2.2: A sketch of convection currents in a rectangular domain. Thin downwards currents at the wall can capture small particles while larger particles can only 'fit' in the upwards current, leading to larger particles accumulating at the top of the domain.

One area of segregation that has not been well studied is the effect that segregation has on the dynamics of a flowing granular material. Due to the rheology being modified by the local mixture, a material with multiple components could require different physical parameters to model than each of the components of the material, whether due to different friction, sizes, densities, or other physical difference in the materials.

2.5 Dilatancy

Granular materials dilate when sheared [148]. When at rest, a granular packing will tend to form a fairly tight packing. When this tightly packed material is sheared, the particles must move other particles apart, loosening the packing slightly (Figure 2.3 gives an illustration of this mechanism). As such, while the density of the granules remain constant, the bulk density (i.e. the density of the mix of material and interstitial fluid, which for an interstitial fluid of air is generally negligible density) changes depending on the flow conditions. Bulk density can also exhibit 'density waves' in certain situations [139, 15].

A simple model for the packing fraction, ϕ, in dense flows is that it decreases linearly with inertial number I (which is discussed in Section 2.2), i.e.

$$\phi(I) = \phi_{\max} - \phi_g I, \tag{2.7}$$

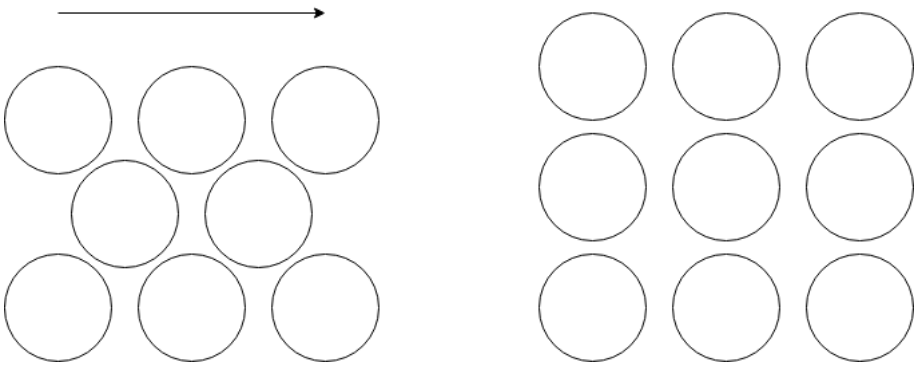

Figure 2.3: An illustration of shear-induced dilatancy. As the tightly packed particles (left) are sheared, they must move aside other particles, forming a less tight packing (right).

where ϕ_g is a constant and $\phi_{\max}$ is the packing fraction at rest in a silo [81].

Dilatancy could have a large effect on the mass flow rate in certain circumstances, however this factor is often ignored in a lot of current continuum models. In a silo, there is a significant difference in volume fraction near the orifice and away from it, with one study showing a transition from a volume fraction of approximately 0.58 away from the orifice to 0.4 at the orifice [48]. In a silo dilatancy is a significant factor for determining flow rate, and will need to be accounted for to make a comparison between a model and experiments.

2.6 Jamming

Jamming is where flowing granules cease flow, even when conditions are normally conducive to flow. The most common form of this is when an orifice in a silo is too small, allowing 'arches' to form over the orifice and blocking further flow [58], which is illustrated in Figure 2.4. This phenomenon commonly occurs when the orifice has a diameter smaller than approximately 5 particle diameters [59].

Jamming can have interesting interactions when there are multiple openings or there is an object inserted near the orifice. Spontaneous jamming and unjamming can occur, where one orifice jams, then later unjams. This behaviour is likely due to the flow near the jammed orifice perturbing the arch forming the jam, breaking the arch and allowing flow to resume [97, 109].

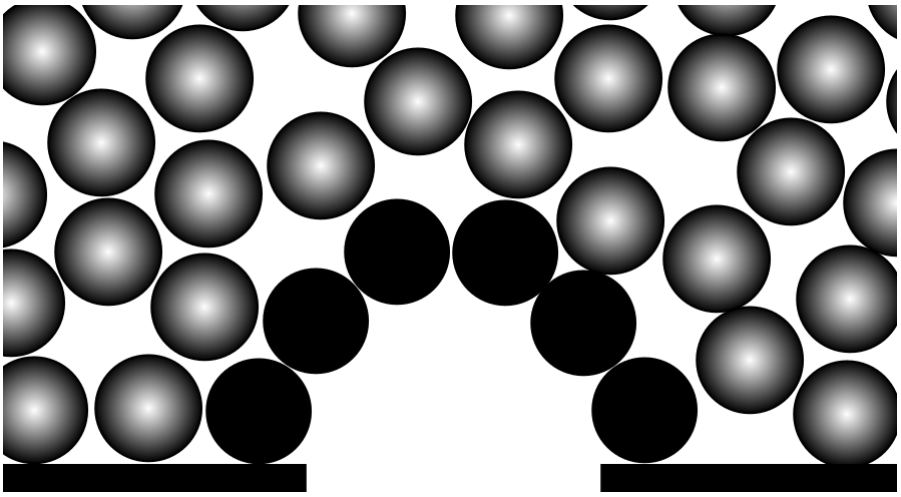

Figure 2.4: An illustration of jamming in a silo. When the opening is too small, random flow of granules can create a stable 'arch' (shown as the black circles) which is stabilised by the surrounding material and blocks all flow.

2.7 Shape effects

For mathematical and computational simplicity, studies often assume that granules are spherical. However most practical applications of granular materials involve highly irregular granules.

Differently shaped granules can have different properties, such as different effective Young's modulus, packing fraction, and rolling friction [11]. This can result in vastly different kinds of flow behaviour, some of which can be undesirable. For example, in a silo shape effects can contribute to 'bridging' (particles forming a bridge over the orifice which stops flow) and 'rat-holing' (where the center of the silo is drained and material to the sides of the silo does not flow), which are significant problems for industrial storage [30, 3].

Some researchers have applied discrete element models to 'clusters' of particles to simulate the rough particles seen in reality [167, 92], while others have used irregular or elongated polygons [138]. The roughness of particles is also going to interact with effective friction, and is also important to consider when the particles are 'wet' and cohesive capillary forces could be present [5].

2.8 Preparation effects

With a standard liquid, the history of the liquid is not required to understand the current state of the liquid. It does not matter whether it came from rainfall or seeped through the ground - as long as it is the same substance in the same location, it will behave the same. This is not true for granular materials.

Granular material can have a 'memory', where the preparation of the granular material affects the stresses in the material [171]. Hysteresis can occur because of nonlocal effects as discussed in Section 2.3, but it can also occur without current flow, when the material is completely static. The stress distribution of a static pile of sand can be completely different depending on preparation - a pile poured out of a funnel shows a bimodal stress distribution at the base, while a pile prepared by sieving shows a more uniform stress distribution with one mode [5]. The packing density also can vary depending on preparation. A sample prepared by allowing the particles to fall down like rain will be less dense than a sample which has been tapped [149]. A. Fall et. al. [45] found the packing fractions resulting from these preparation techniques to be 0.612 and 0.625 respectively.

While preparation effects are important in static materials and developing flow, they do not seem to change the steady state. When mobilised, granular material prepared with different methods can have quite different initial behaviour, however many different preparations will rapidly converge to the same behaviour [45, 51]. When considering the long-term 'steady' behaviour of a draining silo, the preparation of the material can often be safely ignored as long as the initial transient flow is omitted.

2.9 Janssen effect

In standard fluids, pressure at the base of a container of fluid depends linearly on the height of fluid, taking the form $P(h) = \rho a_g h$. In 1895 it was found by Janssen that pressure in a silo 'saturates' with increased height, with the increased load being borne by the silo walls [89, 162].

This results in the pressure at the base taking the form

$$P(h) = \lambda\rho a_g - (\lambda\rho a_g - P(0))e^{-h/\lambda}, \tag{2.8}$$

where the characteristic length λ is given by $\lambda = W_s/(4\mu_w K)$, W_s is the silo diameter, μ_w is the wall friction coefficient, and K is the proportion of horizontal stress to vertical stress and is assumed to be approximately 1. For small heights, i.e. $\lambda \gg h$, the pressure increases approximately linearly with height similar to the hydro-static case, while for large heights, i.e. $h \gg \lambda$, the pressure plateaus at $\lambda\rho g$.

One related result is that flow out of a silo is only determined by the conditions near the silo orifice, unlike traditional fluids which flow faster if more fluid is in the vessel. This results in a flow rate mainly dependant on the diameter of the orifice W, where the flow rate is proportional to $W^{5/2}$ (or $W^{3/2}$ in the 2D case) [71, 158]. A similar effect can be seen in ice melange, where numerous chunks of ice float in a river, melting glacier, or similar domain. In these situations the side walls provide 'buttressing forces' which can resist the enormous weight of upstream material even when only constrained by the side walls [24].

2.10 Cohesion

Granular materials are often simplified in models to consider only solid contact forces and gravity. However many flows exhibit other forces, in particular attractive force between contacting granules. These forces are often created by capillary forces in a 'wet' granular media, but can also be caused by electric charges on the granules (which can be created via rubbing against other materials during handling), van der Waals forces (which is relevant for very fine material), solid bridges (which can occur after long contact times), or other phenomena [5].

These cohesive forces can cause the material to keep its shape in unusual positions, such as in a sandcastle [78]. Cohesion also causes problems for industrial processes via bridging or 'rat holing' [173], and industrial materials stored in silos are often dry to avoid these problems.

The cohesion increases as more liquid is introduced to the granular material, however the amount of cohesion plateaus very quickly, with a relatively small amount of liquid providing

almost all of the cohesive strength possible from larger quantities of liquid [57].

When implemented in a continuum model, cohesion can be modelled as a constant c_o added to the yield criterion, meaning the yield criterion becomes $\tau \geq \mu\sigma + c_o$ [150]. However for the purpose of the work done in this thesis, it is assumed the materials are 'dry' materials, and as such are cohesionless.

2.11 Boundary effects

Any container for granular material will have some effect on the flow of material in the container. The sides of the container are typically stationary relative to a flowing material, causing friction upon the material. The sides of a silo or the base of a slope will rarely be made of the granular material itself, so could have different frictional behaviour than the granular material. This behaviour is associated with the boundary conditions for a continuum model.

Static boundary behaviour is relatively simple to study, and dilute flows can be modelled via the Kinetic theory of granular flow, which has boundary conditions under certain assumptions [108, 17, 91]. In contrast, dense granular flow is somewhat more challenging to model.

Many studies are done or designed with the assumption of non-slip boundary conditions [96, 134, 88, 19], which is equivalent to a layer of glued particles along the boundary which cannot move. While this is a easily controllable variable in an experiment, in many situations the non-slip condition is not physically relevant. One possible alternative is the Coulomb friction condition, which could be more physically relevant for certain domains [8, 9, 10, 69]. In general boundary conditions are a poorly understood area of granular flows, and in many situations the choice of boundary condition that is most physically relevant is not clear.

In order to reduce the impact of the choice of boundary condition, this work will focus on silos with flat bottoms where little or no flow is expected along the base. This allows the use of a non-slip boundary condition, since any flow that would occur is likely negligible. Care is also taken that the walls of the silo are away from the orifice(s), such that the choice of boundary condition at the wall is not as relevant to the flow behaviour. Nonetheless a boundary condition must be chosen, so a non-slip boundary condition is used. Further work is required to examine

whether another boundary condition is more relevant.

2.12 Summary

Granular materials behave in many complex and unintuitive ways. Each of these phenomena can have an important impact on the flow behaviour in certain domains. As such, understanding how a given domain interacts with these phenomena is necessary to develop a model for granular material.

For this work the silo is the domain examined in detail. In a flowing silo, most of the material should be in the 'dense' regime, with a possibility of the material approaching 'dilute' behaviour near the orifice. This means that the main focus of this work is dense granular models. However, silos can also have static regions so understanding the quasi-static limit behaviour of the model is necessary for considering these regions.

Several of these phenomena become irrelevant or negligible with the right assumptions. With the assumption of dry and relatively spherical granular material, we can omit cohesion forces and shape effects. A silo with a sufficiently large orifice has a negligible chance of jamming. The Janssen effect can actually be an advantage for the modelling of granular flow. The Janssen effect means that only the behaviour near the orifice contributes to the flow out of the silo, with behaviour far away not interacting with the pressure or flow near the orifice.

This work is focused on examining models of granular flow, capturing relevant quantities such as velocity, flow rate, and pressure. This requires an approach for dense granular flow that would need to account for the frictional yield behaviour, nonlocal effects, and dilatancy. A model which would be extendable to include other phenomena such as shape effects and segregation would be beneficial, however a model without these effects can still be useful for certain materials and domains. For comparisons with experiments, we make the assumption that the material is relatively spherical, homogeneous, and dry, which allows us to omit consideration for shape effects, segregation, and cohesion. We also make the assumption that the domain is chosen such that jamming does not occur, preparation effects are irrelevant to the long term behaviour of the material, and that nonslip boundary conditions are suitable.

In the next section, multiple different models are examined and compared to find a suitable model to adapt for silo flows.

Chapter 3

Models of granular flow

There are two main approaches to examining the physics of granular materials. One approach is to model each granule individually, while the other is to treat the material as a continuous field. Modelling individual particles, known as discrete element modelling (DEM) [39], provides a way of modelling granular material based on well understood physics and directly measurable particle properties. While DEM is a powerful method for obtaining overall flow behaviour from the individual particle physics, it is also very computationally expensive. While modelling thousands of particles is feasible without specialised hardware, many industrial situations require millions or more particles - a single cup of sand contains millions of particles. With powerful computers or clusters, it is possible to simulate systems with millions or billions of particles [26, 175, 56]. However, this approach is only feasible for certain domains, and the computational cost of DEM makes it less desirable for many applications. Continuum descriptions of granular flow are much much less computationally expensive compared to discrete models. Nonetheless, as the models for continuum flow are not derived directly from the physics of individual particles these approaches can fail to model phenomena such as nonlocal effects [98].

This chapter begins by covering discrete element models in Section 3.1, though they are not the focus of this thesis. Next, various continuum models are discussed, roughly in order of when they were developed. Section 3.2 covers the Mohr-Coulomb model, Section 3.3 covers the kinematic model, Section 3.4 covers the stochastic model. Finally, Section 3.5 covers the $\mu(I)$ model and its extensions, which is our model of primary focus through the remainder of this

thesis.

3.1 Discrete Element Modelling

The discrete element model (DEM) tracks the motion of particles by using Newton's second law of motion and Euler's second law of motion to calculate the translational motion and rotational motion of individual particles. The dynamics of large scale flows emerge from this model of individual particles, with many studies finding that DEM has excellent predictive ability [184, 65, 104, 128, 29], with the caveat of large computational overhead. The quality of DEM is dependant on the ability to accurately model pairs of particle collisions (which may be elastic or inelastic). As such, the specification of the contact forces is vital for achieving accurate results with DEM.

Two major collision models are the Hookean and the Hertzian models [39]. Each of these models consider collisions between spherical particles. The Hookean model simplifies particle contacts to obtain a linear model, while the Hertzian model describes the physics of elastic sphere collisions in more detail [74, 94, 160, 37].

The Hertzian model gives the force between two spherical granules as

$$\boldsymbol{F} = \sqrt{\frac{\delta R_i R_j}{R_i + R_j}}[(k_n \delta \boldsymbol{n}_{ij} - m_{\text{eff}} \gamma_n \boldsymbol{v}_n) + (k_t \Delta \boldsymbol{s}_t - m_{\text{eff}} \gamma_t \boldsymbol{v}_t)], \tag{3.1}$$

where:

- δ is the overlap between spherical granules (i.e. depth of the depression made in the granules),
- R_i and R_j are the radii of particles i and j respectively,
- k_n and k_t are the elastic constants for normal and tangential contact respectively,
- $\boldsymbol{n}_{ij}$ is the normal vector from particle i to particle j,
- $m_{\text{eff}} = \frac{m_i m_j}{m_i + m_j}$ is the effective mass, with m_i and m_j being the mass of particles i and j respectively,

- γ_n and γ_t are the damping terms for normal and tangential contact respectively,
- $\boldsymbol{v}_n$ and $\boldsymbol{v}_t$ are the relative normal and tangential velocity components respectively,
- $\Delta \boldsymbol{s}_t$ is the tangential displacement vector.

The contact model has two main components, the normal component ($k_n \delta \boldsymbol{n}_{ij} - m_{\text{eff}} \gamma_n \boldsymbol{v}_n$) and the tangential component ($k_t \Delta \boldsymbol{s}_t - m_{\text{eff}} \gamma_t \boldsymbol{v}_t$), each of which have an elastic and inelastic term.

The normal elastic term, $k_n \delta \boldsymbol{n}_{ij}$, comes from the Hertzian contact model. A full calculation can be found in [93]. Here a dimensional argument will be presented as in [5]. Consider two spherical particles compressed by a force F, and assume that the force is sufficiently small such that the compression depth δ is much less than the radius R of each particle. Here we simplify and will assume the particles have identical properties for the presentation, however the harmonic mean can be used in cases where they do not.

The particles will compress and form a 'contact disk' of radius a, with average force $F/\pi a^2$ over this area. Strain is of order δ/a since deformations decay from contact over a distance proportional to the contact size. Using the relation $\sigma = E\epsilon$, where E is the Young modulus, σ is the stress, and ϵ is the strain, we can arrive at the relation $F \approx Ea\delta$. For $\delta << R$ we can use Pythagoras' Theorem to find $a \approx \sqrt{2\delta R}$, giving the relation $F \approx E\sqrt{2R\delta^3}$. Given a constant of proportionality k_n (which Hertz theory gives as $k_n = \frac{2E}{3(1-\nu^2)}$ where ν is the Poisson ratio of the material), we obtain the equation

$$F = \sqrt{2R\delta} k_n \delta. \tag{3.2}$$

If R is replaced by the harmonic mean of two radii, the desired term is found.

While elasticity and friction are modelled in almost all simulations using discrete element models, some simulations also need to take cohesion forces into account. This is particularly important for 'wet' granular material, where some liquid is introduced to the granular media (but does not completely saturate the gaps between grains). In these wet flows capillary cohesion is a major force that needs to be accounted for, however examples of other phenomena that cause these cohesion forces are electrostatic effects, van der Waals forces, and solid bridges. Cohesion forces are highly dependent on the roughness and size of the granules [72], as well as the amount

of liquid connecting the granules, where the force transitions between different regimes as the geometry of liquid bridges changes significantly.

3.1.1 Coarse graining

Discrete element modelling gives the behaviour of individual particles, but often what is desired is an understanding of the overall behaviour. The result of a discrete element simulation gives individual particle movements, however individual particle data can be 'noisy' with single particles exhibiting behaviour that is not typical of the statistically average flow. This can be particularly problematic if the simulation is run with fewer particles to save computation time. As such, a method of converting individual particle movements into statistically average flows is needed to understand flow behaviour. This method would also allow comparison to continuum models discussed in later sections.

One method to achieve this is volume averaging, where the domain is split up into a grid and the values of particles in these grid cells is averaged over the cell [106]. Another way of analysing collective particle behaviour is by transforming DEM into continuous fields by a process called 'coarse graining'. This allows discrete data from discrete element models, empirical data from particle image velocimetry, or similarly discrete data to be used for finding an approximate continuous model [4, 177].

Coarse graining requires a radial weighting function $W(r)$ over a region V_∞ which satisfies the following conditions:

- Monotonically decreases with increasing r,
- Normalised, i.e. $\int_{V_\infty} W(r)dV = 1$,
- Infinitely differentiable and integrable over V_∞.

Then continuous fields can be extracted from a collection of discrete particles V_p in the space V_∞. For particles $i \in V_p$ with mass m_i the continuous density ρ at point $\mathbf{x}$ can be calculated by a convolution of the particle masses with the weighting function, giving the equation

$$\rho(\mathbf{x}) = \sum_{\mathbf{i} \in V_p} m_i W(|\mathbf{x} - \mathbf{x_i}|), \tag{3.3}$$

while other attributes can be calculated with an element-wise multiplication of the attribute with the weighting function. An example of this is momentum $\mathbf{p}$, which can be calculated from the velocity $\mathbf{u}_i$ of particles $i \in V_p$ and is given by

$$\mathbf{p}(\mathbf{x}) = \sum_{\mathbf{i} \in V_p} \mathbf{u}_i m_i W(|\mathbf{x} - \mathbf{x}_i|). \tag{3.4}$$

The velocity can then be found from the density and the momentum via the relation

$$\mathbf{u}(x) = \frac{\mathbf{p}(x)}{\rho(x)}. \tag{3.5}$$

Similar methods can be used for other attributes, such as granular temperature T_g and stress σ and τ [62, 176].

For practicality the restriction on smoothness is often relaxed, and a piecewise function is used with $W(r) = 0$ for r greater than some value, typically $3 \sim 5$ particle diameters. This means than calculations only need to be done for particles in a small neighbourhood around a point rather than the whole domain, which can reduce the computational complexity without significantly affecting the calculated values. An example of a piecewise weighting function is a truncated Gaussian [177], given by

$$W(r) = \begin{cases} V_w^{-1} \exp\left(\frac{-r^2}{2\lambda^2}\right) & r \leq c, \\ 0 & r > c, \end{cases} \tag{3.6}$$

where λ is the spatial averaging length scale often chosen to be $\lambda = d$, c is the cut-off point often chosen in the range $3\lambda < c < 5\lambda$, and V_λ is the normalisation constant given by

$$V_\lambda = \left[\sqrt{2\pi}\lambda \operatorname{erf}\left(\frac{c}{\sqrt{2}\lambda}\right)\right]^3, \tag{3.7}$$

which ensures the weighting function is normalised.

While DEM can provide accurate models, the computational cost is prohibitive for many scenarios. The most computationally demanding aspect of DEM is 'neighbour searching', i.e.

finding which particle pairs are in contact (and hence exerting force). A brute force approach scales with the square of the number of particles, i.e. $O(N^2)$. Efficiency gain can be achieved by assigning particles to spatial bins to reduce the search space leading to computation time that scales closer to $O(N)$, with a hierarchical grid approach required when a mix of particle sizes is modelled [168, 135].

Many simulations have been done with a few thousand particles [7, 111, 114]. Larger simulations of several hundred thousand or millions of particles are possible, but these require a large amount of computational power. Real situations typically involve many more granules, with a single cup of sand containing millions of granules. While a simulation with fewer particles can provide informative results for some industrial applications, a continuum model which reduces the computational power and time required to model problems at full scale is desirable to avoid issues when designs are scaled up.

3.2 Mohr-Coulomb analysis

The Mohr-Coulomb model describes a material which remains static relative to neighbouring material until the yield stress is reached, at which point the material mobilises along the plane where the yield stress is reached [133]. The analysis of what forces are required for yield and what axis the material will fail on can be done using a Mohr circle. This can be used to model stresses in granular material at the boundary of static and flowing material, but does not model the flow of material itself. The stress analysis needs to be combined with other assumptions to model flowing material. For a silo, two major assumptions are co-axiality, which assumes that material expands along the direction where compressive forces are smallest and contracts in the direction of highest compressive force, and radial flow, which assumes that all flow points in the direction of a single point at the convergent point of an angled silo [90].

The yield criterion, analogous to the standard static frictional rule, is given by

$$\tau \geq \mu\sigma, \tag{3.8}$$

where σ and τ are the normal and tangential stresses respectively, and μ is the friction coefficient

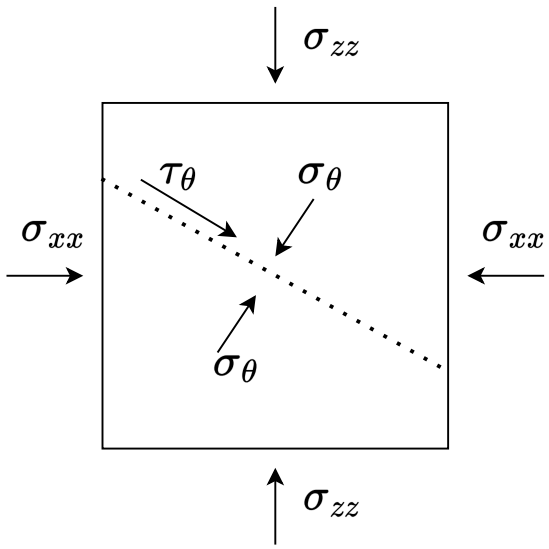

Figure 3.1: An illustration of shear stress introduced by normal stress. Even though along the xz-axis there is no shear stress, along a line at angle θ from horizontal there is an effective shear stress τ_θ.

of the material. The material will slip if and only if the yield criterion is met along any possible slip plane.

Consider a 2D element within a granular material as shown in Figure 3.1. There is a horizontal normal stress σ_{xx}, and a vertical normal stress σ_{zz} with $\sigma_{zz} > \sigma_{xx}$, with shear stresses $\tau_{xz} = \tau_{zx} = 0$. Then consider a line at an angle θ to the horizontal intersecting this point.

The horizontal (F_x) and vertical (F_z) force components for a section of area A can be found to be

$$\begin{aligned} \frac{F_x}{A} &= \sigma_{xx}\sin(\theta), \\ \frac{F_z}{A} &= \sigma_{zz}\cos(\theta). \end{aligned} \tag{3.9}$$

Projecting this force onto the line and the normal, we obtain the normal force σ_θ and tangential force τ_θ for the line,

$$\begin{aligned} \sigma_\theta &= \frac{F_x}{A}\sin(\theta) - \frac{F_z}{A}\cos(\theta), \\ \tau_\theta &= \frac{F_x}{A}\cos(\theta) - \frac{F_z}{A}\sin(\theta). \end{aligned} \tag{3.10}$$

By substituting Equations 3.9 into 3.10 we obtain

$$\begin{aligned} \sigma &= \sigma_{xx}\sin^2(\theta) - \sigma_{zz}\cos^2(\theta), \\ \tau &= \sigma_{xx}\sin(\theta)\cos(\theta) - \sigma_{zz}\cos(\theta)\sin(\theta), \end{aligned} \tag{3.11}$$

and by defining new variables

$$\begin{aligned} \sigma_0 &= \frac{1}{2}(\sigma_{xx} + \sigma_{zz}), \\ r &= \frac{1}{2}(\sigma_{zz} - \sigma_{xx}), \end{aligned} \tag{3.12}$$

we can simplify Equations 3.11 to

$$\begin{aligned} \sigma_\theta &= \sigma_0 + r\cos(2\theta), \\ \tau_\theta &= -r\sin(2\theta). \end{aligned} \tag{3.13}$$

In this form, it is intuitive to see that varying θ forms a circle in the σ, τ coordinates, with centre $(\sigma_0, 0)$ and radius r. This is called the Mohr circle.

The yield condition can be represented in σ, τ coordinates as a pair of lines through the origin with slopes $\pm\mu$, with each point between these two lines being stable. This implies that as long as every point on the Mohr circle represents a point where the yield condition $\tau \geq \mu\sigma$ is not met, the element is stable. However, when the circle intersects the yield condition lines, this represents a slip plane where failure occurs.

From the Mohr circle, the critical vertical stress σ_{zz}^c for a given σ_{xx} can be found to be

$$\sigma_{zz}^c = \Big(\frac{1+\mu}{1-\mu}\Big)\sigma_{xx}, \tag{3.14}$$

which gives the yield criterion in terms of stress; if $\sigma_{zz} \geq \sigma_{zz}^c$, the material will yield, otherwise it will not.

The above analysis is done in the 2D case and with no shear stress, but it can be easily generalized. For the case with shear stress, there exists an angle β where if $\theta = \beta$ then the shear stress at that line is zero. Then using a rotated frame of reference, i.e. using $\theta + \beta$ in the place of θ, the above analysis is valid. The normal stresses in this frame are called the principal stresses.

For the 3D case, we can rotate our frame of reference such that there is no shear stress in our frame and the normal stresses obey $\sigma_{xx} \leq \sigma_{yy} \leq \sigma_{zz}$. Then the Mohr circle can be constructed for each pair of coordinates. If each of these circles are plotted together, then the largest Mohr circle (which will be from the xz plane) will contain the smaller two circles. Any combination of forces which fall in these smaller circles will also fall within the large circle, and as such will already be yielding. In this way, the Mohr analysis can find when yield occurs in the same way as a $2D$ system without taking into account the intermediate normal stress.

It should be noted that the similar Drücker-Prager criterion, which is identical to the Mohr-Coulomb criterion for a $2D$ case, takes into account this intermediate stress [5, 41]. The criterion is that yield occurs for a given stress tensor $\boldsymbol{\sigma}$ when

$$q = \mu P, \tag{3.15}$$

where the pressure P is given by $P = \frac{1}{3}\text{tr}(\boldsymbol{\sigma})$, and the deviatoric stress q is given by $q = ||\boldsymbol{\sigma} - P\boldsymbol{I}||$.

3.2.1 Radial model

The radial model uses the Mohr circle analysis for modelling flow through a hopper [90, 133, 85]. The model assumes that every point in the hopper is at incipient yield. This is combined with the incompressibility assumption, the principle of co-axiality, as well as an assumption that flow only occurs radially (which is a reasonable approximation in the lower half of conical hoppers [127]). Using these assumptions a velocity field can be found.

Using spherical coordinates with radial distance r, polar angle θ, and azimuthal angle χ, Jenike stress is given by

$$\frac{\partial \sigma_{rr}}{\partial r} + \frac{2\sigma_{rr} - \sigma_{\theta\theta} - \sigma_{\chi\chi}}{r} + \frac{1}{r}\frac{\partial \tau_{\theta r}}{\partial \theta} + \frac{\tau_{\theta r}\cot(\theta)}{r} + \rho a_g \cos(\theta) = 0, \tag{3.16}$$

$$\frac{\partial \tau_{\theta r}}{\partial r} + \frac{1}{r}\frac{\partial \sigma_{\theta\theta}}{\partial \theta} + \frac{3\tau_{\theta r}}{r} + \frac{\sigma_{\theta\theta} - \sigma_{\chi\chi}}{r}\cot(\theta) - \rho a_g \sin(\theta) = 0, \tag{3.17}$$

where σ and τ are the diagonal and off-diagonal components of the stress tensor respectively, ρ is the bulk density, and a_g is acceleration due to gravity. Mohr circles can be used to give the

stress components

$$\sigma_{rr} = p(1 + \sin(\phi)\cos(2\psi)), \tag{3.18}$$

$$\sigma_{\theta\theta} = p(1 - \sin(\phi)\cos(2\psi)), \tag{3.19}$$

$$\sigma_{\chi\chi} = p(1 + \sin(\phi)), \tag{3.20}$$

$$\tau_{\theta r} = p\sin(\phi)\sin(2\psi), \tag{3.21}$$

$$\tau_{r\chi} = \tau_{\theta\chi} = 0, \tag{3.22}$$

where ϕ is the angle of repose of the material, p is the mean of the major and minor stresses, and ψ is the angle from the x-axis to the major principal plane on the Mohr circle.

A dimensionless stress q can be defined by the equation $p = \rho a_g r q$. It can also be noted that both ψ and q are functions of θ only, so $\frac{\partial q}{\partial r} = \frac{\partial \psi}{\partial r} = 0$. Then the stress equations simplify to

$$A\frac{dq}{d\theta} + B\frac{d\psi}{d\theta} + C = 0, \tag{3.23}$$

$$D\frac{dq}{d\theta} + E\frac{d\psi}{d\theta} + F = 0, \tag{3.24}$$

where A through F are given by

$$A = \sin(\phi)\sin(2\psi), \tag{3.25}$$

$$B = 2q\sin(\phi)\cos(2\psi), \tag{3.26}$$

$$C = \cos(\theta) + q[\sin(\phi)(4\cos(2\psi) + \sin(2\psi)\cot(\theta))], \tag{3.27}$$

$$D = 1 - \sin(\phi)\cos(2\psi), \tag{3.28}$$

$$E = 2q\sin(\phi)\sin(2\psi), \tag{3.29}$$

$$F = q\sin(\phi)(4\sin(2\psi) - [1 + \cos(2\psi)]\cot(\theta)) - \sin(\theta). \tag{3.30}$$

Then the derivatives of q and ψ are given by

$$\frac{dq}{d\theta} = \frac{CE - BF}{BD - AE}, \tag{3.31}$$

$$\frac{d\psi}{d\theta} = \frac{AF - CD}{BD - AE}. \tag{3.32}$$

L'Hôpital's rule is used in the case where $BD - AE = 0$.

There are two boundary conditions for ψ, which are $\psi = \pi/2$ when $\theta = 0$, and another determined by the friction of the wall. However, there is no boundary condition for q. To solve this problem, a shooting method can be used - the system is solved with an assumed boundary condition for q, then the extra boundary condition for ψ is checked, and the assumed boundary condition is adjusted if necessary.

With the stress field defined, the velocity can also be found. In spherical coordinates, the assumption of incompressibility is given by

$$\frac{\partial v_r}{\partial r} + 2\frac{v_r}{r} + \frac{1}{r}\frac{\partial v_\theta}{\partial \theta} + \frac{v_\theta \cot(\theta)}{r} = 0, \tag{3.33}$$

the assumption of the principle of co-axiality is given by

$$\left(\frac{\partial v_r}{\partial r} - \frac{v_r}{r} - \frac{1}{r}\frac{\partial v_\theta}{\partial \theta}\right)\tan(2\psi) = r\frac{\partial}{\partial r}\left(\frac{v_\theta}{r}\right) + \frac{1}{r}\frac{\partial v_\theta}{\partial \theta}, \tag{3.34}$$

and the relationships between stress/strain and velocity are given by

$$\dot{\varepsilon}_{rr} = -\frac{\partial v_r}{\partial r}, \tag{3.35}$$

$$\dot{\varepsilon}_{\theta\theta} = -\frac{v_r}{r} - \frac{1}{r}\frac{\partial v_\theta}{\partial \theta}, \tag{3.36}$$

$$\dot{\varepsilon}_{\chi\chi} = -\frac{v_r}{r} - \frac{v_r \cot(\theta)}{r}, \tag{3.37}$$

$$\dot{\gamma}_{r\theta} = -\dot{\gamma}_{\theta r} = r\frac{\partial}{\partial r}\left(\frac{v_\theta}{r}\right) + \frac{1}{r}\frac{\partial v_r}{\partial \theta}. \tag{3.38}$$

From these, we make one further assumption - that the velocity is only radial. From that

assumption and the equations above, the velocity can be shown to be in the form

$$v_r = -\frac{f(\theta)}{r^2}, \tag{3.39}$$

$$v_\theta = v_\chi = 0, \tag{3.40}$$

where $f(\theta)$ is some function of θ. From the Mohr circle, the relation

$$f'(\theta) = -3\tan(2\psi)f(\theta) \tag{3.41}$$

can be found, which shows the function $f(\theta)$ to be

$$f(\theta) = G\exp\left(-3\int_0^\theta \tan(2\psi)d\theta\right), \tag{3.42}$$

where G is a constant of integration which is found using the volumetric flow rate.

To eliminate the constant of integration G, the model can be scaled to match the volumetric flow rate Q. G can be found from

$$Q = -\int_0^\alpha 2\pi r\sin(\theta)v_r r d\theta = 2\pi A\int_0^\alpha F(\theta)\sin(\theta)d\theta. \tag{3.43}$$

3.3 Kinematic model for silo flow

The kinematic model is a model for silo flows based on the assumption that a difference in vertical velocity causes horizontal velocity [132] (illustrated in Figure 3.2). This, combined with incompressibility, gives a relatively simple model of granular flow. The two assumptions combined give a differential equation in the form of the heat equation [124], the derivation of which is given below.

Consider a section of granular material with a horizontal gradient of vertical velocities, as depicted in Figure 3.2. After a short period of time, a flat layer of granular material will become a 'ramp', inducing the layer of material above it to be pushed to the side. For the $2D$ kinematic

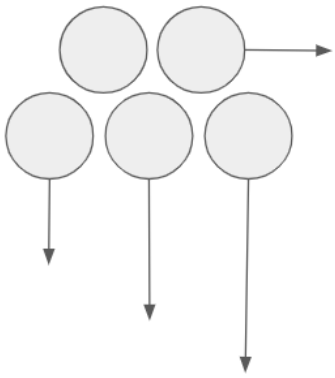

Figure 3.2: An illustration of the main premise of the kinematic model. The bottom row of particles have a vertical velocity differential, resulting in horizontal motion as the bottom particles form a ramp for the particles above.

model, this assumption takes the form

$$u = -B\frac{\partial v}{\partial x} \tag{3.44}$$

where u and v are horizontal and vertical velocities respectively, i.e.

$$\boldsymbol{u} = \begin{bmatrix} u \\ v \end{bmatrix}. \tag{3.45}$$

We also assume incompressibility, given in 2D by

$$\frac{\partial u}{\partial x} + \frac{\partial v}{\partial z} = 0. \tag{3.46}$$

These two assumptions combine to give us a differential equation in the form of the heat equation

$$\frac{\partial v}{\partial z} = B\frac{\partial^2 v}{\partial x^2}. \tag{3.47}$$

The flow can then be derived from the boundary condition set at $z = 0$. A simple choice of boundary condition is the Dirac delta function, which gives the velocity for a $2D$ silo as

$$v = \frac{-Q}{4Bz}\exp\left(\frac{-r^2}{4Bz}\right), \tag{3.48}$$

with $r = \sqrt{x^2 + z^2}$ and Q being the volumetric flow rate. The flow rate is needed to be given as a parameter, which can be predicted from the Beverloo relation which relates flow rate to the orifice size given some physical parameters [182]. A more natural boundary condition could be a 'step change' condition, i.e. $v(z = 0) = 1/2\alpha, |x| < \alpha$ with $v(z = 0) = 0$ for $|x| > \alpha$ for some length α, representing a non-zero orifice width. While this seems like a significant difference, this simply leads to a convolution of the Dirac delta solution; i.e. the velocity is the same as the Dirac delta solution, just 'spread out' in the horizontal plane.

For a $3D$ silo, the vertical velocity v is

$$v = \frac{-Q}{\sqrt{4\pi B z}} \exp\left(\frac{-x^2}{4Bz}\right), \tag{3.49}$$

where Q is the mass flow rate (which is prescribed), B is a fitting parameter, and x, z are the horizontal and vertical distance from the orifice, which is modelled as a single point.

While the model assumes the parameter B is constant, recent work has shown that is not necessarily a valid assumption [27]. Along horizontal slices, the velocity profile of the kinematic model can give a good fit with the correct choice of B. However, across different heights the value of B needed to obtain a good fit varies. While it could be possible to obtain a better model which accounts for varying B at different heights, the base kinematic model assumes that B is constant for all heights.

The kinematic model, like the radial model, fails to give a prediction for flow rate and must be scaled by the Beverloo relation. It also assumes incompressibility which does not hold over the entire silo.

Note that even if the kinematic model gives a sufficiently accurate prediction for the qualitative behaviour, a limitation of the model is that the flow rate is prescribed by Q and so provides no prediction for flow rate. As such, when examining the flow rate behaviour the kinematic model can only be used for comparing qualitative behaviour to other models which predict the flow rate (such as the $\mu(I)$ model).

We expect that in the upper middle of the silo the flow transitions to plug flow, which the kinematic model is unable to capture [132]. The kinematic model could give a closer fit for

any particular height if the B parameter is varied, however this requires a height dependent B parameter which is not justified by the assumptions of the kinematic model.

While the main assumptions of the kinematic model could be true in non-silo domains, the kinematic model was developed in order to model granular silos rather than as a generic granular flow model. As such, the kinematic model is not easily extendable into other domains. The kinematic model also does not have a time component, so is unable to model any sort of transient behaviour. While this is not a problem for obtaining the steady state behaviour, being restricted in this manner greatly reduces its applicability to domains such as a granular collapse.

3.4 Stochastic model

The stochastic model is based on the Mohr-Couloumb plasticity rules, but replaces the co-axial flow rule with an equation modelling the diffusion of 'spots' of relaxation which travel through the domain. It also requires some assumptions about the timescales of drift and diffusion, which Kamrin discusses in his thesis [102, 99]. For this analysis we will assume steady state flows.

The stochastic model assumes that flow occurs in 'spots' of local mobilisation. The material is assumed to be static outside of spots, with spots travelling through the material in a direction determined by some stochastic process. As many spots travel through the silo, the superposition of many small local flows combine to make the large-scale flow of the bulk material. By capturing the probability distribution of where spots are expected to be, the flow can be modelled. Note that spots typically travel in the opposite direction of flow - in a gravity-driven flow, a spot of local mobilisation allows a section of material to fall down slightly, which then mobilises the section of material about it which is captured by the spot moving up.

The first step involves solving a Fokker-Planck equation for the probability density of spots $\rho_s(x, z)$, which for a steady state is given by

$$\nabla \cdot (\boldsymbol{d_s}(x, z)\rho_s) = \frac{L_s}{2}\nabla^2 \rho_s, \tag{3.50}$$

where $\boldsymbol{d_s}(x, z)$ is the spot drift direction and L_s is the spot diameter (assumed to be approximately 3-5 particle diameters). Given the spot probability density $\rho_s(x, z)$, the velocity $\boldsymbol{u}(x, z)$

is given by

$$\boldsymbol{u}(x,z) = -\frac{L_s}{t_s}\int\int_{\Omega} w(x,z,x',z')\Big(\boldsymbol{d_s}(x',z')\rho_s(x',z') - \frac{L_s}{2}\nabla\rho_s(x',z')dx'dz'\Big), \tag{3.51}$$

where t_s is the timescale for a spot to drift to a new location (assumed to be equal to the timescale for a particle to diffuse to a new location), Ω indicates the entire modelled domain, and $w(x,z,x',z')$ is the 'spot influence function', which controls how a spot affects its surroundings.

When calculating the velocity field, the 'unconvolved' velocity field u^* is obtained, which is equivalent to having a spot influence function of $w(x,z,x',z') \equiv \delta(\sqrt{x^2+z^2}, \sqrt{x'^2+z'^2})$. This treats the spots as if movement only occurs inside the spot, and outside the spot no movement occurs. Using unconvolved velocity is a reasonable approximation for the final 'convolved' velocity if the shear zones are fairly large, such as in a silo, since the convolution step simply serves to smooth out the sharper features of the flow. When dealing with small shear zones, such as in a annular shear cell, the exact form of $w(x,z,x',z')$ is important to determine, however for the purpose of this report where the silo is the focus, the unconvolved velocity is sufficient and the question of the correct form of the spot influence function is disregarded.

For a 2D silo, the drift vector points directly upwards. This simplifies equation 3.50 to

$$\frac{\partial\rho_s}{\partial z} = \frac{L_s}{2}\Big(\frac{\partial^2\rho_s}{\partial x^2} + \frac{\partial^2\rho_s}{\partial z^2}\Big), \tag{3.52}$$

where we assume the silo is sufficiently wide that wall effects are irrelevant. It should be noted that if the $\frac{\partial^2\rho_s}{\partial z^2}$ term is neglected, the kinematic model is obtained.

The exact solution of Equation 3.52 is given by the Fourier integral

$$\rho_s = \frac{1}{2\pi}\int_{-\infty}^{\infty} e^{ikx}A(k)e^{\frac{z}{L_s}(1-\sqrt{1+L_s^2k^2})}dk, \tag{3.53}$$

where $A(k)$ is the Fourier transform of the boundary condition at $z = 0$. For the smallest possible opening, the boundary condition is $\rho_s(z=0) = \delta(x)$, corresponding to $A(k) = 1$. A wider opening could be considered, however a larger opening would only result in the velocity being 'smeared' horizontally as the opening widens. For $z \gg L_s$, we note that the vertical

diffusion is insignificant and the resulting vertical velocity is approximately Gaussian

$$v(x,z) \approx \frac{e^{-x^2/\sigma^2(z)}}{\sqrt{2\pi\sigma^2(z)}}, \tag{3.54}$$

with variance $\sigma^2(z) \approx L_s z + O(L_s^2)$. This matches the kinematic model with $B = L_s/2$, giving a fair approximation of idealized silo flow.

The stochastic model is a powerful model, capturing the basic behaviour of a silo while also being capable of modelling other domains. The stochastic model is also capable of capturing transient flow, which is important for certain domains. However for the silo in particular, the stochastic model requires a choice in parameters which determines the flow rate. In order to capture the flow rate information, another model is needed.

3.5 The $\mu(I)$ rheology

The $\mu(I)$ model, as described by [125] and extended to $3D$ by [96], is a powerful model capable of modelling many kinds of domains. The $\mu(I)$ model has been applied to silos [163, 186] and silo-like domains with side openings [182, 185] or multiple openings [53], shear beds [172], granular collapses [111, 164, 1], and is the baseline model that we use to describe the granular flows we are investigating. The model uses the incompressible Navier-Stokes Equations (3.55)

$$\begin{aligned} \partial_t \mathbf{u} + \mathbf{u}\cdot\nabla\mathbf{u} &= \frac{1}{\rho}\left[-\nabla P + \nabla\cdot(2\eta\mathbf{D})\right] - \mathbf{a_g}, \\ \nabla\cdot\mathbf{u} &= 0, \end{aligned} \tag{3.55}$$

where $\mathbf{u}$ is the velocity vector, $\rho = \phi\rho_{\text{granular}} + (1-\phi)\rho_{\text{air}}$ is the density derived from the packing fraction ϕ and the mix of material and gas density (ρ_{granular} and ρ_{air} respectively), $\mathbf{D}$ is the strain rate tensor given by $\mathbf{D} = [\nabla\mathbf{u} + (\nabla\mathbf{u})^T]/2$, and $\mathbf{a_g}$ is the acceleration due to gravity. The numerical methods used to solve these equations are given in Appendix B.

These equations are combined with the $\mu(I)$ rheology, which assumes that the granular

friction coefficient varies only on the inertial number I, which is given by

$$I = \frac{|\dot{\gamma}|d}{\sqrt{P/\rho}}, \tag{3.56}$$

where $\dot{\boldsymbol{\gamma}}$ is the shear rate tensor with elements $\dot{\gamma}_{ij}$ given by

$$\dot{\gamma}_{ij} = \frac{\partial u_i}{\partial x_j} + \frac{\partial u_j}{\partial x_i} = 2D_{ij}, \tag{3.57}$$

and $|\dot{\gamma}|$ is the second invariant of the shear rate tensor given by

$$|\dot{\gamma}| = \sqrt{\frac{\dot{\gamma}_{ij}\dot{\gamma}_{ij}}{2}} = \sqrt{2D_{ij}D_{ij}}, \tag{3.58}$$

d is the particle diameter, P is the pressure, and ρ is the material density.

While other formulations of the relationship of μ and I are possible [98], in this work the assumption is made that the rheology is a kind of Coulomb friction with a coefficient of the form

$$\mu(I) = \mu_s + \frac{\Delta\mu}{(I/I_0 + 1)}, \tag{3.59}$$

where μ_s, $\Delta\mu$, and I_0 are fitting parameters. Equation 3.59 defines the friction, which is implemented as an effective viscosity defined as

$$\eta = \frac{\mu(I)P}{|\dot{\gamma}|}, \tag{3.60}$$

which is used in the Navier-Stokes equations. This gives us the basic $\mu(I)$ model [125].

In order to solve the incompressible Navier-Stokes equations from the $\mu(I)$ model we use the numerical scheme described by Popinet [141], which is implemented by Lagrée & Staron [111] with the framework Basilisk [143]. The Navier-Stokes Equations can be transformed using a projection method into a Poisson equation and a Helmholtz equation. The simulation uses a volume of fluid method representing the granular material as well as the air [116]. The boundary conditions are no-slip at the walls and base, and zero pressure at the top of the silo and inside the opening. More details are given in Appendix B

Another complication posed when implementing the $\mu(I)$ model is the static zones. A static region of material means that Equation 3.60 gives an unbounded viscosity, and in a flat-bottomed silo there are some areas where there will be zero flow. To avoid divergent viscosity, a maximum viscosity $\eta_{\max}$ is enforced, i.e. the finite η^* is used, given by $\eta^* = \min(\eta, \eta_{\max})$, where η is the viscosity calculated from Equation 3.60 and $\eta_{\max}$ is a large constant. This leads to a small creeping flow in these regions which should be static in a physical silo. For our simulations we use $\eta_{\max} = 1800\sqrt{\rho^2 d^5 a_g^{-1}}$, which is sufficiently large such that the creeping flow is negligible compared to the flow from the silo draining due to gravity.

It should be noted that this model assumes that the stress and strain rate tensors are aligned. The $\mu(I)$ model relies on visco-plastic theory which assumes that these tensors are in the same direction, which is not always the case [35]. Also, the model is not well-posed, so may fail for some parameters and some domains [13, 75]. The parameters and domain studied in this thesis do not display evidence of numerical instabilities, however caution should be applied when using these models.

At the edge between the floor of the silo and the openings at the bottom of the silo, different boundary conditions are applied for the 'floor' of the silo and the openings where material exits. In order to avoid applying different boundary conditions within the length of a single discretised cell, all lengths are chosen to be some integer multiple of the cell width. Due to the tree-based discretization implementation used [170] the domain width contains 2^n cells, so the orifice widths are chosen as an integer divided by 2^n. As a result boundary cells have either 'wall' boundary conditions or 'free surface' boundary conditions, with no mix in the length of a cell.

3.6 Extensions to the $\mu(I)$ model

Each of the continuum models examined so far can give a decent approximation of the velocity in a silo, however they share some common flaws. Physical granular flows dilate as they shear, however none of these models capture the effect fluctuations in volume fraction has on the flow of the material. In addition, all of these models are 'local' models, where flow conditions at a point

do not account for the flow conditions nearby, which misses important dynamics when quasi-static material is near flowing material. Finally, in an idealised $2D$ silo the granular material is only affected by the base and the side walls of the silo, however for experimental $2D$ silos the material also experiences friction from the front and back walls of the silo. While smart choices of materials can greatly reduce this friction, nonetheless real experiments are done with some non-zero 'Hele-Shaw' like friction which these models do not take into account.

It may be possible to account for each of these factors in all of these models, however in order to reduce duplication of work, one model - the $\mu(I)$ model - is chosen to be extended.

3.6.1 Hele-Shaw friction

In implementing the $\mu(I)$ model in a $2D$ silo, we assume that the granular material is in a true two-dimensional system. In reality, the experiments are done in a system that only approximates two dimensions, with front and back walls being separated by a small non-zero distance [50]. It is possible to improve the comparison to experimental data by accounting for the friction between the granular material and the front and back walls [183].

The friction at the front and back walls provides a force $\mu_w P$, which is in the opposite direction of the $2D$ flow, $-\frac{\boldsymbol{u}}{|\boldsymbol{u}|}$. Unlike a standard Newtonian fluid where we would expect a parabolic velocity profile, for granular material with yield-stress properties we assume that the variation of flow over the thickness is negligible (i.e. the flow is only displaying $2D$-like behaviour). By integrating between the front and back of the silo, the velocity can be updated by calculating the Hele-Shaw friction which results in an extra term in the Navier-Stokes equations

$$\begin{aligned} &\partial_t \mathbf{u} + \mathbf{u}\cdot\nabla\mathbf{u} = \frac{1}{\rho}\left[-\nabla P + \nabla\cdot(2\eta\mathbf{D})\right] - \mathbf{a_g} - \frac{2\mu_w P\mathbf{u}}{W_d|\mathbf{u}|}, \\ &\nabla\cdot\mathbf{u} = 0, \end{aligned} \tag{3.61}$$

where μ_w is the friction coefficient between the granular material and the walls, W_d is the distance between the front and back wall, P is the pressure, and $\mathbf{u}$ is the velocity [182].

To implement wall friction, we calculate the Navier-Stokes equations, then apply an update to the velocity from the front and back wall friction [182]. We take the velocity already calculated,

u, and calculate an update to the velocity term

$$\Delta \mathbf{u} = -\frac{2\mu_w P \mathbf{u} \Delta t}{W_d |\mathbf{u}|}, \tag{3.62}$$

with Δt as the time step. If the update to the velocity is greater than the friction-free velocity (which could result in unphysical upward flows), the velocity is instead set to zero. This corresponds to friction being greater than the other net forces and completely arresting the flow. This updated velocity is then fed into the unmodified Navier-Stokes equations for the next time step.

Note that the parameters μ_w and W_d are both constant and are not used elsewhere. Therefore, in order to simplify the parameter set we combine them by choosing a parameter $F = \frac{2\mu_w}{W_d}$ which we vary to test the wall friction model. Then Equation 3.62 becomes

$$\Delta \mathbf{u} = -FP\Delta t \frac{\mathbf{u}}{|\mathbf{u}|}. \tag{3.63}$$

3.6.2 Dilatancy

The assumption that the granular material is incompressible is a first order approximation that simplifies the numerical methods. In reality granular material is known to dilate when sheared [5, 148]. Dilatancy introduces compressibility to the Navier-Stokes equations and increases interaction with the interstitial fluid. As such, any model which fully takes dilatancy into account would be computationally complex [14, 137, 20]. A simpler approach takes advantage of the observation that over the range of inertial numbers relevant to a silo, the packing fraction seems to linearly decrease with the inertial number I [81]. We can implement this linear dependence as a simple model for dilatancy, with

$$\phi = \max(\phi_{\max} - \phi_g I, \phi_{\min}) \tag{3.64}$$

where ϕ_g is the linear gradient parameter, $\phi_{\max}$ is a constant representing the packing fraction for a material that is not being sheared, and the minimum packing fraction is $\phi_{\min}$. Since the dominant effect of combined adjustments to both ϕ_g and $\phi_{\max}$ is only a change in effective

density, $\phi_{\max}$ is set to a fixed value, $\phi_{\max} = 0.6$, throughout this thesis. A minimum packing fraction is used in order to prevent non-physical negative packing fractions. Throughout this thesis the value of packing fraction approaches ≈ 0.4 at the orifice, so a value of $\phi_{\min} = 0.2$ is used throughout this thesis with minimal impact upon the simulations. While other formations of the relationship of ϕ to I are sometimes used [151], for simplicity we limit our scope to only consider linear dependence. This packing fraction is used to calculate the bulk density of the material. With non-homogeneous density the incompressible assumption $\nabla \cdot u = 0$ is replaced with a 'source term', which is derived from conservation of mass. This source term is given by

$$\nabla \cdot \mathbf{u} = \frac{1}{\rho}\left(\frac{\partial \rho}{\partial t} + \mathbf{u} \cdot \nabla \rho\right), \tag{3.65}$$

where ρ is the bulk density. The bulk density is dependent both on the material density as well as the packing fraction of the granular material, determined by the linear dilatancy model in Equation 3.64 (if there is no relationship between ϕ and I, the incompressible assumption is recovered).

This new 'Source term dilatancy model' takes the volume fraction $\phi(I)$ and feeds that into the bulk density, and then numerically approximates the right hand side of Equation 3.65. This approximation is then added into the projection method when the incompressible assumption would otherwise be applied.

3.6.3 Nonlocal fluidity

The $\mu(I)$ model and extensions are all local models, meaning that the properties of flow at a point are determined only by other properties at that point. However, granular material exhibits nonlocal effects, meaning that the behaviour of the material around a given point can affect the flow at that point. An example of a geometry which displays nonlocal effects clearly is flow down a slope, where there is a difference between the angle at which flow stops when the slope is lowered and the angle at which it starts when the slope is raised [145]. This difference exists because the flowing particles agitate their neighbours, maintaining flow when a local model would predict no flow is possible. Another example is an annular shear cell, where local models

predict flow sharply going to zero in the areas where the yield criterion is not met, while in experiments an exponential decay is observed [73].

In order to capture these nonlocal effects, we use a granular fluidity model [101, 153, 47]. This model finds the local 'fluidity' (which can be conceptualised as an inverse viscosity), and then 'spreads out' the fluidity into nearby regions, representing the agitation caused by flowing particles in a neighbourhood that create nonlocal effects. The fluidity g (not to be confused with gravity) is related to the μ value by the relation $|\dot{\gamma}| = \mu g$. The fluidity has some local value g_l, which corresponds to the fluidity if there were no nonlocal effects. The local g_l is then 'spread out' by the Laplacian term

$$g = g_l + \xi(\mu(I))^2 \nabla^2 g, \tag{3.66}$$

where $\xi(\mu(I))$ is given by

$$\xi(\mu(I)) = Ad\sqrt{\frac{\mu_s + \Delta\mu - \mu(I)}{\Delta\mu(\mu(I) - \mu_s)}} \tag{3.67}$$

where A is a parameter which determines the strength of nonlocal effects with $A = 0$ corresponding to a purely local model, and d is the particle diameter [101]. With the fluidity g calculated, the relations $\dot{\gamma} = \mu g$ and $\eta = \frac{\mu P}{\dot{\gamma}}$ can be combined to give the effective viscosity as

$$\eta = \frac{P}{g}, \tag{3.68}$$

which is used in Equation 3.55 in the same manner as the base $\mu(I)$ model. The choice of boundary conditions is nontrivial, however the conditions used in this work are generally zero fluidity, $g = 0$, at the walls (corresponding to infinite viscosity i.e. no-slip) and zero normal flux, $g_n = 0$, at the opening and top, although in Section 5.1 a small non-zero fluidity is used for the insert walls.

3.7 Conclusions

Each of these models have unique advantages and disadvantages. For the scope of this thesis, discrete element models will not be examined. In the first part of Chapter 4 each of the continuum models will be compared in the context of a single opening silo. As the $\mu(I)$ model

is the well developed model capable of predicting flow rate and accounting for the extensions discussed in Section 3.6, the $\mu(I)$ model and its extensions will be further examined throughout the remainder of this thesis.

Each of these models have previously been applied to granular flow in silo-like domains [133, 5, 102, 165]. In addition, the extensions to granular flow incorporated into the $\mu(I)$ model have been developed by other authors [98, 5]. This thesis adds original contribution by applying these extensions to the silo, combining these extensions, and testing the combined model in more complex domains such as the double slot silo and silos with inserts. The work done in Chapter 6, using volume-of-fluid models to model material with multiple components with different material properties, was developed by the authors and to our knowledge is original work.

Chapter 4

Application of continuum models to silos

In this chapter we discuss continuum models in pseudo-$2D$ flat bottomed silos with one and two openings, the latter of which is sketched in Figure 4.1. While flows in silos and silo-like domains have been well studied [27, 163, 53], multiple openings cause the silo to exhibit interesting phenomena that require further study [50]. In particular, the double opening silo can exhibit a 'flow rate dip', where a small separation between openings creates less flow than either a larger separation or a lack of separation (described in greater detail in Section 4.3). Studying these systems is fertile ground for obtaining further understanding of granular flows and testing the limits of continuum models.

Section 4.1 begins by examining continuum models, comparing the $\mu(I)$ model to the radial, kinematic, and stochastic models. Section 4.2 then examines the extensions of the $\mu(I)$ model in a single opening silo. Finally Section 4.3 examines the two opening silo [50]. The focus is on the $\mu(I)$ model and extensions as the other models used for single silos are unsuitable for many important metrics in the double opening domain.

Much of this chapter shares its contents with the paper "Capturing the dynamics of a two orifice silo with the $\mu(I)$ model and extensions" [86].

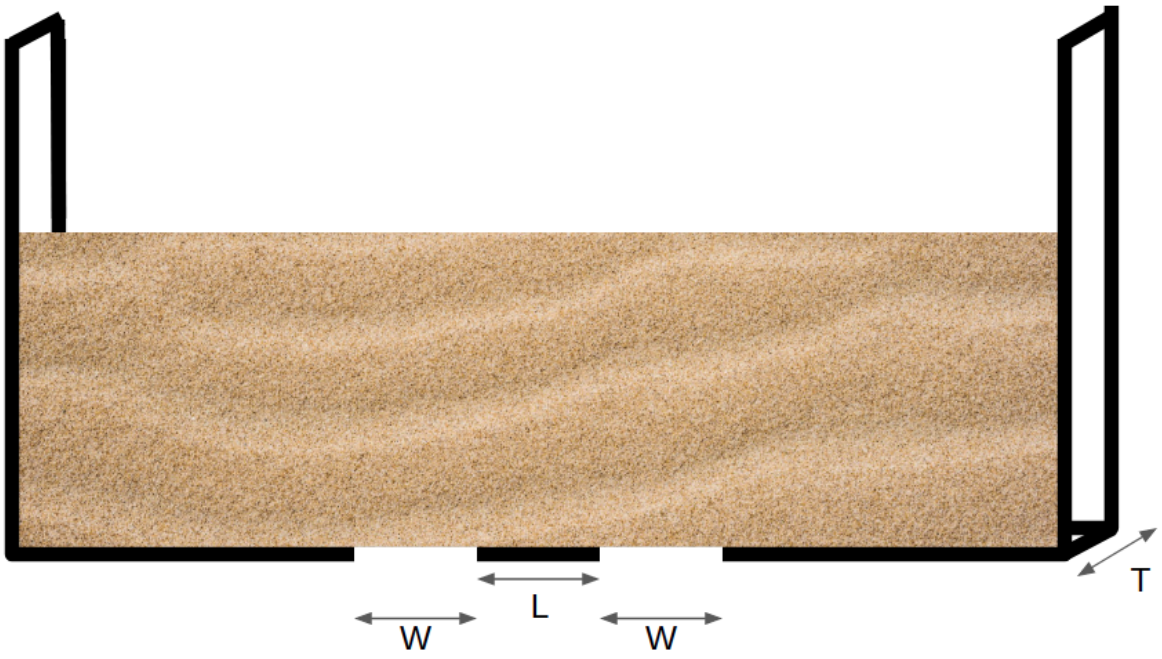

Figure 4.1: Diagram of a pseudo-2D flat bottomed silo with two openings.

4.1 Continuum models in a flat bottomed silo

4.1.1 Mohr-Coulomb radial model

The radial model, as outlined in Section 3.2, is a model based on the assumption that flow in a conical hopper is radial. This means that the flow direction is always towards the point where the conical hopper walls would meet if they were extended. This kind of flow can be empirically observed near the orifice in conical hoppers, although further from the silo the flow transitions into a plug flow regime [133, 33, 32, 159].

While this model is normally applied to a conical hopper, for a flat bottomed silo we make the assumption that material below the angle of repose is stationary, and we treat the flat bottomed silo as a silo with sides of slope equal to the angle of repose. The resulting velocity is shown in Figure 4.2, with internal angle of friction and angle of repose $\alpha = 28°$, and wall angle of friction $\alpha_w = 15°$.

The shooting method is used to find the boundary condition for fluidity q at the center of the silo given an excess boundary condition on principal stress angle ψ^* at the wall of the silo

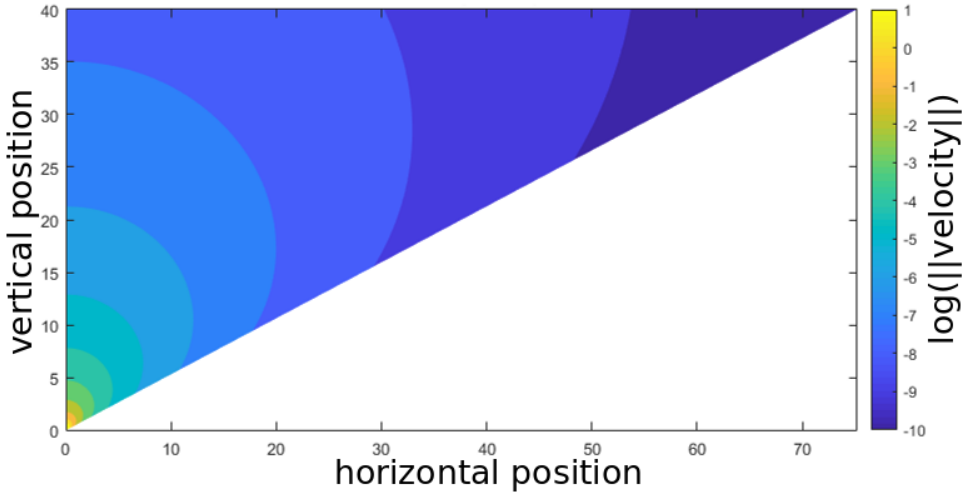

Figure 4.2: Velocity magnitude for a single opening silo with a log scale for the radial model. Material is assumed to have an angle of repose $\alpha = 28°$ which is used for the cone slope. While the velocity is calculated to the tip of the cone, practically the silo would be truncated.

(quantities defined in Section 3.2). A value of q at the center of the silo is assumed, and the resulting ψ^* at the wall is compared to the given boundary condition. The resulting error is shown in Figure 4.3. This process is repeated until a q boundary condition which minimises the error in ψ^* is found, which for this system is found to be $q \approx -0.74$.

While in practice the shooting method appears to give stable results, the shooting method may not be reliable. Figure 4.4 shows the q values over all angles in the silo θ with the boundary condition given from the shooting method. For small θ, i.e. near the center of the silo, the q value appears unstable. This instability could interfere with the validity of the shooting method.

The radial model has no obvious extension to a two opening silo. This, in addition to the other questionable assumptions and prescribed flow rate, make the radial model limited in how far it can be extended and adapted for various different domains. While the model can be suitable for certain applications, it is not suitable as a basis for a general granular continuum model.

4.1.2 Kinematic

The kinematic model, as described in Section 3.3, can be constructed from the assumption that a horizontal gradient in vertical velocity creates a horizontal velocity (though there are a variety

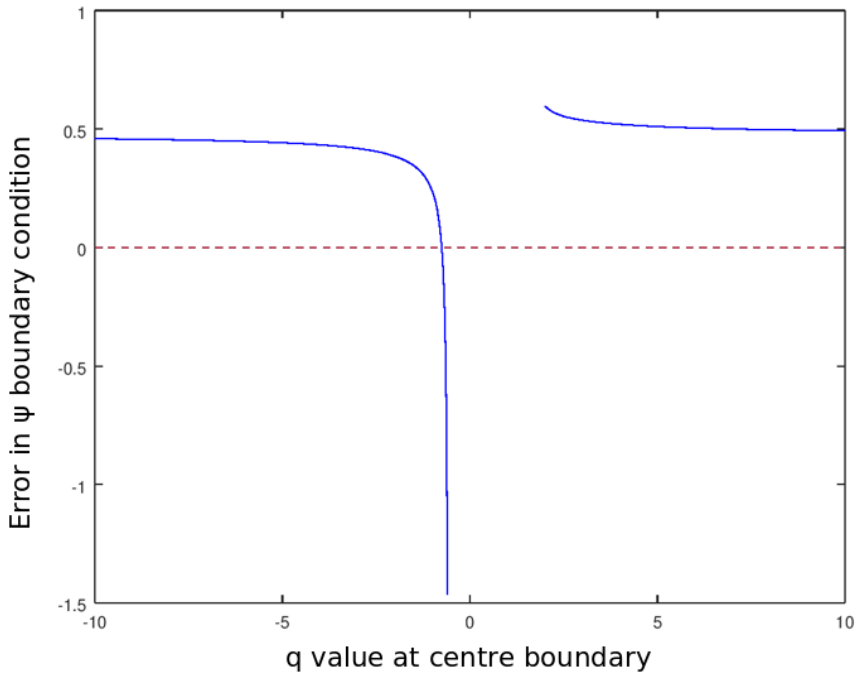

Figure 4.3: Error in ψ^* boundary condition given initial q boundary condition with shooting method.

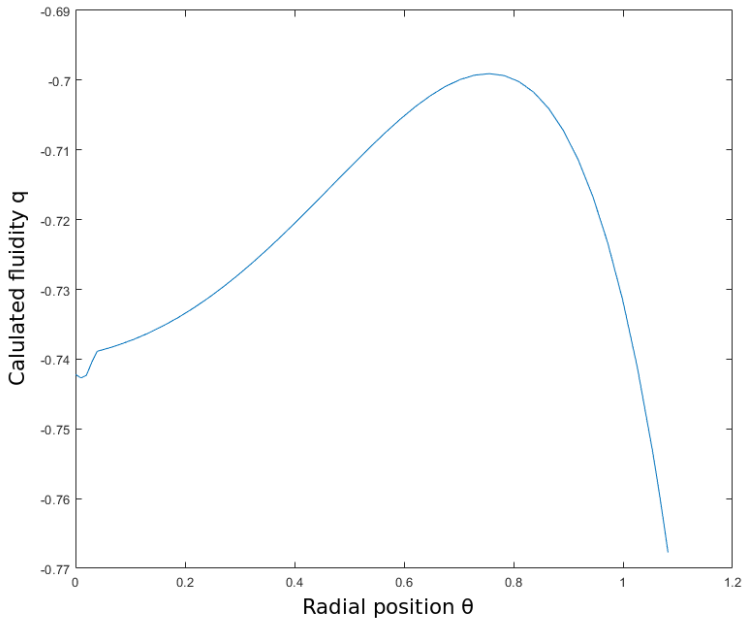

Figure 4.4: The parameter q calculated using the shooting method across the range of the spherical coordinate θ spanning from the center of the silo to the wall. Near the silo center the parameter appears to be unstable.

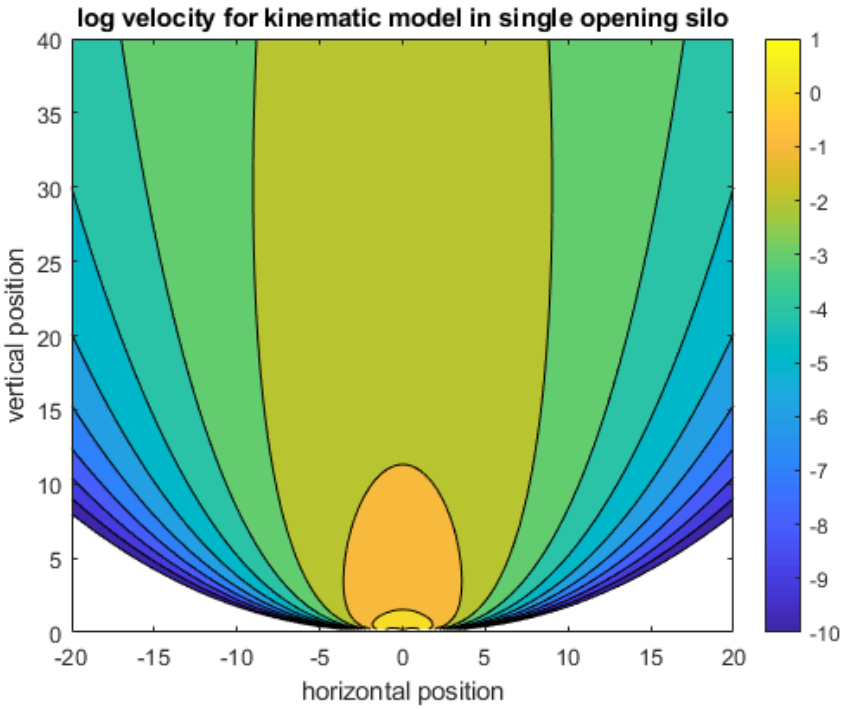

Figure 4.5: Kinematic model in a single opening silo. Velocity magnitude is displayed in a log scale.

of equivalent constructions) [132]. This assumption takes the form

$$u = -B\frac{\partial v}{\partial x}, \tag{4.1}$$

where u, v are the horizontal and vertical velocity respectively, B is a fitted parameter, and x, y are the horizontal and vertical distance from the opening respectively.

For a single opening $3D$ silo, Equation 3.48 gives vertical velocity for the kinematic model as

$$v = \frac{-Q}{4By}\exp\left(-\frac{r^2}{4By}\right), \tag{4.2}$$

with $r = \sqrt{x^2 + y^2}$ and Q being the prescribed flow rate. The horizontal velocity can be calculated from the assumption of the kinematic model. The resulting velocity magnitude for a single opening silo is shown in Figure 4.5.

The calculation assumes an infinitely small opening which gives a Dirac delta boundary

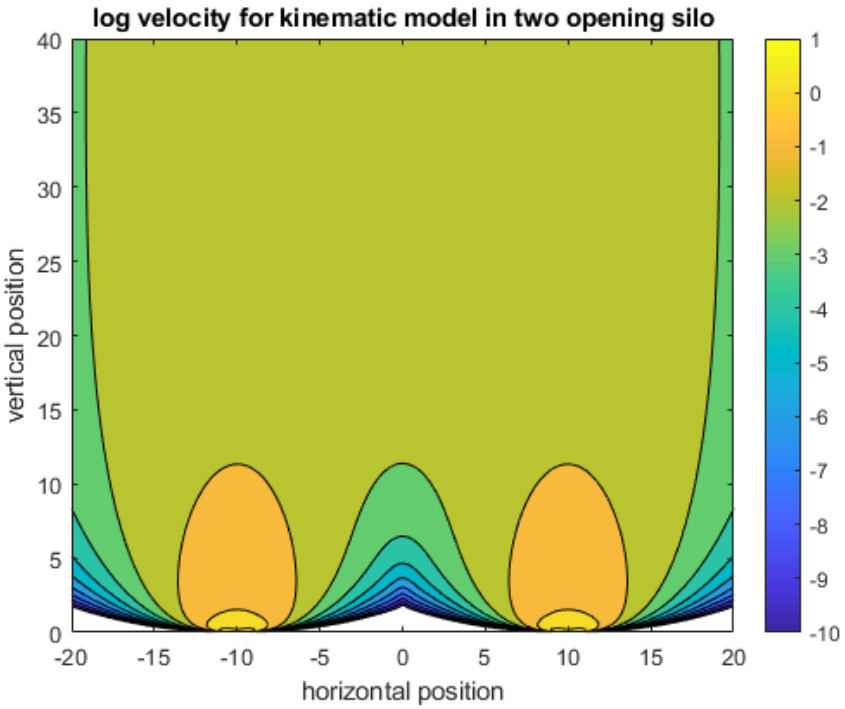

Figure 4.6: Kinematic model velocity in a two opening silo. Velocity magnitude is displayed in a log scale.

condition for the base of the silo. However, a wider opening can be considered by using a more 'spread out' boundary condition such as $H(x + W/2) - H(x - W/2)$, where W is the width of the opening and $H(x)$ is the Heaviside function. The resulting velocity is convolved with this boundary condition, resulting in the same velocity distribution but averaged out over the horizontal axis.

The same method can be used to extend the model to two openings. By using two Dirac delta functions separated by some distance as the boundary condition, we get the velocity shown in Figure 4.6. However, this fails to capture any influence of the separation of the orifices. The flow rate is determined by the integral over the base boundary condition, so is completely independent of the separation between the openings. As such, the kinematic model is unable to capture the difference in flow rate between a single large orifice and two smaller openings, and is unable to capture the variation of flow rate with orifice separation that leads to the flow rate dip.

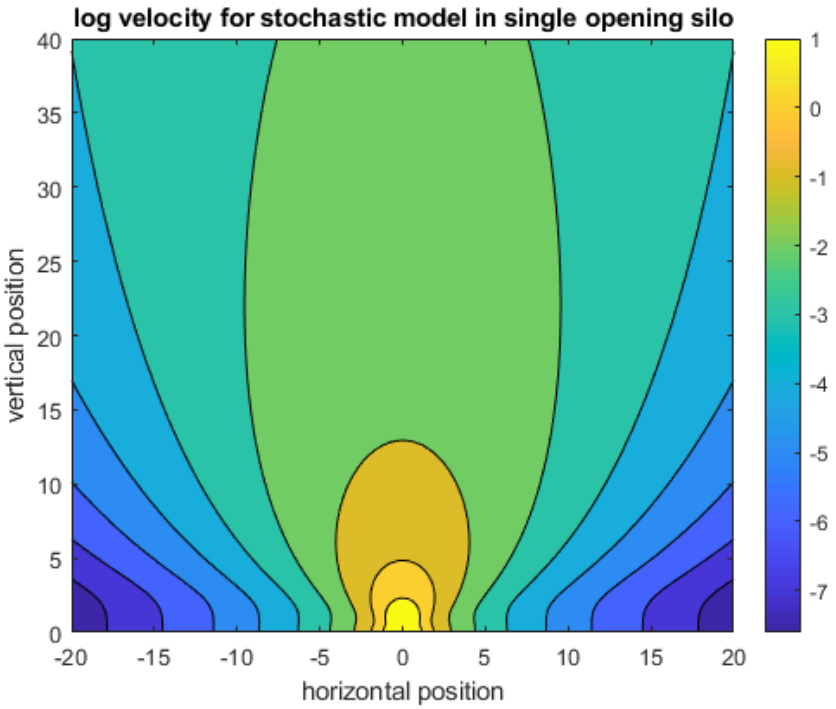

Figure 4.7: Stochastic model velocity in a single opening silo. Velocity magnitude is displayed in a log scale.

4.1.3 Stochastic

The stochastic model shares similarities with the kinematic model and Mohr-Coulomb plasticity. It assumes that flow occurs only in 'spots' which travel through the domain, and is static otherwise. The flow can then be predicted by tracking the probability of a spot travelling through the area. For a silo these spots are created at the orifice at a rate proportional to the flow rate, which then diffuse up the silo to determine the velocity field. It combines this with Mohr-Coulomb stress analysis to give a more thorough model of granular behaviour. Far away from the orifice the stochastic model approximates the kinematic results, but closer to the orifice the models diverge. The full details of the Stochastic model are given in Section 3.4. Figure 4.7 shows the calculated flow velocity for the stochastic model.

Like the kinematic model, the calculation assumes an infinitely small opening which gives a Dirac delta boundary condition for the base of the silo. The stochastic model can use different boundary conditions to spread out the flow, but the stochastic model can also have different 'spot' functions which spread out flow. Using two Dirac delta functions separated by some

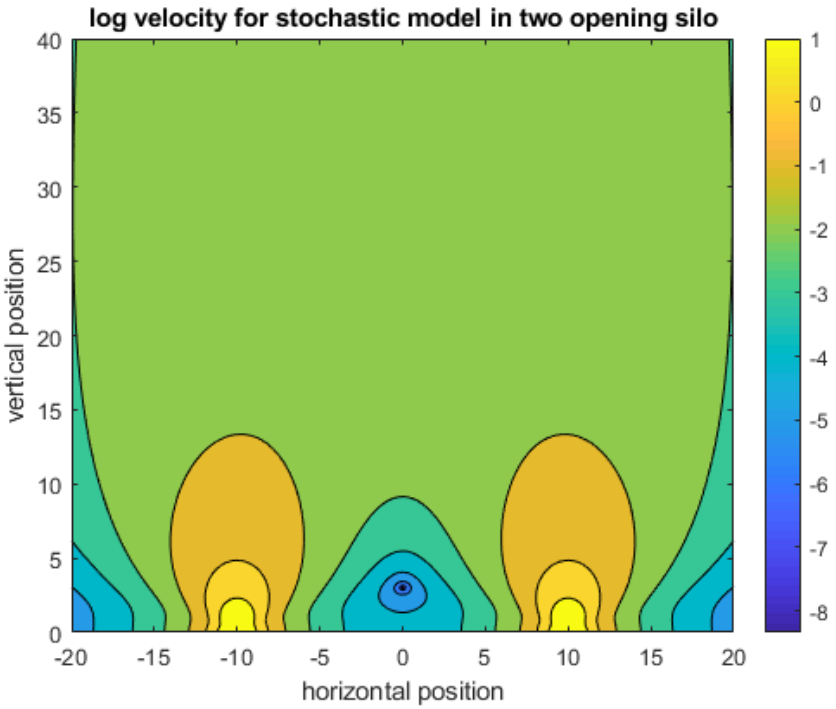

Figure 4.8: Stochastic model velocity in a two opening silo. Velocity magnitude is displayed in a log scale.

distance as the boundary condition, we get the velocity shown in Figure 4.8. Note that for a full application of the stochastic model, the spot convolution function would further smooth the velocity.

Much like the kinematic model, the stochastic model has flow rate determined by the choice of parameters L_s and t_s. The spot probability density is also determined by the boundary condition at the base in a similar way to the kinematic model, and is unable to capture the influence of multiple openings and their separation on flow rate. This makes these models poor choices when investigating phenomena related to more complicated silo domains.

4.1.4 The $\mu(I)$ model

By applying the base $\mu(I)$ model to the single orifice silo, we use the modelling software Basilisk [143] to obtain the velocity profile shown in Figure 4.9. The silo is chosen to have non-slip boundary conditions at the walls and base, and zero pressure at the opening. The simulations are done with non-dimensionalised parameters, with the choice of parameters given

Parameter	Value
Relative density of air $\rho_{\text{air}}/\rho_{\text{granular}}$	1.7×10^{-3}
Orifice width W	$9.375d$
Domain width W_{silo}	$150d$
Domain height H_{silo}	$150d$
Initial fill height H_{silo}	$135d$
Inertial number scaling I_0	0.6
Maximum solid fraction ϕ_{max}	0.6
Minimum solid fraction ϕ_{min}	0.2*
Solid fraction gradient ϕ_{grad}	0.2*
Nonlocal model strength A	0.5*

Table 4.1: Parameters used throughout this chapter, with lengths being given as multiples of the particle diameter d. An asterisk indicates the parameter is only relevant when the appropriate extension is enabled.

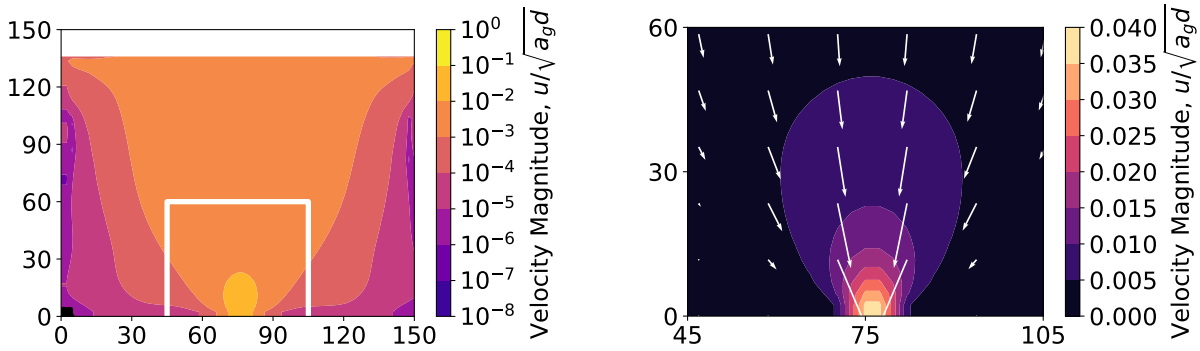

Figure 4.9: Velocity magnitude for a single opening silo, with a log scale (left) and linear scale zoomed to the opening (right). The box in the log plot indicates the area covered in the linear plot. The $\mu(I)$ parameters used are $(\mu_s, \Delta\mu, I_0) = (0.62, 0.48, 0.6)$, with an opening diameter of 0.625.

in Table 4.1. The parameters are chosen to demonstrate certain behaviours, however these parameters are similar to values other authors have found [95, 100]. The simulation is done with a fixed volume of non-replacing material.

The resulting flow matches the qualitative behaviour we expect to see in a flat-bottom silo, with static zones in the corners (with near-static creeping flow caused by the regularisation on viscosity), high flow near the orifice decreasing rapidly as points further from the orifice are considered, and 'mass flow' like behavior in the upper regions of the silo.

We also use the Nedderman Tüzün kinematic model [132] for comparison, which finds the

vertical velocity v for a $2D$ silo to be

$$v = \frac{-Q}{\sqrt{4\pi By}} \exp\left(\frac{-x^2}{4By}\right), \tag{4.3}$$

where Q is the mass flow rate (which is prescribed), B is a fitting parameter, and x, y are the horizontal and vertical distance from the orifice, which is modelled as a single point. Note that even if the kinematic model gives a sufficiently accurate prediction for the qualitative behaviour, a limitation of the model is that the flow rate is prescribed by Q and so provides no prediction for flow rate. As such, we use the kinematic model for comparing qualitative behaviour to the $\mu(I)$ model before using the $\mu(I)$ model to examine the flow rate behaviours.

A comparison between the kinematic model and the $\mu(I)$ model is shown in Figure 4.10, which shows the vertical velocity at various different horizontal slices in the silo. The $\mu(I)$ velocity is calculated throughout the silo, and least squares fitting is used to find parameters for the kinematic model for comparison. The $\mu(I)$ model predicts a 'flatter' velocity curve along a chosen height far from the silo orifice than the kinematic model. We expect that in the upper middle of the silo the flow transitions to plug flow, which the kinematic model is unable to capture. This indicates that plug flow is a phenomena that the $\mu(I)$ model can capture that the kinematic model cannot. While the kinematic model could give a closer fit for any particular height if the B parameter is varied, this requires a height dependent B parameter which is not justified by the assumptions of the kinematic model.

To further validate the $\mu(I)$ model we examine the effect of orifice width on the mass flow rate. For a silo with a single orifice we expect that the flow rate follows the Beverloo-Hagen relation, which for a $2D$ silo has the form [182]

$$Q = C\rho\sqrt{a_g}(W - kd)^{1.5}, \tag{4.4}$$

where Q is the $2D$ mass flow rate, C and k are fitting parameters, ρ is the bulk density, a_g is gravitational acceleration, W is the orifice width, and d is the particle diameter. Experiments show that k in the range $1 < k < 2$ fits the data well, although some theories suggest that k should be 1 exactly. This theoretical $k = 1$ value is due to particles occupying the width of

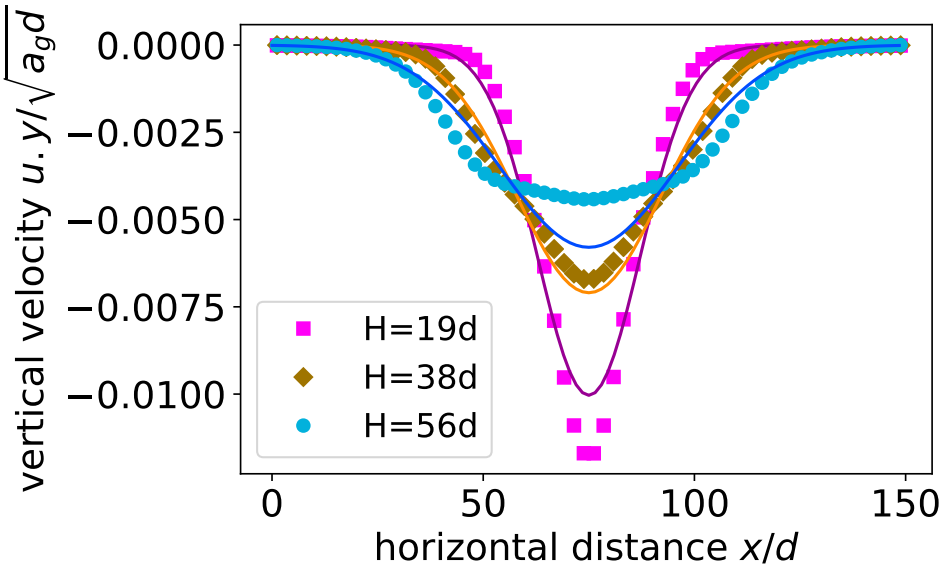

Figure 4.10: Kinematic model (lines) compared with $\mu(I)$ model (points) in a single opening $2D$ silo. The vertical velocity from simulations and kinematic model are compared for various different heights. One set of kinematic parameters is fitted over the entire silo.

a particle when passing through, meaning the effective orifice width is a particle diameter less than the actual orifice width [18, 118].

In Figure 4.11 we see a comparison of the Beverloo relation with the simulated $\mu(I)$ silo. The $\mu(I)$ simulations are done with a fixed volume of material and allowed to drain for a short time before approaching a relatively steady state. The flow rate is measured by taking the mass of granular material remaining over time and fitting a straight line (omitting the first time unit of flow to avoid transitional effects from the initial conditions). For the $k = 0$ case we see results consistent with the expected $Q \propto W^{1.5}$ relationship. The kd term is often attributed to single particle interactions, so we do not expect that it would be captured by this continuum model. Nonetheless, the $\mu(I)$ model seems to capture this kd term with $k \approx 1.92$, and the Beverloo model has a clear discrepancy with the simulations when this term is omitted. This may suggest that the kd term is not caused by individual particle interactions or the "empty annulus" theory, but is instead primarily caused by friction effects near the orifice. Note that the low orifice widths represent unphysical silos; for orifice widths less than approximately $5d$, jamming becomes a significant factor and no meaningful flow rate measurement can be achieved experimentally. The $\mu(I)$ model gives non-zero predictions for the flow rate for all silos where the orifice width

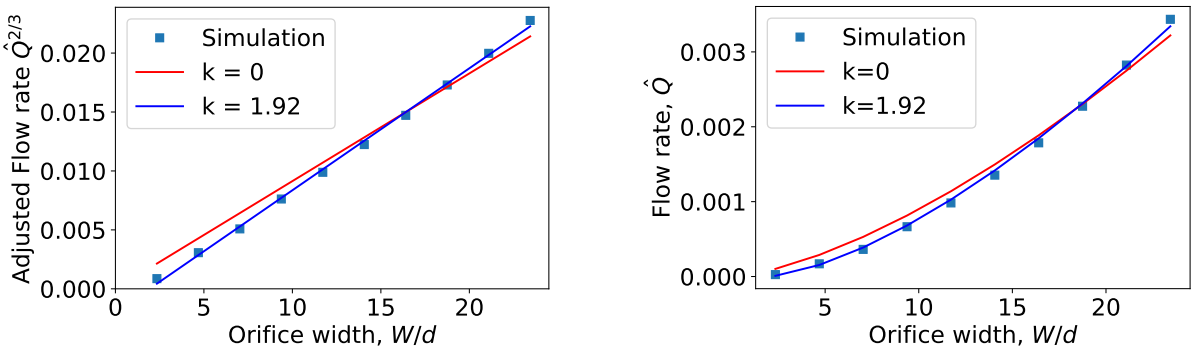

Figure 4.11: Flow rate $\tilde{Q} = Q/\sqrt{a_g d^5}$ compared to orifice width on a $\frac{2}{3}$ flow rate scale (left) and a linear scale (right), with $k = 0$ and fitted $k = 1.92$.

is greater than zero, a limitation of the $\mu(I)$ model and continuum models in general. In depth examination of these small opening sizes requires consideration of jamming, often done with a DEM or experimental method, which is outside the scope of this work [118, 97, 58, 187].

These simulations are done by discretizing the silo into a 2^n by 2^n grid of cells, with the value of n determining the resolution of the simulation. To examine the effect this grid resolution has on flow rate for a single opening silo, different choices of n shown in Figure 4.12. The flow rate seems to converge to similar values for $n = 7$ and $n = 8$, with $n = 6$ approaching this trend. Values of $n = 9$ lead to computation times that prohibitively long for this thesis. Throughout this work, the resolution value is chosen to be $n = 8$, with this comparison validating that the $\mu(I)$ model does converge in this parameter range.

We also consider the effect of varying $\mu(I)$ parameters. Figure 4.13 shows the effect on flow rate of varying each $\mu(I)$ parameter individually. The value of the base parameters used are (μ_s, $\Delta\mu$, I_0)=(0.62, 0.48, 0.6), with one of these parameters varied in each plot. These plots show that, in this range of parameters, the flow rate is relatively insensitive to changes in the friction differential $\Delta\mu$ and inertial number scaling I_0, while quite sensitive to μ_s. This insight leads us to focus on variation of μ_s, however since μ_s and $\Delta\mu$ are generally correlated with each other in physical materials these are varied together in later tests. This sensitivity analysis shows us that variation of $\Delta\mu$ in this manner is likely to have little difference on the flow rate results. The inertial number scaling is also likely low impact, although in the case where the scaling is much lower than the range chosen here there is a possibility of a larger impact.

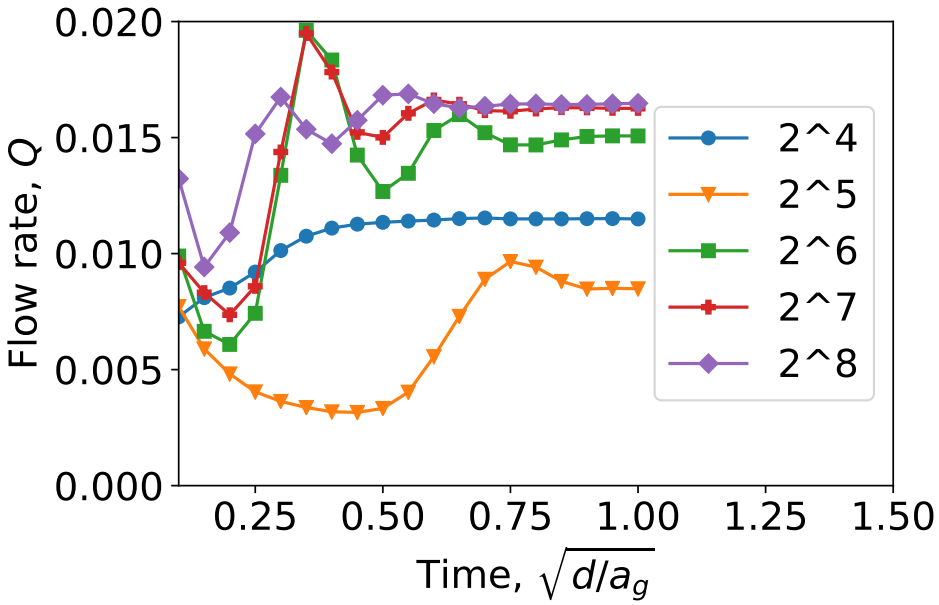

Figure 4.12: Flow rate over time for different mesh resolutions. The single opening silo is divided into a grid of 2^n cells for simulation and the resulting flow rate is calculated from the velocity flux at the opening. The finer resolutions of 2^7 and 2^8 seem to converge to approximately the same result for long time periods. A finer resolution of 2^9 becomes prohibitively computationally expensive.

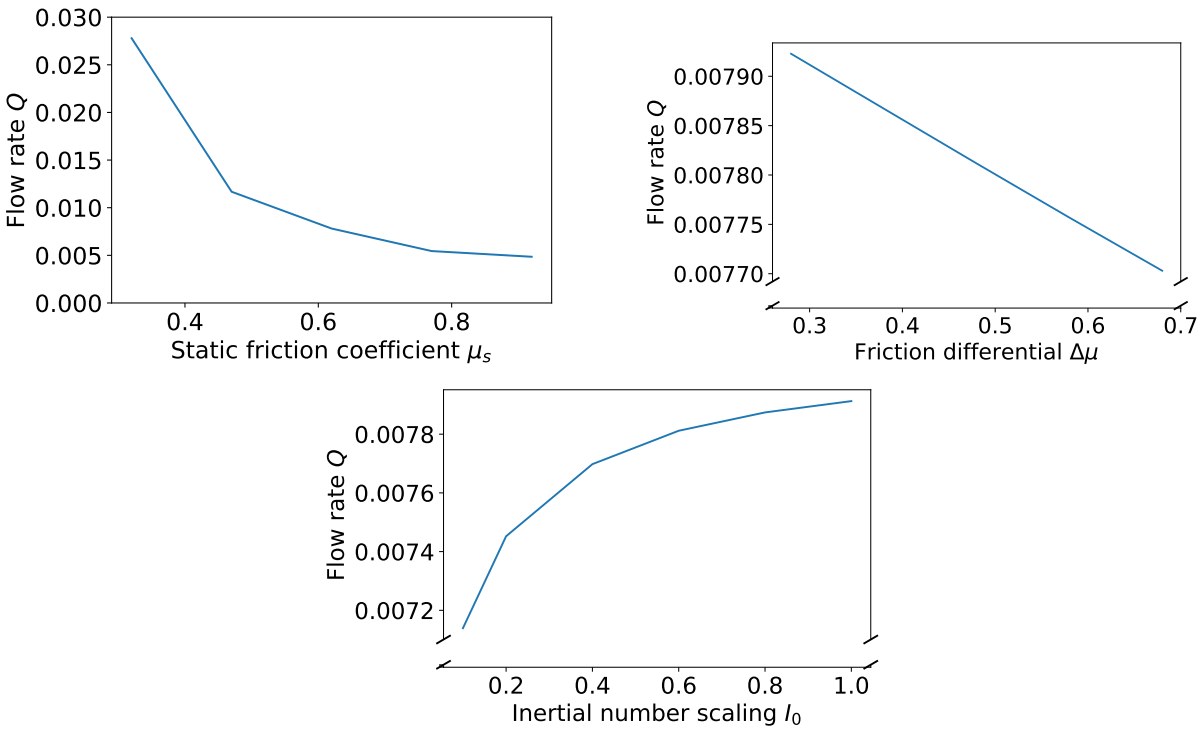

Figure 4.13: Flow rate for different $\mu(I)$ parameters. The base values used are (μ_s, $\Delta\mu$, I_0) being set to (0.62, 0.48, 0.6), with one parameter varied in each plot.

4.2 Extensions of the $\mu(I)$ model

The $\mu(I)$ model is a more general model, capable of capturing the dynamics of flow rate when multiple openings are considered. However, there are some weaknesses of the model, and so the extensions of nonlocality and dilatancy are added, as well as Hele-Shaw wall friction to account for the pseudo-$2D$ nature of the domain. Equations describing the model used for wall friction are presented in Section 3.6.1, dilatancy in Section 3.6.2, and nonlocal fluidity in Section 3.6.3. Nonlocality also requires fluidity boundary conditions, which are chosen as zero fluidity, $g = 0$, at the walls and base (corresponding to infinite viscosity i.e. no-slip) and zero normal flux, $g_n = 0$, at the opening and top.

In Figure 4.14, the Beverloo relation is examined when combinations of nonlocal effects, dilatancy, and/or wall friction are implemented. Nonlocal effects and dilatancy seem to decrease the flow rate, with nonlocal effects having the stronger effect for these parameter values. While wall friction also seems to decrease the flow rate for high orifice widths, yet for low orifice widths it seems to increase the flow rate. This could theoretically be captured by decreasing the kd term, however this require lowering the kd value well below what is observed in many experiments and theories. It should again be stressed that this analysis is done including non-physical silos with orifice widths too small to give consistent flow, and as such this analysis may have limited application to physical silos.

In Figure 4.14 we also combine nonlocal effects with combinations of dilatancy and wall friction. Adding dilatancy or wall friction when nonlocal effects are present decreases the flow rate, but to a lesser extent compared to when nonlocal effects are absent. The increased flow rate for low orifice widths also seems to be suppressed when nonlocal effects are present. Any continuum model wishing to capture the flow rate accurately will need to account for each of these effects.

4.3 Two opening silo

One interesting flow rate phenomena is the flow rate ‘dip’, which can arise when a silo has multiple orifices. Previous experiments done with spherical steel beads in a two opening silo

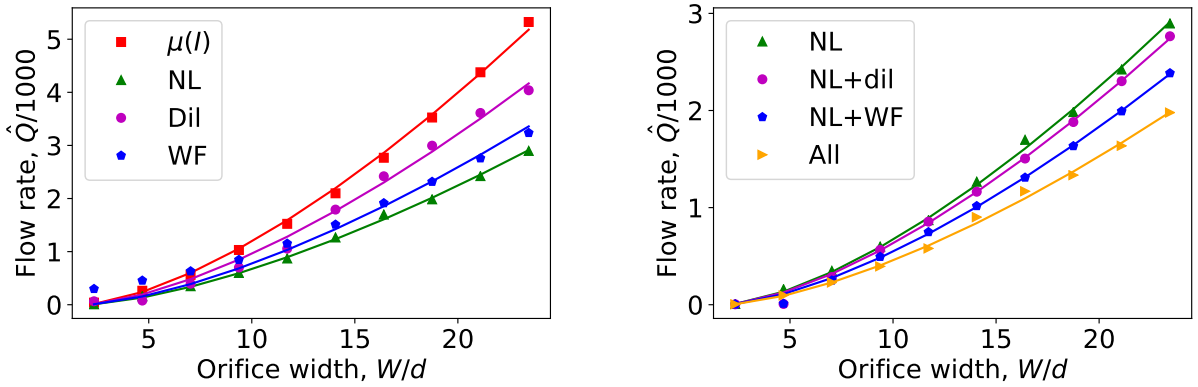

Figure 4.14: Mass flow rate $\tilde{Q} = Q/\sqrt{a_g d^5}$ for various single orifice widths with no extensions ($\mu(I)$) and combinations of nonlocal effects (NL), dilatancy (Dil), and wall friction (WF). The points show the simulation, while the lines give the fitted Beverloo relation with $k = 1.92$. For the extensions, the nonlocal strength is set to $A = 0.5$, dilatancy gradient is set to $\phi_g = 0.2$, and wall friction strength is set to $F = 0.5$.

have shown a monotonic decrease in flow rate as the orifice distance increases [180]. However, experiments done using coarser, more industrially relevant materials result in a flow rate dip, where the flow rate for a silo with two openings in close proximity to each other is lower than the flow rate for a silo with larger separations between the openings [50]. A multiple orifice silo has been modelled using the kinematic and plasticity models [123, 124], although the flow rate dip could not be analysed due to the flow rate being prescribed by the choice of parameters.

4.3.1 Friction effect on dip

When examining the two opening silo over multiple separation distances, we find the $\mu(I)$ parameters (given in Equation 3.59) have a big impact on the shape or existence of the flow rate dip. We examine 3 different sets of parameters, with (μ_s, $\Delta\mu$, I_0) being set to (0.47, 0.38, 0.6) for a low friction simulation, (0.62, 0.48, 0.6) for a medium friction simulation, and (0.77, 0.58, 0.6) for a high friction simulation. The velocity profile of two opening silos using the medium friction values for various different orifice separations is given in Figure 4.15, with low and high friction both giving similar qualitative behaviour. For low separation distances, the fast regions near the orifice merge together creating a single fast region, while for large separations the fast regions stay relatively independent, and maintain higher independent speed.

The flow rates over different separations are shown in Figure 4.16 for different friction values

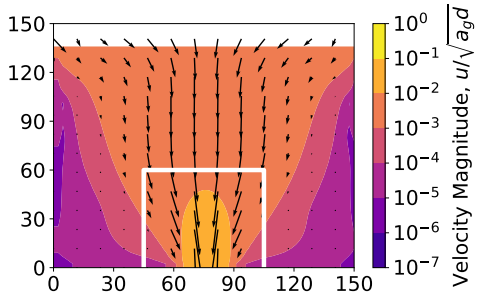

Log velocity with $L/d = 4.7$

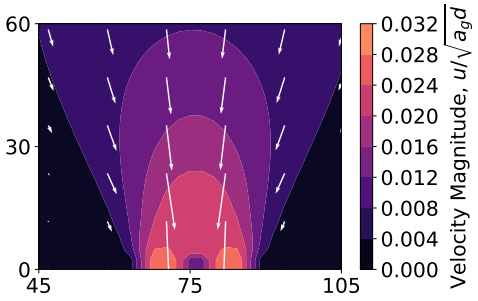

Linear velocity with $L/d = 4.7$

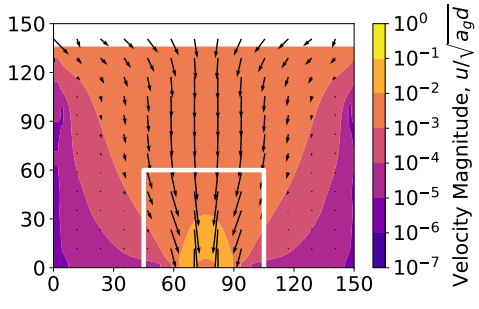

Log velocity with $L/d = 9.4$

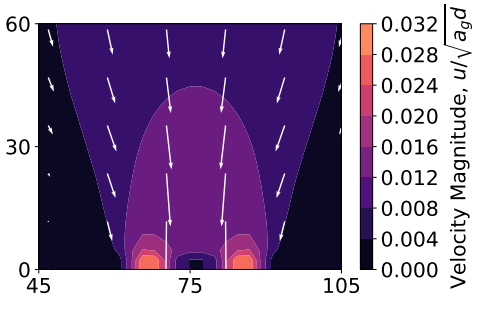

Linear velocity with $L/d = 9.4$

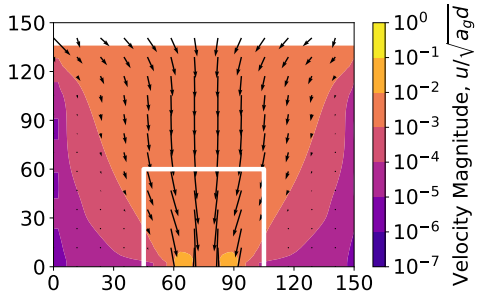

Log velocity with $L/d = 14.0$

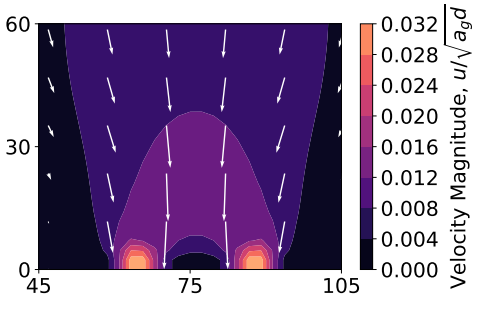

Linear velocity with $L/d = 14.0$

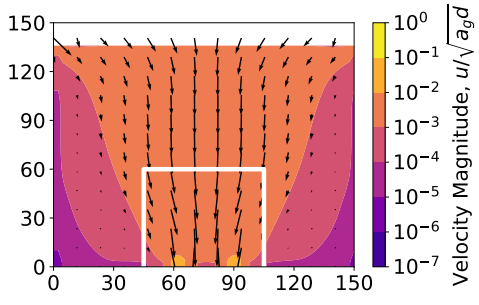

Log velocity with $L/d = 18.8$

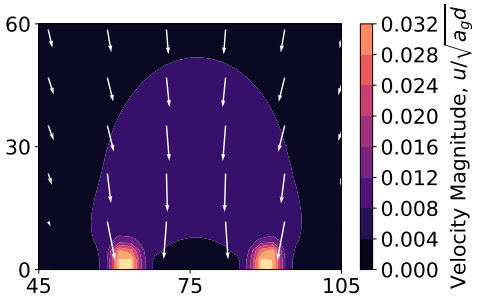

Linear velocity with $L/d = 18.8$

Figure 4.15: Velocity in two hole silos with various different orifice separations. The white box in the log plots indicate the area examined in the linear plots.

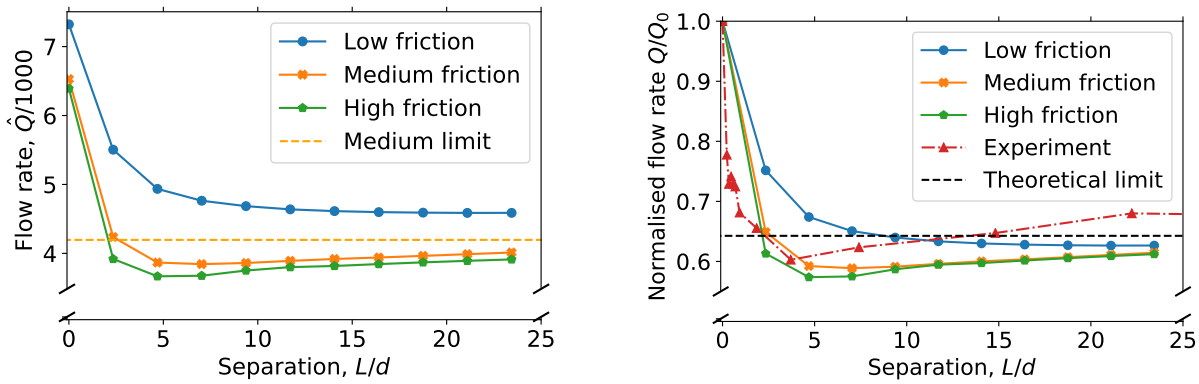

Figure 4.16: Flow rate $\tilde{Q} = Q/\sqrt{a_g d^5}$ versus opening separation length for two opening silos with different friction values. The left plot shows the raw flow rate, while the right plot shows flow rate normalised by the zero separation case. The $\mu(I)$ parameters (μ_s, $\Delta\mu$) are (0.47, 0.38) for low friction, (0.62, 0.48) for medium friction, and (0.77, 0.58) for high friction. Twice the flow rate of a single orifice silo is provided using the Beverloo relation for theoretical comparison in the normalised case (black dotted line), with only the medium friction case given for the raw flow rate (orange dotted line). The normalised data also has experimental "Amaranth small" data from [50] for comparison.

and some experimental data taken from [50]. The dotted line also shows the doubled flow rate for a single opening case with the orifice width used for the double opening cases. This should give the flow rate for arbitrarily large separations (since interactions between the orifices are negligible, the silo will act as two single orifice silos). For the low friction case, we see that the flow does not dip significantly, instead decreasing in what seems to be a monotonic pattern. The low friction case does go below the expected infinite separation value; this could be because of the side walls affecting the flow for large orifice widths. For medium friction values, the flow rate dips in a similar manner to the experiment, though the dip is more gradual than the experimental data, with the dip occurring over a greater separation range than the experiment shows. The medium friction data also does not seem to have as large of a difference between the minimum dip value and the large separation value. The high friction values seem to have similar dipping behaviour to the medium friction values. Some tests with high friction values are numerically unstable, and as such the 'medium' values are used as the default values when not otherwise specified.

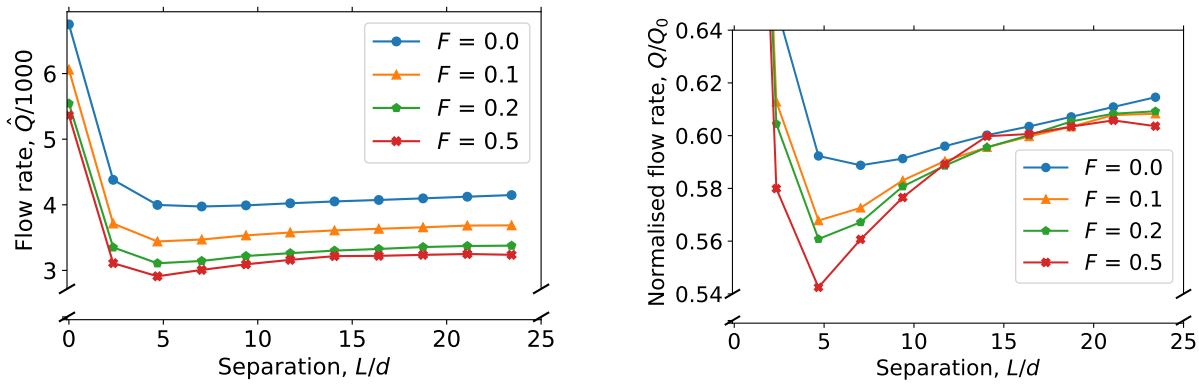

Figure 4.17: Flow rate $\tilde{Q} = Q/\sqrt{a_g d^5}$ versus opening separation length for two opening silos with different wall friction values. The raw flow rate dip is shown on the left, while on the right the flow rate normalised by the zero separation case is shown.

4.3.2 Hele-Shaw wall friction

In Figure 4.17 we show the flow rate as a function of orifice separation for medium $\mu(I)$ parameters combined with various values of the wall friction parameter F. Accounting for the Hele-Shaw wall friction given by Equation 3.63 has a significant effect. As intuitively expected, increased friction decreases the overall flow rate for all separation values. The dipping behaviour of the flow rate occurs for all of these different wall friction values, however greater wall friction results in the dip deepening. For the normalised plot the flow rate seems to recover to the same normalised point independently of the friction values, indicating that wall friction is impactful when the separation between orifices is low while not changing the relationship between the zero separation case and the infinite separation case.

4.3.3 Dilatancy

The effect of dilatancy on the relationship between mass flow rate and orifice separation distance is shown in Figure 4.18. Increasing the dilatancy decreases the mass flow rate for all separations as expected, with a realistic parameter of 0.2 [5] giving approximately 20% less flow than the incompressible case. The flow rate dip occurs for all parameters tested, with the normalised flow rate recovering with increased separation at similar rates. With increased dilatancy, the normalised flow dips deeper, indicating that dilatancy heavily depends on the orifice size. Since the flow rate dip recovery is somewhat consistent for the different parameters tested, dilatancy

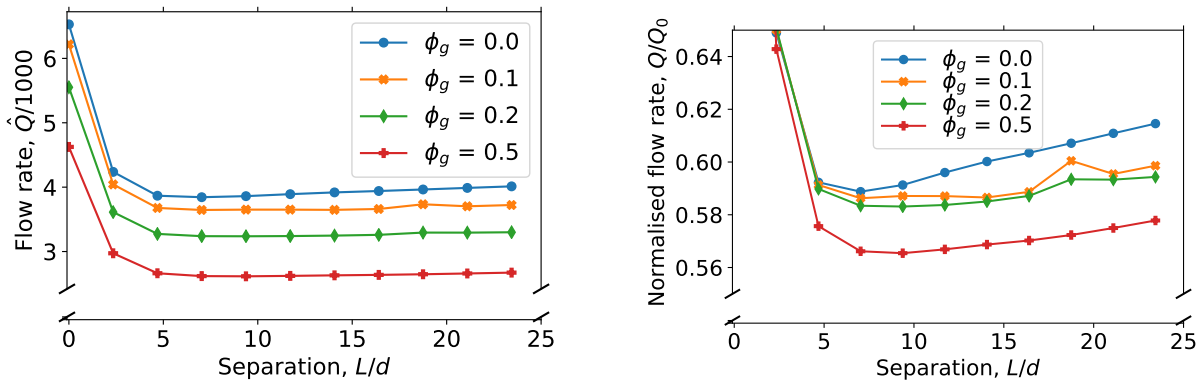

Figure 4.18: Flow rate $\tilde{Q} = Q/\sqrt{a_g d^5}$ versus opening separation length for two opening silos with different strengths of dilatancy, determined by the value ϕ_g. The raw flow rate dip is shown on the left, while on the right the flow rate normalised by the zero separation case is shown.

seems to primarily affect the flow rate dip by increasing the difference between the zero separation case and the non-zero separation cases.

4.3.4 Nonlocal fluidity

In Figure 4.19, nonlocal effects have been implemented for a two opening silo. The nonlocal effects are controlled by a single chosen parameter A. Increased nonlocal strength decreases the flow rate greatly, with a feasible nonlocal parameter $A = 0.5$ [73] resulting in approximately half of the flow rate compared to the local case. When examining the normalised plot, increased nonlocal strength seems to counteract the flow rate dip. The dip occurs for all parameters tested, however the dip is shallower when the nonlocal parameter A is greater. The normalised flow rate seems to recover to the same value, which indicates that nonlocal effects have a similar impact for the single opening with double width silo and the silo with two openings separated by a large distance. Nevertheless, the nonlocal effects do have a large impact on the flow rate dip when the distance between openings is low (but not zero). This indicates that nonlocal effects are important for capturing the flow rate dip.

Figure 4.20 shows the strength of nonlocal fluidity, g, normalised by the local fluidity, g_l, over a silo, which we use to represent the influence of nonlocal effects. This Laplacian coefficient is relatively large over most of the domain, however it drops rapidly near the orifices. This behaviour is consistent with what we expect from Equation 3.67. Near the orifices I is large,

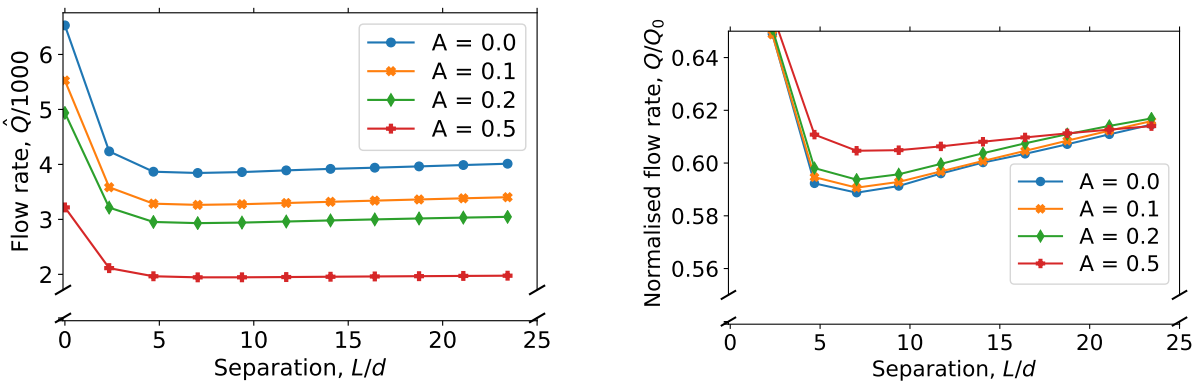

Figure 4.19: Flow rate $\tilde{Q} = Q/\sqrt{a_g d^5}$ versus opening separation length for two opening silos with different strengths of nonlocal effects, as determined by parameter A. The raw flow rate dip is shown on the left, while on the right the flow rate normalised by the zero separation case is shown.

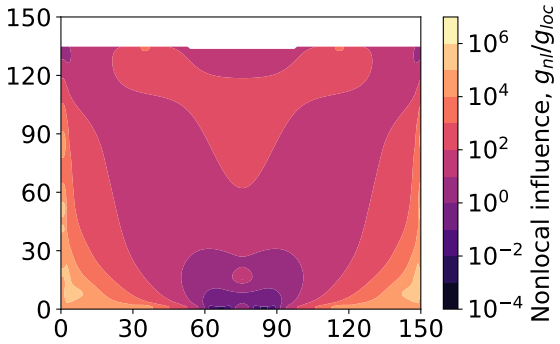

Figure 4.20: A log-scale contour plot of a two opening silo displaying the nonlocal influence g/g_l, which is used to show where nonlocal effects are strong compared to local effects.

hence $\mu(I)$ approaches $\mu_s + \Delta\mu$, meaning that $\xi(\mu(I))$ approaches zero. This suggests that nonlocal effects are dominant over most of the silo, however near the openings nonlocal effects are negligible. Interestingly, in between the orifices there is a small zone for which g/g_l is larger, indicating an increased relevance for nonlocal effects. This zone may explain why nonlocal effects decrease the impact of the flow rate dip for small separation values, since this zone may smooth out the flow for small separations.

4.4 Conclusions

A synopsis of the topics covered in this chapter is provided in the following bullet points:

- Various continuum models have been tested in a single slot silo.
- The $\mu(I)$ model is capable of partially capturing Beverloo-Hagen relationships.
- Wall friction significantly affects the Beverloo-Hagen shift.
- The base $\mu(I)$ model with high friction partially captures the flow rate dip.
- Wall friction, dilatancy, and nonlocal fluidity improve the $\mu(I)$ fit to the flow rate dip.

In this chapter various continuum models are applied to a silo, with focus on a continuum model based on the $\mu(I)$ rheology. The $\mu(I)$ model was also applied to two opening silos and extended to account for wall friction, dilatancy, and nonlocal effects.

The $\mu(I)$ model was found to give comparable but distinct velocity profiles to other continuum models, while also capturing flow rate information. The $\mu(I)$ model was found to follow the expected behaviour described by the Beverloo-Hagen relation for a single opening silo, even without modelling single particle interactions. Each of wall friction, dilatancy, and nonlocal effects were all found to have a strong impact on the mass flow rate. Wall friction effects have a significant impact on the $-kd$ shift term in the Beverloo-Hagen relation, although caution is necessary as this is partially based on theoretical data where physical silos would jam.

For a double opening silo, the base $\mu(I)$ model is capable of capturing the transition from a monotonically decreasing relationship between flow rate and orifice separation distance for low

friction materials to the more complex flow rate dip which is seen in more realistic higher friction materials via the $\mu(I)$ parameters. This shows that the flow rate dip is a frictional phenomena, with higher friction being required to obtain the flow rate dip.

Each of wall friction, dilatancy, and nonlocal effects also had unique impacts on the flow rate dip. Wall friction strengthened the dip, nonlocal effects weakened the dip, and dilatancy decreased the flow rate for the smaller orifice sizes used for non-zero separations. The extended model incorporating these three effects matches the qualitative behaviour seen in experiments better than the base $\mu(I)$ model.

Chapter 5

Granular flow around inserts

Granular material is used for many different industrial processes, and is often stored and processed using silos or silo-like domains. While drawing material from silos several problems can occur, such as jamming, rat holing, and stagnant zones [68, 187]. In order to reduce stagnant zones [169], change mixing behaviour of the material [52], reduce segregation of mixed material [34], or otherwise affect the flow of granular material in a silo [112], inserts of various shapes are often used. Being able to model the behaviour of granular material in a silo with an insert is highly relevant to many industrial processes.

There are some effects that the basic $\mu(I)$ model does not capture. One such effect is compressibility. While the assumption of incompressibility greatly simplifies the numerical calculations, it is known that granular material dilates when sheared. The incompressible $\mu(I)$ model can be extended to capture some dilatancy with a pseudo-compressibility model [5] which is described in Section 3.6.2. Another factor to consider is that the $\mu(I)$ model is a purely local model, while granular materials show evidence of nonlocal effects: where the flow of material at a point is determined by the behaviour in a neighbourhood around that point rather than just the conditions at that point. However, granular material exhibits nonlocal effects, meaning that the behaviour of the material around a given point can affect the flow at that point. An example of a geometry which displays nonlocal effects clearly is flow down a slope, where the angle at which flow stops when the slope is lowered is different from the angle at which it starts when the slope is raised [145]. This difference exists because the flowing particles agitate their neighbours,

maintaining flow when a local model would predict no flow is possible. Another example is an annular shear cell, where local models predict flow sharply going to zero in the areas where the yield criterion is not met, while in experiments an exponential decay is observed [73]. The $\mu(I)$ model can be extended with a nonlocal fluidity model [100], which spreads out the local flows to capture the nonlocal nature of these flows. This fluidity model is described in Section 3.6.3.

Much of the material of this chapter is drawn from "The $\mu(I)$ model and extensions applied to granular material in silo with inserts" [87]. A $2D$ silo is modelled with various inserts (as shown in Figure 5.1) using the base $\mu(I)$ model and the dilatancy and nonlocal extensions. The impact of insert size and insert shape is examined. We examine a silo with no insert and compare to silos with diamond inserts, square inserts, triangular inserts (upwards pointing and downwards pointing), and circular inserts. Examining the diamond insert in more detail we test various insert sizes and parameter combinations. We test all these different silos for the difference in size and shape of zones where the material is static or nearly static, as well as the effect on flow rate.

5.1 Methods

A description of the numerical methods used is given in Equation 3.59, where we describe the $\mu(I)$ rheology, how it applies to the Navier-Stokes equations, and how the dilatancy and nonlocal fluidity extensions are implemented. The base parameters used throughout this chapter are given in Table 5.1, with individual simulations deviating as noted in their description.

One difference in the simulations done in this chapter than the simulations in other chapters is the nonlocal boundary conditions. The choice of nonlocal boundary conditions is zero fluidity $g = 0$ at the silo base and walls (corresponding to infinite viscosity i.e. no-slip) and zero tangential flux $g_t = 0$ at the opening and top. However for the insert boundary conditions, practically we found that using a small fluidity (i.e. $g = 10^{-3}\sqrt{a_g d}$) boundary condition avoided numerical instabilities that caused the time step to approach zero for certain parameter combinations. This small fluidity was found to have minimal impact on the flow behaviour in cases where both converged. A possible physical analogy for this is that the insert could be creating a kind of

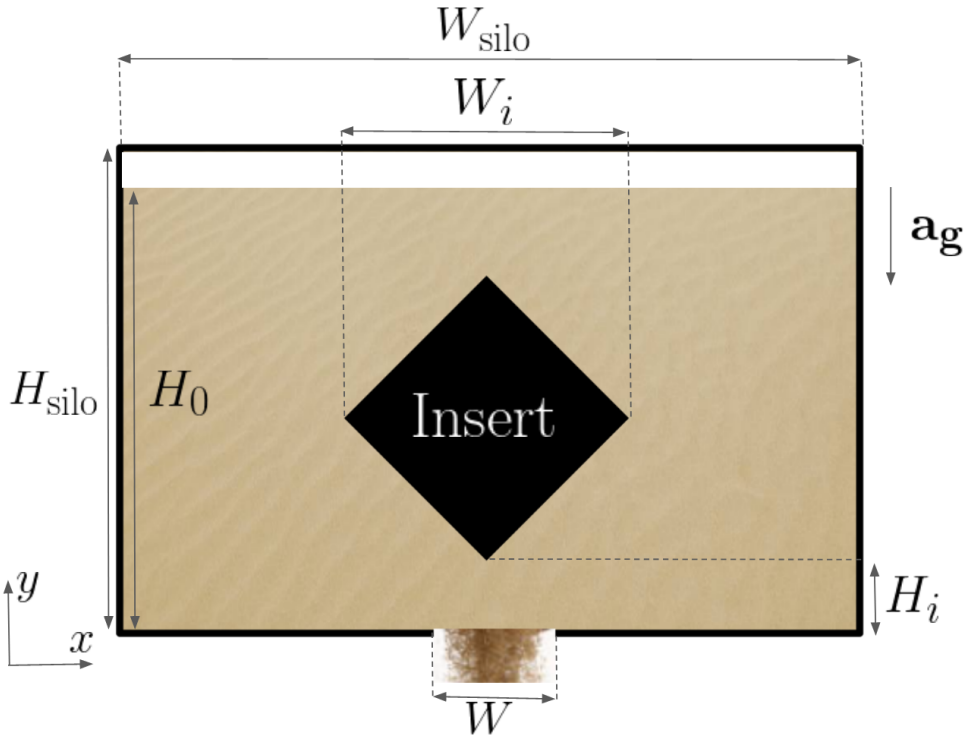

Figure 5.1: Diagram of the system being studied. Granular material flows around the insert (this case shows the diamond shape) and flows out of the outlet below. The silo is square with $H_{\text{silo}} = W_{\text{silo}} = 150d$, and is initially filled to $H_0 = 135d$. Material is not replaced during the run-time of the simulation.

Parameter	Value
Relative density of air $\rho_{\text{air}}/\rho_{\text{granular}}$	1.7×10^{-3}
Orifice width W	$9.375d$
Domain width W_{silo}	$150d$
Domain height H_{silo}	$150d$
Initial fill height H_{silo}	$135d$
Static friction μ_s	0.62
Friction differential $\Delta\mu$	0.48
Inertial number scaling I_0	0.6
Maximum solid fraction ϕ_{max}	0.6
Minimum solid fraction ϕ_{min}	0.2*
Solid fraction gradient ϕ_{grad}	0.2*
Nonlocal model strength A	0.5*

Table 5.1: Parameters used throughout this chapter, with lengths being given as multiples of the particle diameter d. An asterisk indicates the parameter is only relevant when the appropriate extension is enabled.

fluidisation similar to fluidised beds [63]. However, due to the small value of fluidity used and the low sensitivity we found to this value, fluidisation does not seem to be occurring. Boundary conditions for granular flow, particularly nonlocal fluidity, is an area which requires additional research and we forgo further study of them in this work.

5.2 Results

5.2.1 Insert shape

The geometry of the insert has a large influence on the flow behaviour. We first apply the base $\mu(I)$ model to a variety of differently shaped inserts, looking at square, diamond, triangular (upwards pointing and downwards pointing), and circular inserts, as well as comparing the silo with no insert. Flow is started and allowed to develop until a 'steady' flow is reached, at which point the velocity and other behaviour is examined ($t = \sqrt{d/a_g}$ was sufficient in all cases) [86]. Each insert is sized such that the lowest and highest point is $37.5d$ and $75d$ respectively. This fixes the height of the inserts, but not the area (compared to the square insert, the area is reduced by a factor of $4/\pi$ for circle inserts and by 2 for a diamond insert) or width of insert (which is doubled for both triangular inserts when compared to the square insert). Figure 5.2 shows velocity contours around various different shapes of insert. The case with no insert exhibits

'funnel flow' behaviour, with a fast moving region in the center and large slow moving zones to the sides. The circle, diamond, and triangle inserts all disrupt the funnel area, spreading the flow out into otherwise near-static regions. Of these shapes, the circle appears to have a large effect on spreading the flow to the sides, while the diamond appears to have the smallest.

It should be noted that the flat bottoms of the square and the triangle inserts may not display realistic results directly underneath the insert. In a physical silo with a flat-bottomed insert, we would expect a void zone with little to no material. However, the volume of fluid method used to distinguish air and granular material in this work assumes the materials are mutually impervious which is not true in practice. The unrealistic rapid horizontal flow directly beneath the insert is likely an artifact of the continuum model not being designed to model these void zones. It is possible that a true two-fluid model may be capable of modelling this behaviour, however we leave this for future work [61]. These shapes could have improperly modelled voidage, though these inserts still seem to give reasonable flows. However we limit the analysis done on the square and upward triangle shapes, and future work involving these shapes should be done using a model capable of capturing these void regions.

Granular pressure is also important to consider, with contours for each shape shown in Figure 5.3. Each of these cases has higher granular pressure in the corners of the silo representing the 'hydrodynamic' pressure, with lower pressure in the middle above the orifice. The inserts all seem to widen the low pressure zone. The inserts also have a peak of pressure above the insert itself and a decreased pressure zone directly below the insert.

Differently shaped inserts exhibit different flow rates. Finding an insert which reduces the quasi-static area while also maintaining a high flow rate may be desirable for industrial applications. The flow rate is calculated by tracking the total mass of material in the silo over time and taking a linear fit. The flow rates for different insert shapes are shown in Figure 5.4. The case with no insert has the highest flow rate, with all inserts decreasing the flow rate somewhat. Interestingly, the pressure does not seem to have a significant effect on the flow rate. Examples of relatively high flow rates and low flow rates can be found for insert shapes with high pressure in the corners (e.g. diamond and downward triangle) and low pressure in the corners (e.g. square and circle).

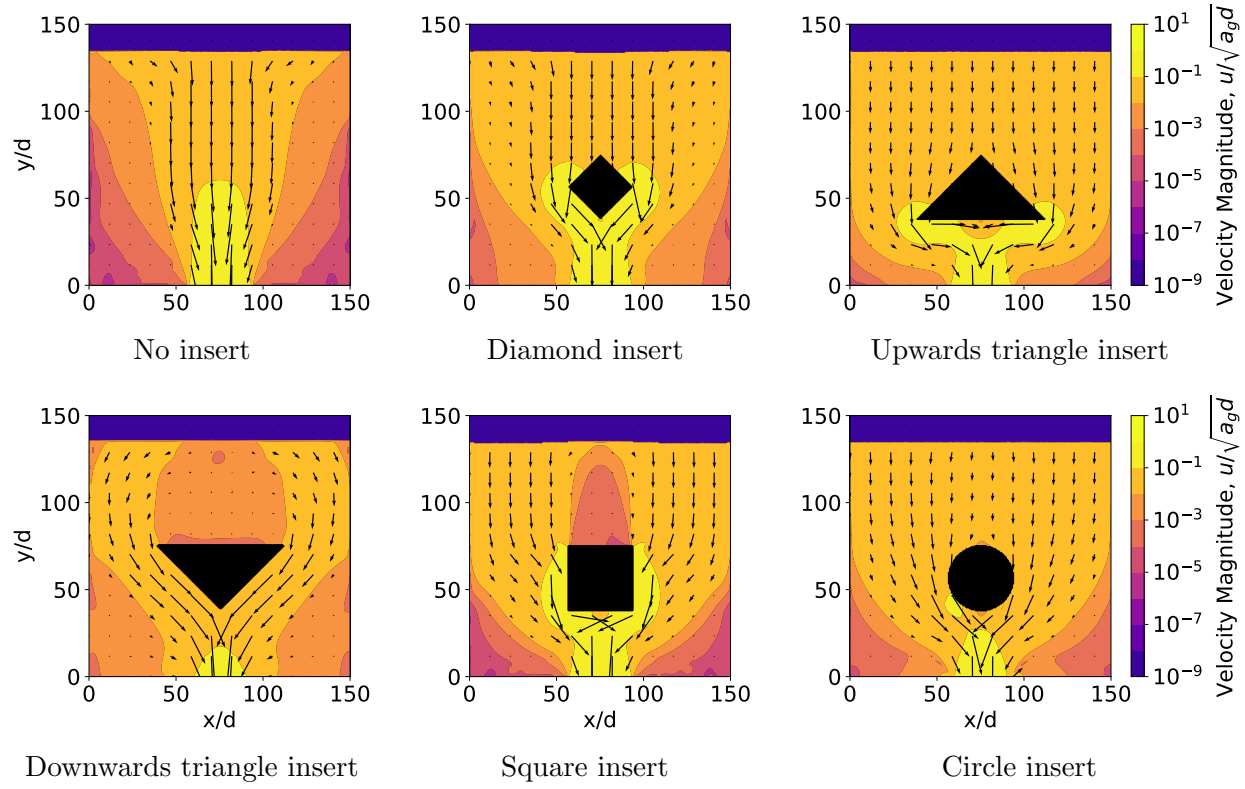

Figure 5.2: Velocity in silos for various different insert shapes. The square, diamond, and circle inserts are sized to have height and width equal to the width of the silo opening, with the triangle inserts having the same height and twice the width.

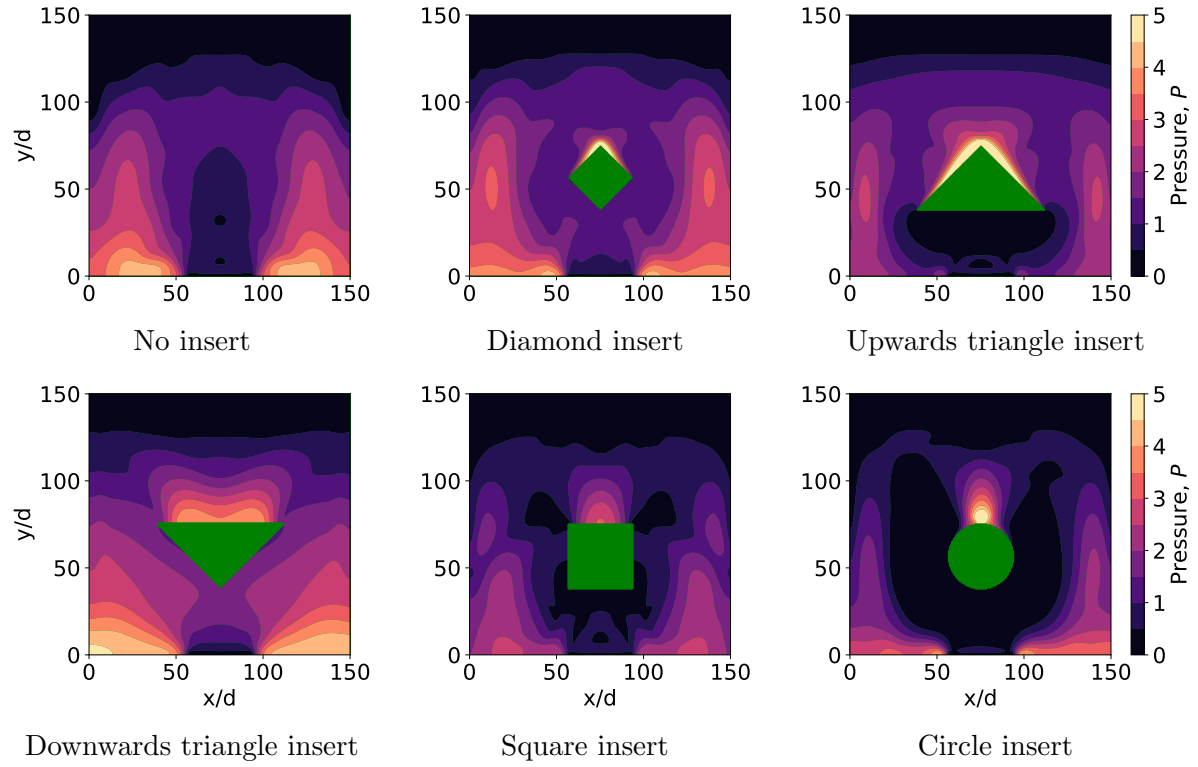

Figure 5.3: Granular pressure in silos with various different insert shapes. Pressure is nondimensionalised by $P = P_*/(\rho a_g d^{-2})$ where P_* is the dimensional granular pressure, ρ is the density of granular material with solid fraction 1, a_{g*} is gravitational acceleration, and d is the granule diameter. The square, diamond, and circle inserts are sized to have height and width equal to the width of the silo opening, with the triangle inserts having the same height and twice the width.

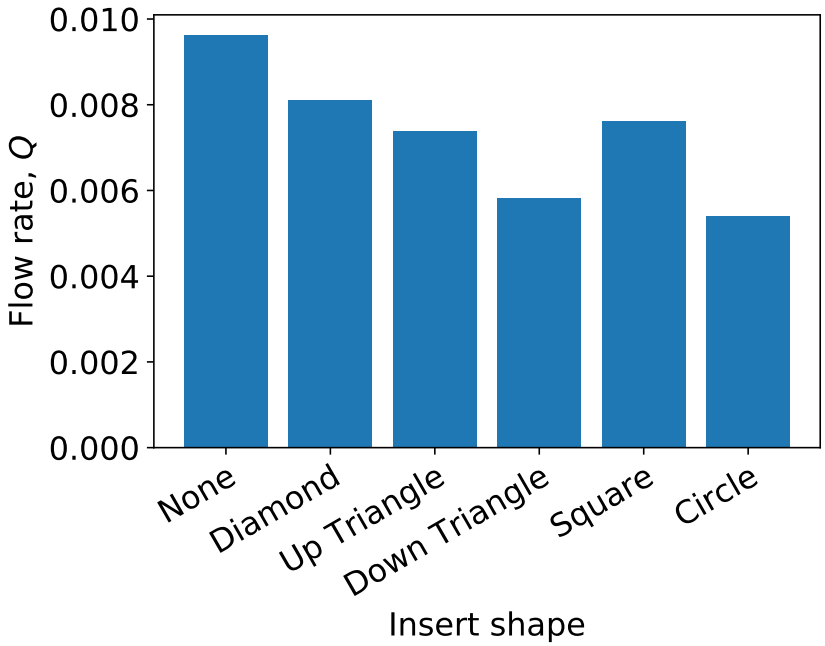

Figure 5.4: Flow rate $Q = \hat{Q}/\sqrt{a_g d^5}$ for different shapes of inserts. The square, diamond, and circle inserts are sized to have height and width equal to the width of the silo opening, with the triangle inserts having the same height and twice the width.

Extensions

We can modify the $\mu(I)$ model to capture dilatancy and to capture nonlocal effects either independently or combined. These extensions change the velocity pattern within the silo. Figure 5.5 and Figure 5.6 shows the velocity contour with base $\mu(I)$, dilatancy, and nonlocal effects. Dilatancy decreases the overall velocity throughout the silo, with peak velocity near the silo outlet less than the peak velocity given in the case without dilatancy. However, dilatancy does not greatly change the direction or shape of the flow pattern. In contrast, nonlocal effects seem to increase the velocity slightly and also change the shape of the velocity contour. The nonlocal case has slow moving regions that cover most of the areas near the bottom and side walls, reducing the size of the quasi-static zones. This may be from the Laplacian in the fluidity model 'spreading out' the zero velocity resulting from the no-slip boundary conditions. These low flow areas are displayed in some experiments [50], so nonlocal effects may be important for capturing flow behaviour near the wall.

Figure 5.7 shows the flow rate in the silo, comparing the base $\mu(I)$ model, the model with

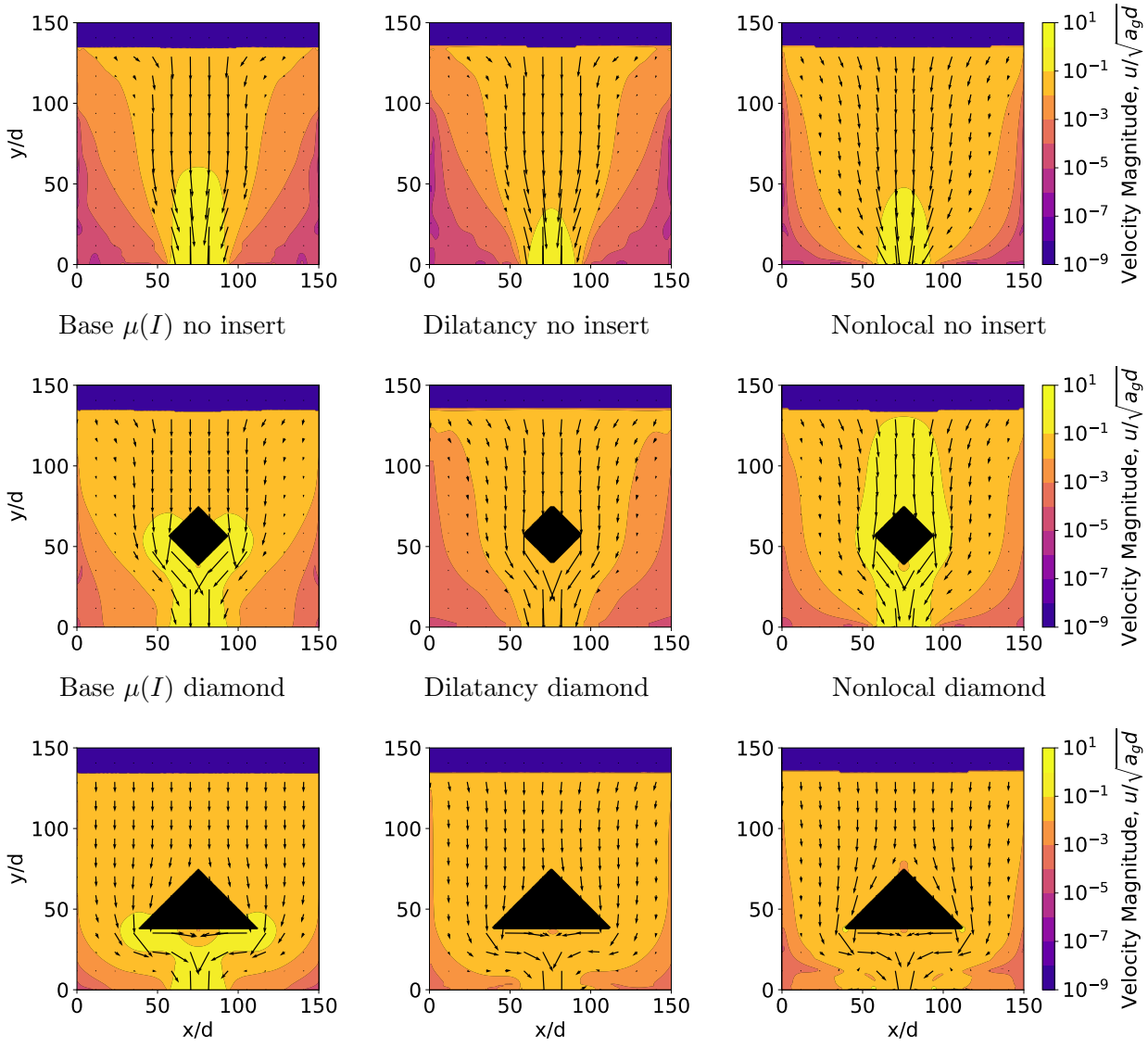

Figure 5.5: Velocity for base $\mu(I)$, dilatancy, and nonlocal models in silos with various different insert shapes. Dilatancy extension has dilatancy strength $\phi_{\text{grad}} = 0.2$ and nonlocal extension has nonlocal strength $A = 0.5$. Base case is drawn from Figure 5.2. The square, diamond, and circle inserts are sized to have height and width equal to the width of the silo opening, with the triangle inserts having the same height and twice the width. Continued in Figure 5.6

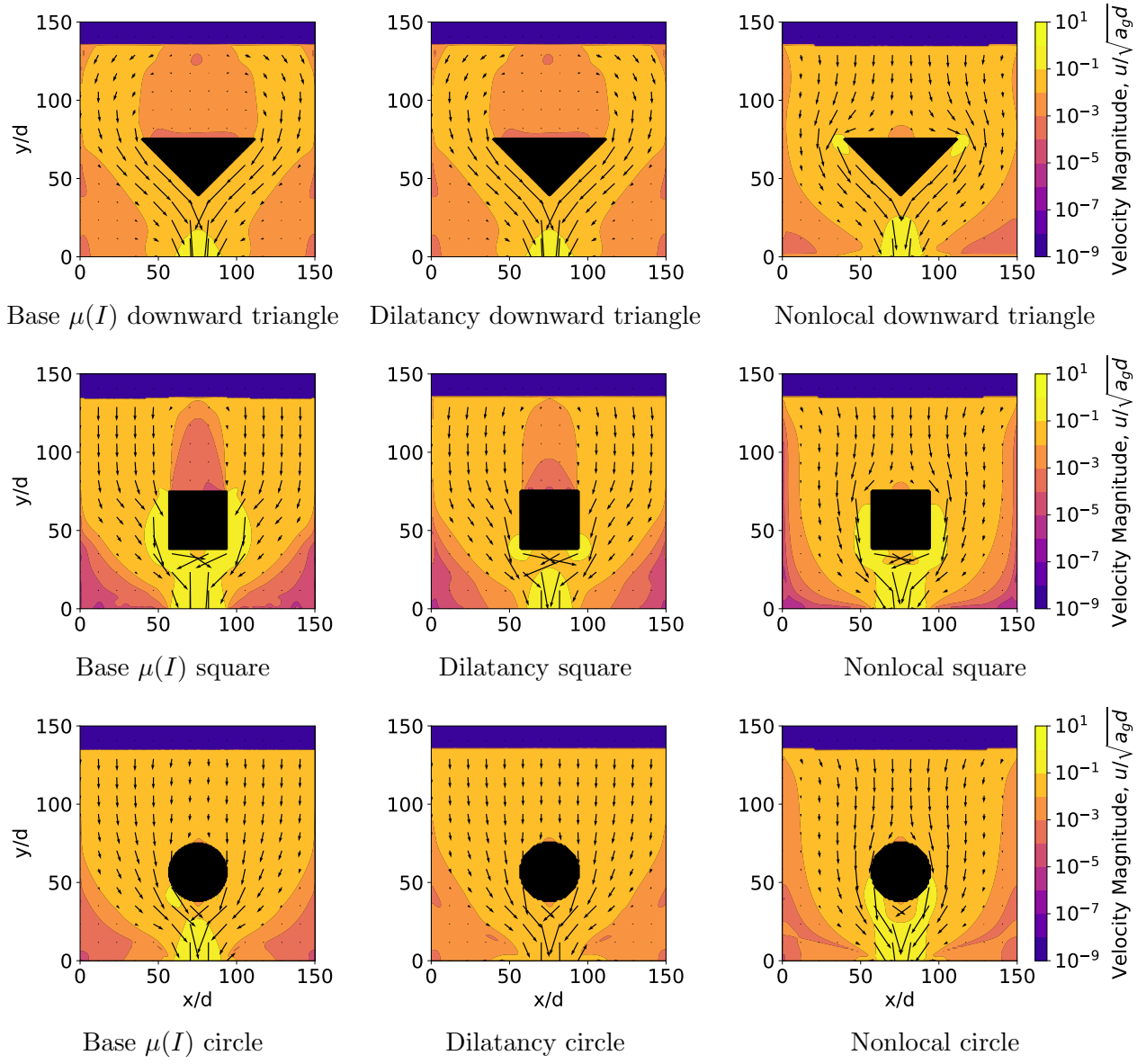

Figure 5.6: Velocity for base $\mu(I)$, dilatancy, and nonlocal models in silos with various different insert shapes. Dilatancy extension has dilatancy strength $\phi_{\text{grad}} = 0.2$ and nonlocal extension has nonlocal strength $A = 0.5$. Base case is drawn from Figure 5.2. The square, diamond, and circle inserts are sized to have height and width equal to the width of the silo opening, with the triangle inserts having the same height and twice the width. Started in Figure 5.5

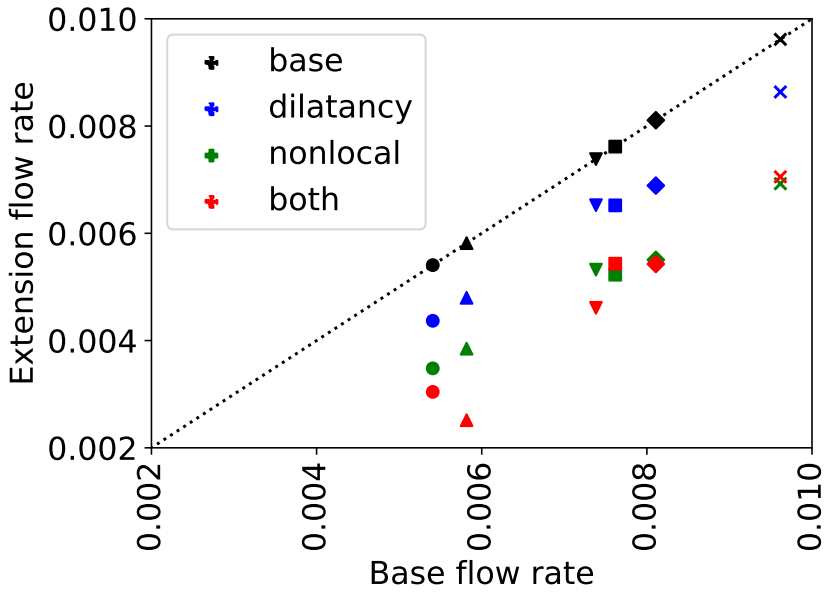

Figure 5.7: Flow rate $Q = \hat{Q}/\sqrt{a_g d^5}$ for different extensions, with dilatancy strength $\phi_{\text{grad}} = 0.2$ and nonlocal strength $A = 0.5$. The shape of the marker indicates the shape of the insert, with the 'x' indicating no insert. The dotted line is the '$x = y$' line, and the 'base' results falling on this line by definition. The square, diamond, and circle inserts are sized to have height and width equal to the width of the silo opening, with the triangle inserts having the same height and twice the width.

dilatancy, the model with nonlocal fluidity, and the model with both dilatancy and nonlocal fluidity added. These are also compared for each of the insert shapes studied (indicated by the shape of the data points, with the 'x' shape indicating no insert). Dilatancy seems to decrease the flow rate slightly when compared to the base $\mu(I)$ model, while nonlocal effects decrease the flow rate compared to the base $\mu(I)$ model to a greater extent, with a combination of both decreasing the flow rate more than both. These factors seem to be fairly consistent across the different shapes, indicating that these effects do not interact with insert shape in a manner that greatly affects the flow rate. The exception to this seems to be the inserts with flat bottoms, which have results slightly inconsistent with the linear pattern in the 'both' case, indicating there could be some interaction between nonlocal effects and dilatancy where there would be a void zone.

We can also see the influence of nonlocal granular fluidity for a selection of inserts in Figure 5.5 and Figure 5.6, which shows the relative strength of nonlocal effects within the silo.

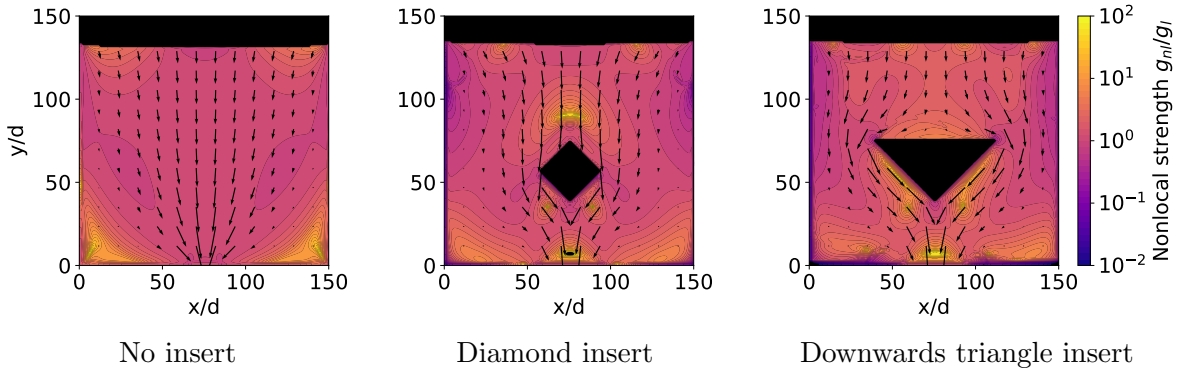

No insert Diamond insert Downwards triangle insert

Figure 5.8: Relative strength of nonlocal effects, as indicated by the ratio of nonlocal fluidity to local fluidity g_{nl}/g_l with nonlocal strength $A = 0.5$. Strong nonlocal effects can be seen near the boundaries of the lower insert and the base of the silo.

Nonlocal effects are predictably strong in the corners or above a flat insert where the material is quasi-static. There is also strong nonlocal behaviour bands just below the slopes of the inserts. This demonstrates that nonlocality has strong influence on flow past the inserts, widening the effective channel that material can flow through (as seen in the flow past the diamond in Figure 5.5) and therefore resulting in higher flow rates. The insert cases also have strong nonlocal effects near the orifice, whereas the no insert case has negligible nonlocal influence at the orifice. All of these domains have shear gradients between the rapidly flowing material and the quasi-static material in the corners, however the addition of inserts appear to greatly strengthen these shear gradients at the orifice. While Figure 5.7 indicates that the interaction between inserts and nonlocal effects has very little influence on the outputted flow rate, the interaction seems to have strong influence on the flow behaviour within the silo with an insert.

Quasi-static zones

For a physical flat bottomed silo we would expect static zones in the sides, yet the $\mu(I)$ model is incapable of truly static flow. True static regions would have divergent effective viscosity in the static zone, and would have divergent nonlocal cooperativity length if nonlocal fluidity was implemented. For numerical stability the effective viscosity is capped and zones which should be static will exhibit "creeping" flow. Even if this limitation of maximum effective viscosity was removed, physical silos display jamming behaviour, intermittent flows, and other frictional

behaviour that this continuous model would not be able to capture. Despite this limitation, we still expect the zones which are static in physical silos will also be very low speed in this continuous model. Even if these zones are not truly static, very low speed areas would also result in problems in industrial contexts as this may result in some stored material taking a long time to pass through the silo and potentially deteriorating the quality of the product. As such, we propose that quasi-static zones with very low speeds make a suitable analogy for static zones in the continuum model.

The size of the quasi-static regions are dependant on the threshold velocity. The quasi-static regions for different threshold velocities is shown in Figure 5.9. This figure shows that the threshold value of $10^{-3}\sqrt{a_g d}$ gives the balance between capturing static material and not capturing flowing material that is expected in the no insert case. For the following results we analyse the area of near-static zones with a threshold of $10^{-3}\sqrt{a_g d}$, i.e. any zone that has velocity $u < 10^{-3}\sqrt{a_g d}$. This quasi-static cutoff corresponds to a velocity that is less than 0.1% of the velocity at the opening.

As shown in Figure 5.2, inserts change the shape and reduce the size of these quasi-static zones. The proportion of the silo containing quasi-static material for each shape of silo using the base $\mu(I)$ model is given in Figure 5.10. As expected, the insert-free case has the largest proportion of the silo filled with quasi-static material. Both the downwards pointing triangle and the square have significantly higher quasi-static proportions. In part this is due to the flat surface at the top of the insert which creates an additional area where the material approaches the quasi-static limit. The portion of quasi-static material in this region (which we define to be $y > 75d$ and $|x - 75d| < 75d/2$) is shown in orange, while quasi-static material outside this region is shown in blue. The flat surface almost completely explains the extra quasi-static material for the down triangle, but the square insert has increased quasi-static proportion even without this area. The upwards pointing triangle has a particularly low quasi-static proportion. This is likely due to the wide base of the triangle forcing flow through the corners of the silo which would otherwise be quasi-static.

The impact of extensions on quasi-static areas is also important to consider. Figure 5.11 shows the comparison of the base $\mu(I)$ model with simulations using combinations of dilatancy

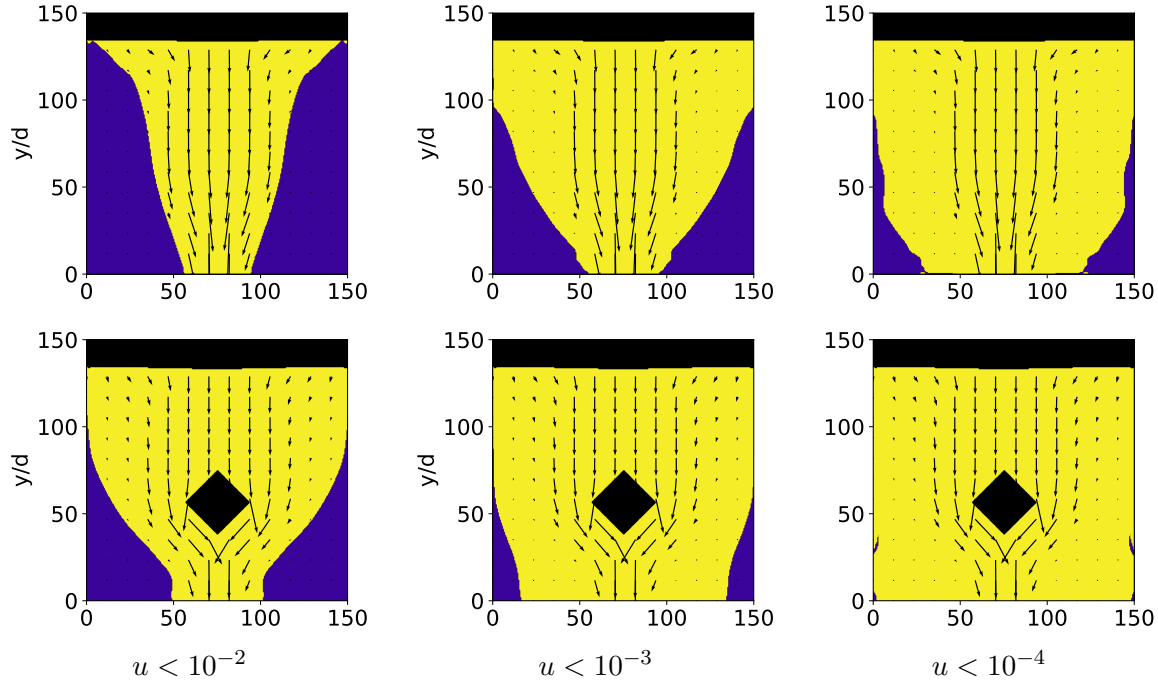

Figure 5.9: Quasi-static areas (blue) for different static thresholds. Static thresholds of $10^{-2}, 10^{-3}$, and 10^{-4} are shown for both the no insert and diamond insert case. All of these thresholds show a large reduction in quasi-static area due to the insert. The 10^{-3} threshold is chosen as a balance between overestimating near-static material and avoiding capturing creeping flow.

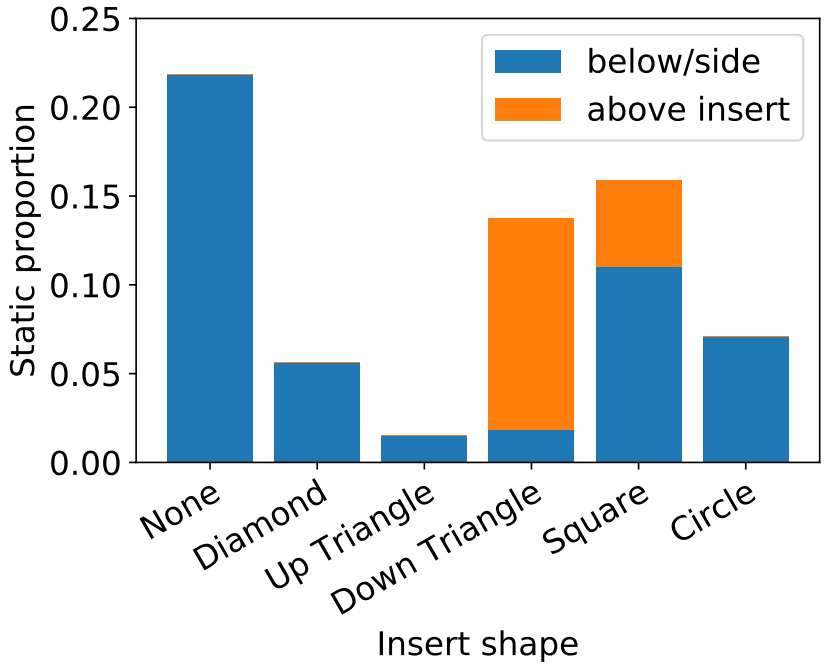

Figure 5.10: Proportion of the material in the silo that is quasi-static by insert shape. The quasi-static region is defined as any location where velocity is less than $10^{-3}\sqrt{a_g d}$. The quasi-static material directly above the insert ($y > 75d$ and $|x - 75d| < 75d/2$) is shown in orange, while quasi-static material at the sides or base of the silo is shown in blue.

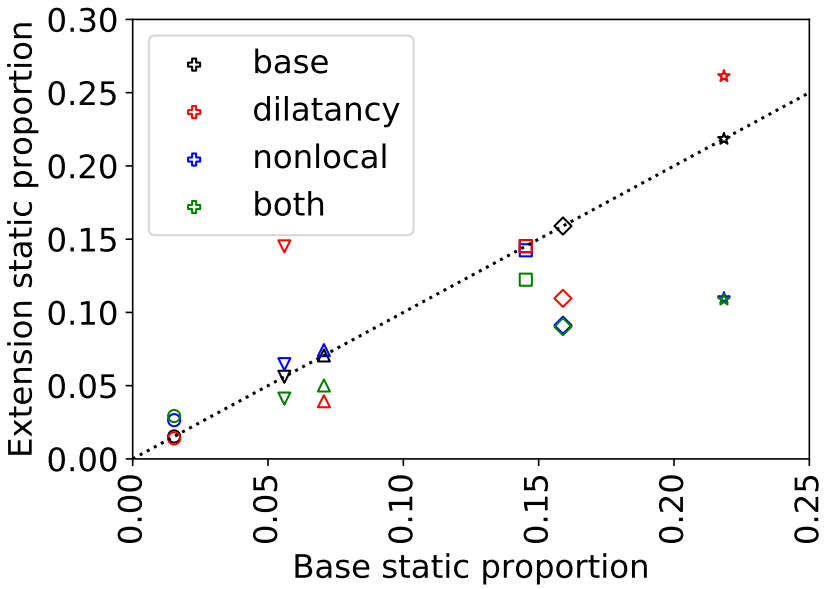

Figure 5.11: Proportion of the material in the silo that is quasi-static for different extensions by insert shape. The quasi-static region is defined as any location where velocity is less than $10^{-3}\sqrt{a_g d}$. The shape of the insert is indicated by the marker shape of the data (circle indicating circle insert, square indicating square insert, etc, with the star indicating no insert), with the colour indicating which extensions are enabled. The black points are by definition on the line $y = x$ (the dotted line), with vertical deviation indicating a difference caused by the extension(s). Note that the 'nonlocal' and 'both' cases nearly overlap for the diamond insert and the no insert cases, obscuring these points on the graph.

and nonlocal extensions. These show a much less consistent pattern than the flow rate shown in Figure 5.7, with different shapes interacting with extensions differently. Dilatancy increases the area of quasi-static material for both diamond and no inserts, but decreases it for circle and square inserts. The nonlocal extension has almost no effect except for the no insert and the square insert case, where it significantly decreases the quasi-static area. The presence of both extensions decreases the quasi-static area for most tested insert shapes, but particularly for the square insert and no insert cases.

5.2.2 Variable insert size

We have examined inserts of fixed size at a fixed height, however the size and location of inserts will also affect the flow rate and quasi-static zones. For examining these parameters we limit ourselves to the diamond shape insert, varying the location of the insert (measured from the

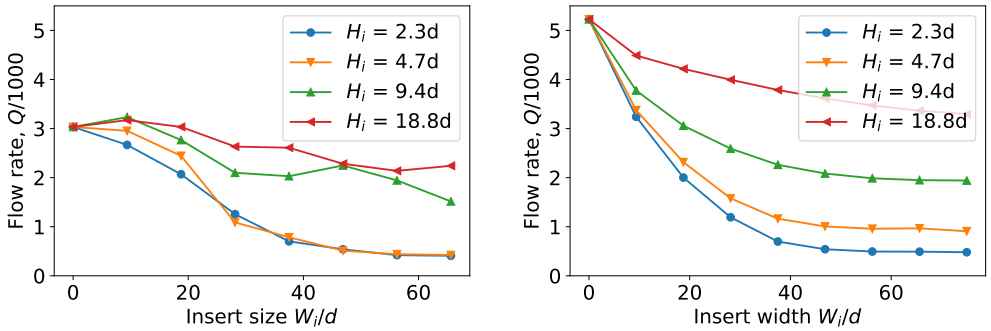

(a) Local $\mu(I)$ (b) Nonlocal fluidity

Figure 5.12: Flow rate $Q = \hat{Q}/\sqrt{a_g d^5}$ vs different diamond insert sizes at different heights. The base model is shown in (a), with (b) showing the flow rate when nonlocal effects are added.

height of the lowest point of the insert, H_i) and the size of the insert (indicated by the width W_i).

The flow rate for variable insert size and location is shown in Figure 5.12. When the insert is small the flow rate is relatively high with a larger insert decreasing the flow rate. This matches our intuition of a large obstacle near the orifice reducing flow more than a small obstacle far away from the orifice. This effect is stronger when the insert is located closer to the orifice. This matches the intuitive idea that the dynamics of the region near the orifice are the most important for determining flow rate.

For small inserts far away from the orifice in the local $\mu(I)$ model, the flow rate is actually increased compared to the silo with no insert. This may be because when the insert is far away it forces the flow to happen from the sides of the silo, which effectively mobilises more material increasing the amount of material attempting to approach the orifice. This increased flow is not seen when nonlocal effects are included. The flow rate of nonlocal silos is already higher than that of local silos, so the benefit of more material being 'mobilised' by the insert might already be provided by the nonlocal model spreading out the flow, explaining the difference between the local and nonlocal cases.

The quasi-static zones proportion is shown in Figure 5.13. Looking at the base case, for small widths (i.e. $W_i \approx 10d$), the height has a large impact on the quasi-static area, with inserts near the orifice showing almost no reduction in quasi-static area over the no insert case. For

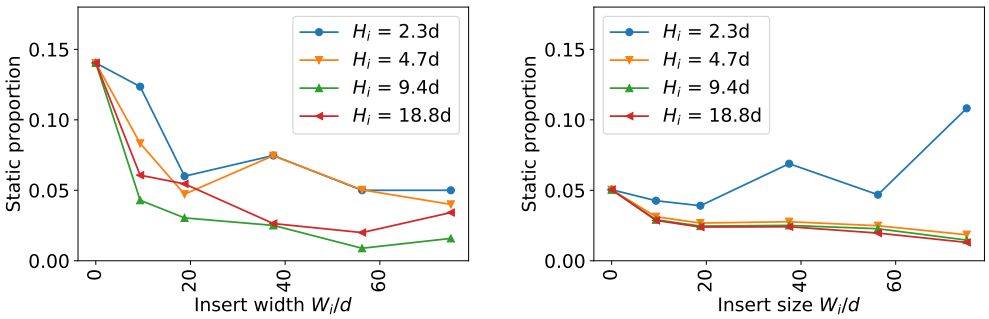

(a) Local $\mu(I)$ (b) Nonlocal fluidity

Figure 5.13: Static region vs different diamond insert sizes at different heights. The base model is shown in (a), with (b) showing the flow rate when nonlocal effects are added.

larger inserts the height is less important, but still impactful. For these larger inserts, lowering the insert gives a larger quasi-static area. This demonstrates that the insert has a maximum effective height for reducing quasi-static area. Above this height, increasing the width of the insert only increases flowing area by a small amount. The nonlocal case for large insert heights shows a similar decreasing trend with insert size, but with less volatility than the base case. The overall quasi-static values are also a lot lower since the fluidity works to spread out which areas are flowing. However for inserts close to the outlet, increased insert size actually increases quasi-static area. The flow rate in this case also becomes very low, indicating that the flow could be moving too slow to make a meaningful distinction between quasi-static and flowing material using this model. For the nonlocal model the flow rate depends on the insert height, while the quasi-static zone is relatively independent of insert height. This implies that we can achieve quasi-static zone reduction with minimal flow rate reduction by using inserts high in the silo.

5.3 Conclusions

A synopsis of the topics covered in this chapter is provided in the following bullet points:

- The $\mu(I)$ model was applied to silos with differently shaped inserts.
- Different shapes of inserts significantly affect the size and shape of quasi-static zones.
- Nonlocal fluidity and dilatancy were found to have complicated interactions with insert

shape when considering quasi-static zones.

- Nonlocal fluidity and dilatancy were found to affect the flow rate independently of insert shape.
- A small insert located high in the silo was found to greatly reduce quasi-static zone sizes with minimal reduction in flow rate.

We have tested the $\mu(I)$ model with dilatancy and nonlocal effects in silos with inserts. This model and extensions are capable of capturing information about the flow rate and quasi-static zones of granular material around various different shapes and sizes of inserts in a silo.

This model shows that extensions have a significant effect on flow rate, with nonlocal effects increasing the flow and dilatancy decreasing flow. Different shapes of inserts also change the flow rate behaviour significantly. Each of these factors seem to be independent of each other, with different combinations of extensions having approximately the same effect on flow rate for a circular insert as for a diamond insert or any other shape of insert. By contrast, the size of quasi-static area can change dramatically with different combinations of extensions and insert shapes. This shows that nonlocal effects and dilatancy are vital to calculating quasi-static zones, and any model wishing to accurately capture the effect on quasi-static zones would be highly dependent on these extensions.

We also examined insert size, showing that there is a reasonably sized insert which greatly reduces quasi-static areas without dramatically reducing flow rate, with larger inserts reducing flow rate without improving quasi-static behaviour significantly. The examination of the diamond insert indicates that when the insert is $\approx 10d$ above the opening and the insert is $\approx 20d$ wide for this silo, a large reduction of quasi-static zone reduction is achieved with minimal flow rate reduction. This information could be used to optimise silo flow in cases where static or slow moving material is a concern.

Chapter 6

Mixing granular materials

The distribution of multiple distinct types of granular materials in a domain is an important factor to consider for many applications of granular flow. In many industrial processes, it is desirable to have a homogeneous product, and as such the material is mixed to achieve the required consistency. Tracking the spread of material can be advantageous in case of contamination occurring within some process. Certain materials can also degrade with time, and as such ensuring material is processed in an adequate time frame is vital. In order to understand these behaviours a continuum granular model that can be used to track phases of material is desired.

Many mixing studies have been done in various domains, including flow down slopes [46], rotating drums or blenders [64, 22, 121], and silos [55]. Mixing in many domains can be measured directly [131], however for silos and silo-like domains much of the mixing that happens is due to the geometry rather than diffusion or similar factors [28, 120, 97]. For many applications of silos and silo-like domains, an important measure to understand is the residence time distribution [49, 115], which tracks the 'exit time' of material which starts partway up a silo [54, 84, 85] or in other arrangements [152]. Silos can often be adjusted to modify the residence time behaviour, particularly by the addition of inserts [34, 52, 119].

Different granular materials phases can also have different physical qualities. If a more frictional type of material is inserted below a type of material which is more free-flowing, the exit times of these materials could be significantly different. Segregation is a well known phenomenon,

where two different kinds of material (typically different sized granules) end up separating as they flow in drums [77], slopes [179], hoppers [105, 6, 103], and other complex domains [130, 31]. While the process of segregation is not modelled in this work, understanding the flow behaviour of distinct types of materials has important industrial applications.

In this chapter, the $\mu(I)$ model is used to track the mixing behaviour of granular material in a $2D$ silo. The domain is also extended to include multiple orifice silos; the impact of mixing and residence time are measured and analysed in these more complex domains. The analysis is also done in the presence of different types of material, with different parameters for the $\mu(I)$ rheology and different strengths of extension parameters.

6.1 Residence time and cumulative distribution

In order to analyse the mixing behaviour of these silos we examine the cumulative distribution $F(t)$, which is closely related to the residence time distribution $E(t)$. The cumulative distribution can represent the mixture of material emitted at a given time for a silo with a 'step change' of material, while the residence time distribution represents the distribution of time taken for a 'pulse' of material to travel through the domain. Each of these represents a measure of how long it takes for material to transit through the silo (i.e. the distribution of residence times for given units of material). These two distributions can be derived from each other by the relation [49]

$$F(t) = \int_0^t E(t)\,\mathrm{d}t. \tag{6.1}$$

The ideal residence time distribution can be measured directly from a steady state flow with a tracer pulsed at time $t = 0$, and the flow of tracer measured until all of the tracer has passed through the silo. The concentration of the material is measured at the exit point, with the flow rate of tracer over time forming the residence time distribution. Given a concentration of tracer over time $C(t)$, the residence time distribution $E(t)$ is just normalised concentration distribution, i.e.

$$E(t) = \frac{C(t)}{\int_0^\infty C(t)\,\mathrm{d}t}. \tag{6.2}$$

For a granular silo a true steady state is difficult to form, but $C(t)$ can be approximated experimentally by placing a thin horizontal line of tracer material (which could be material which is dyed a different colour or some similar process) in a silo some distance above the opening, representing the pulse of material followed by the steady flow of non-tracer material.

The cumulative distribution can be found in a similar manner by considering a 'step change' in flow. Rather than a thin layer of material at a given height that is marked as a tracer material, instead all material above that height is tracer material. This attempts to replicate a steady flow of material where the type of material entering the silo after $t > 0$ is instantaneously switched to the tracer. The flow rate of tracer over time at the exit point then forms the cumulative distribution, with the test ending when the flow rate of tracer is sufficiently close to the flow rate of the overall material.

For the purposes of this work, the step change is used to analyse the mixing behaviour. This is demonstrated in Figure 6.1, with tracer displayed in yellow and non-tracer material displayed in blue throughout the chapter. The step change experiment can mimic certain industrial problems, such as a storage silo where new product is loaded above old product potentially leading to degraded product contaminating newer product. Also if the second material has different physical properties, such as more or less surface friction, the step change model can account for these by modifying the model parameters where the tracer is present as discussed in Section 6.2.2.

For the step change silos without replacement used in this work, there are expected limits on what behaviour the cumulative function will show. In the limit of a perfectly mixed silo, the cumulative distribution should be a constant value, with the exiting material always being a perfect mix of the two components. For a perfectly unmixed silo (i.e. first material in is the first material out), the cumulative distribution would be a step change from zero to a constant value; the material emitted by the silo would initially be purely the non-tracer component, which would continue until all the non-tracer material is drained, at which point the silo switches instantaneously to emitting pure tracer. A realistic silo would be expected to have behaviour between these two extremes, similar to a logistic curve with a smooth transition from zero up to some non-zero constant. Another factor to note is that for a non-replacing silo, the flow

rate is also not constant. After some time the silo drains to the point where the orifice is not saturated with granular material, meaning the flow rate drops. The initial flow also requires a small amount of time to reach the constant flow, although this is when the tracer is well away from exit so the effect on the residence time is negligible. In order to account for the dropped flow rate the total emitted material is used as a substitute for time. Nonetheless, most of the flow happens before the silo drains and the flow rate drops, so the focus of the analysis is done on the time before the drop.

6.2 Step change tracer simulations

The mixing behaviour is examined by implementing a 'step change' distribution of tracer. An inert tracer is incorporated into the volume of fluid methods. The tracer 'follows' the material, and tracks where the specific material moves in the silo via advection. The tracer is tracked using the volume-of-fluid method as described in Appendix B.

The initial state of the silo is static material. The silo contains non-tracer material in the bottom half ($y < 75d$) and tracer material to 90% full ($75d < y < 135d$). The top 10% is filled with air. The $\mu(I)$ parameters (μ_s, $\Delta\mu$, I_0) are set to be (0.62, 0.48, 0.6) respectively. Pressure is initially set to hydro-static pressure, with a region of zero pressure near the orifice to aid initial flow stability.

The flow vectors and tracer distribution at four key points in time are given in Figure 6.1. Initially only the non-tracer material is emitted from the silo. The tracer is trapped above the other material until approximately $t \approx 5\sqrt{d/a_g}$, where tracer begins to reach the orifice and a mix of material is emitted. The portion of the orifice covered by tracer then widens until it near-saturates at approximately $t \approx 10\sqrt{d/a_g}$. From here the amount of tracer in the silo rapidly decreases until approximately $t \approx 20\sqrt{d/a_g}$, at which point most of the tracer within the silo has drained. After this time, non-tracer material dominates the orifice and drains more readily until the silo empties of all material.

We examine both the total emitted material and total emitted tracer from the silo over time, shown in Figure 6.2. While the ideal cumulative distribution requires that the flow rate of the

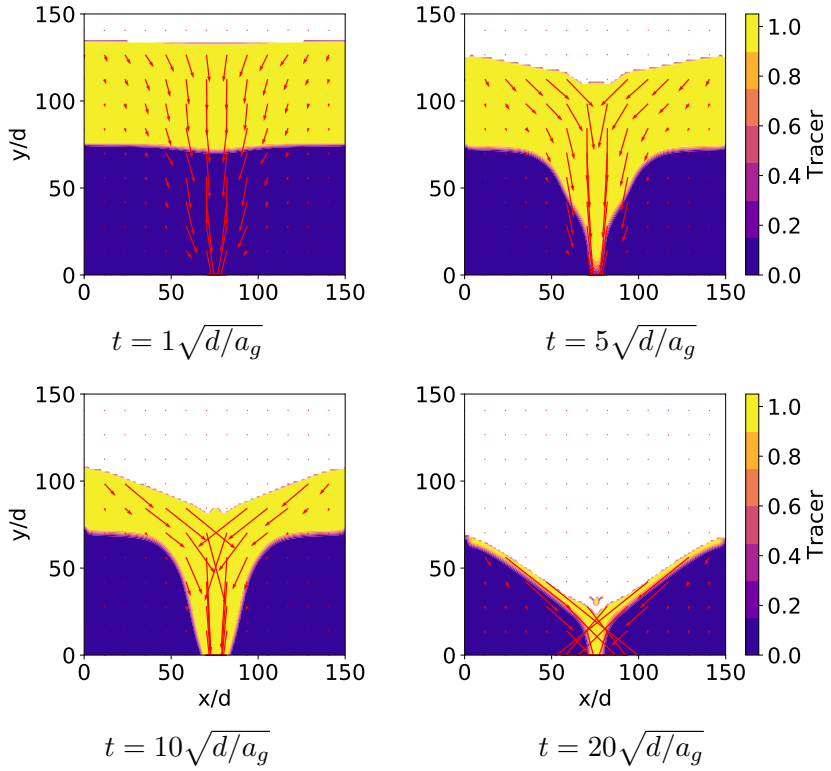

Figure 6.1: Tracer in silo over time. The tracer initially is placed in the top half of the silo and allowed to drain. The arrows indicate the flow direction and magnitude. Tracer material has identical properties to non-tracer material.

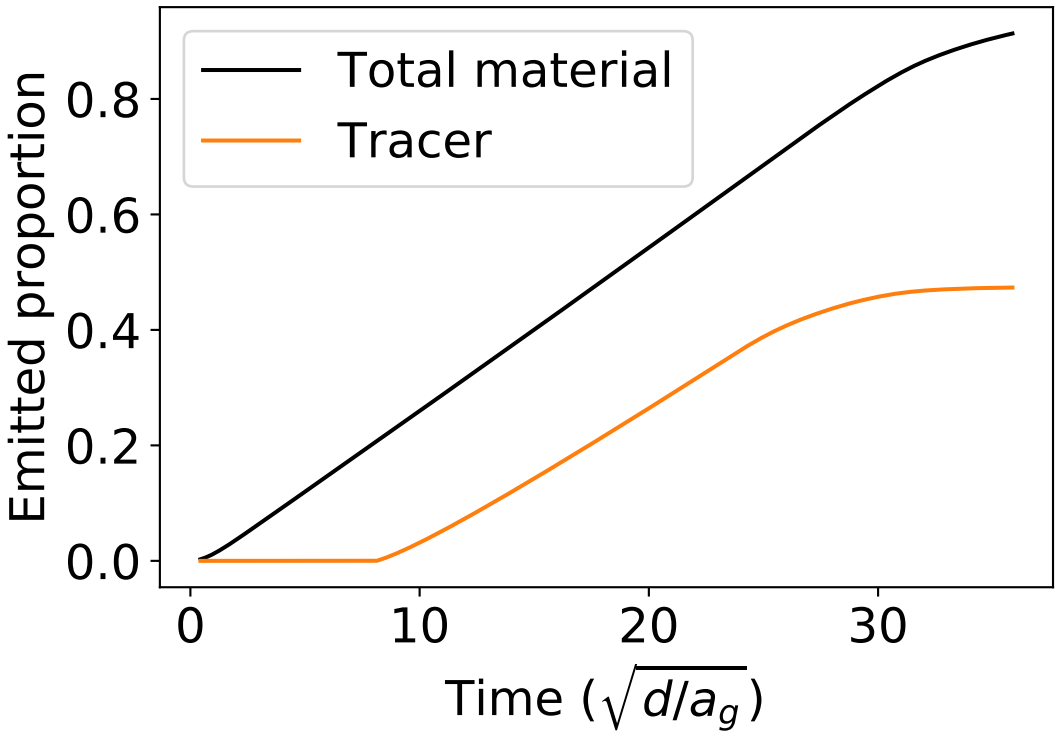

Figure 6.2: Quantity of material emitted from the silo over time for both all material and tracer material. The straight line for the material demonstrates the validity of the assumptions required to use the tracer for the cumulative function.

entire material is constant, this is not the case for this domain since the material is not in motion initially and as the silo drains the flow rate reduces. Fortunately the initial startup time is small ($t \lessapprox 1$), and occurs before tracer begins to be emitted from the silo. The total flow rate slow down occurs after approximately $t \approx 30\sqrt{d/a_g}$, which is after the tracer flow rate begins to slow as the tracer is almost fully expelled from the silo. For times $10\sqrt{d/a_g} \lessapprox t \lessapprox 25\sqrt{d/a_g}$, both total flow rate and tracer flow rate are nearly constant, with tracer flow rate slightly lower than total material due to some non-tracer material being emitted. This validates the assumptions required to use this simulation to form an approximation to the true cumulative distribution.

The cumulative distribution $F(t)$ can be found by taking the first order numerical derivative with respect to time of the distributions in Figure 6.2. This is given in Figure 6.3 for both tracer and overall material. This shows the short startup time more clearly, and shows the decay after $t \approx 30\sqrt{d/a_g}$. Also note that at $t \approx 30\sqrt{d/a_g}$ the flow is slightly noisy. This occurs when the orifice is no longer fully covered in granular material, causing the flow to oscillate slightly.

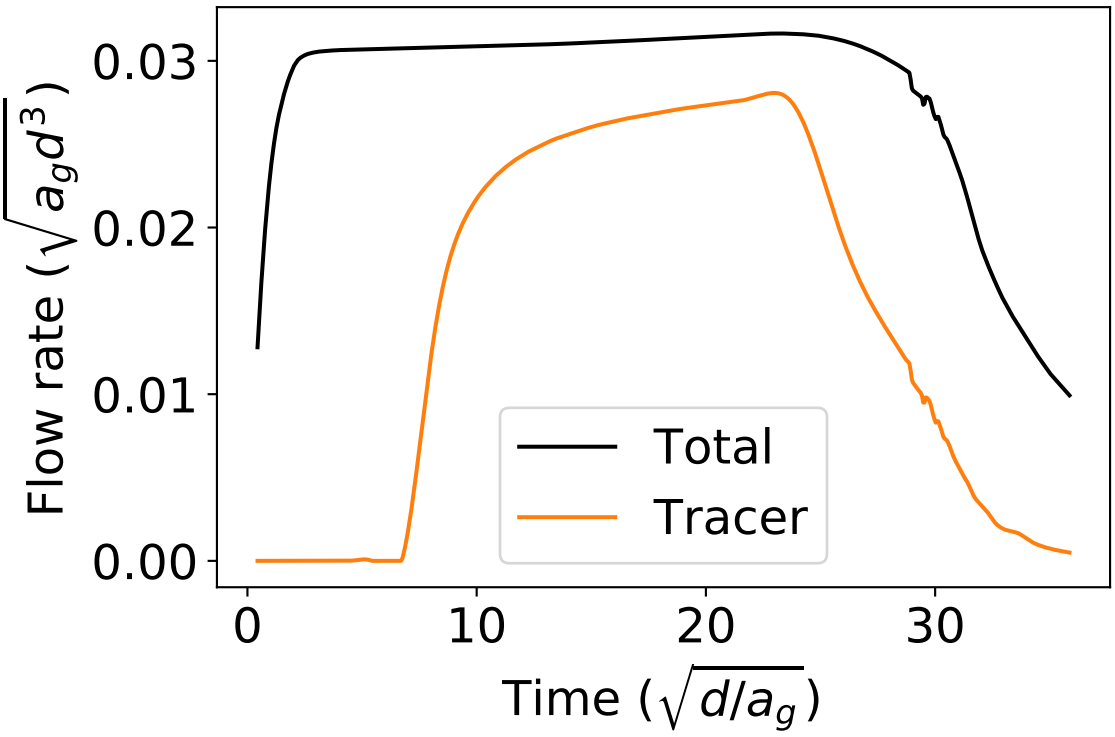

Figure 6.3: Flow rate of emitted material in the silo over time for both all material and tracer material, giving the cumulative distribution $F(t)$.

However, the key area is between $t \approx 1\sqrt{d/a_g}$ and $t \approx 30\sqrt{d/a_g}$, where the material flow is fully developed and near-constant. This area gives the bulk of the tracer flow, and we can use this to analyse the mixing of the material within the silo. The tracer flow rate rises quickly and reaches near the total flow rate which is characteristic of a 'first in, first out' flow pattern where initially lower material is always emitted before higher material, although some mixing does occur.

To account for the reduced flow rate after $t \approx 30\sqrt{d/a_g}$ and the slight variations in flow rate, the fraction of emitted tracer compared to emitted material is used. In addition we can use the portion of total volume drained in place of time to allow for easier comparison to silos with different flow rates. The resulting normalised tracer cumulative distribution is given in Figure 6.4.

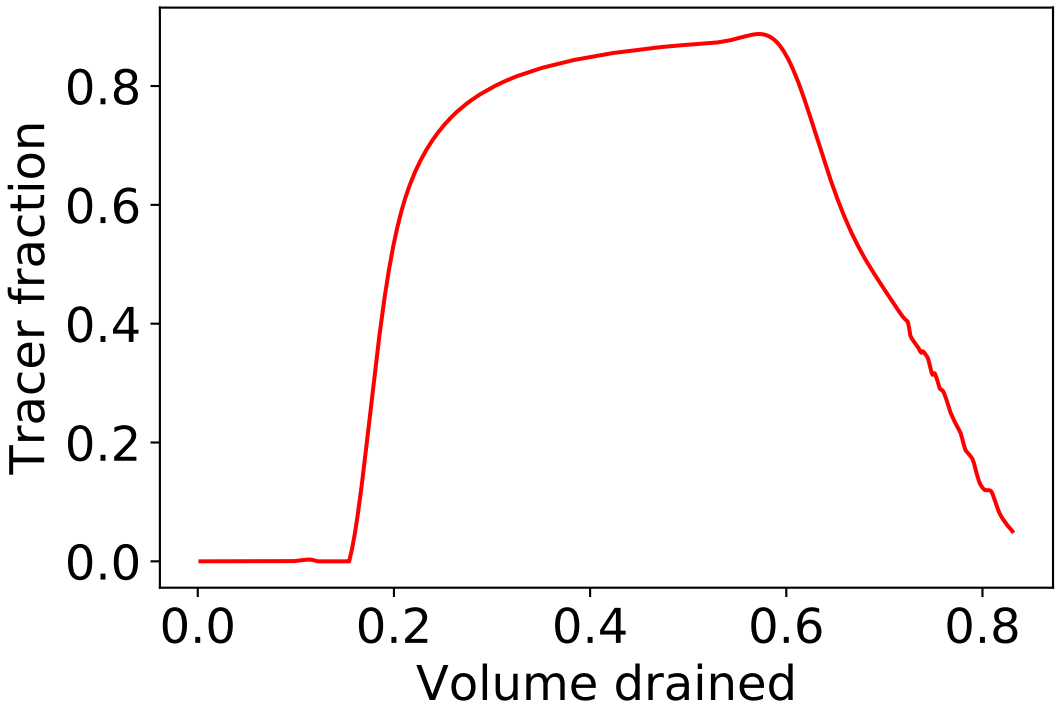

Figure 6.4: Portion of emitted tracer material normalised by total emitted material as the silo drains, giving the normalised tracer distribution.

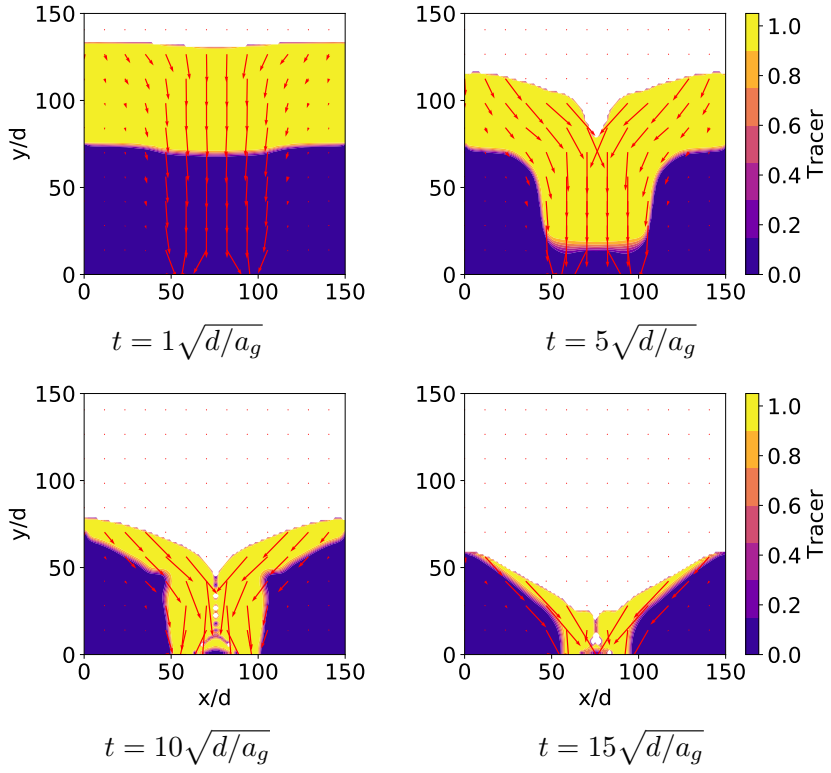

Figure 6.5: Tracer in a double slot silo (with separation $L = 75d/4$) at various times. The tracer initially is placed in the top half of the silo and allowed to drain. The arrows indicate the flow direction and magnitude. Tracer material has identical properties to non-tracer material.

6.2.1 Mixing in other modified silos

The two orifice silo, as discussed in Section 4.3, can exhibit some unusual flow behaviour. The two opening silo shows a dip in flow rate, where any non-zero separation between orifices significantly decreases flow rate but a small non-zero separation decreases the flow rate more than larger separations. This more complex flow behaviour could have an impact on the mixing behaviour as well.

Snapshots of the double slot silo at various times are given in Figure 6.5, while the normalised tracer distribution for different separations is shown in Figure 6.6. The zero-separation (i.e. single orifice with double width resulting in the highest flow rate) case has less material emitted before tracer begins to drain than any of the other cases, with increased separation increasing the volume of material that has to drain before the tracer begins to be emitted. This indicates that multiple openings reduce mixing and contribute towards maintaining a ‘first in first out’

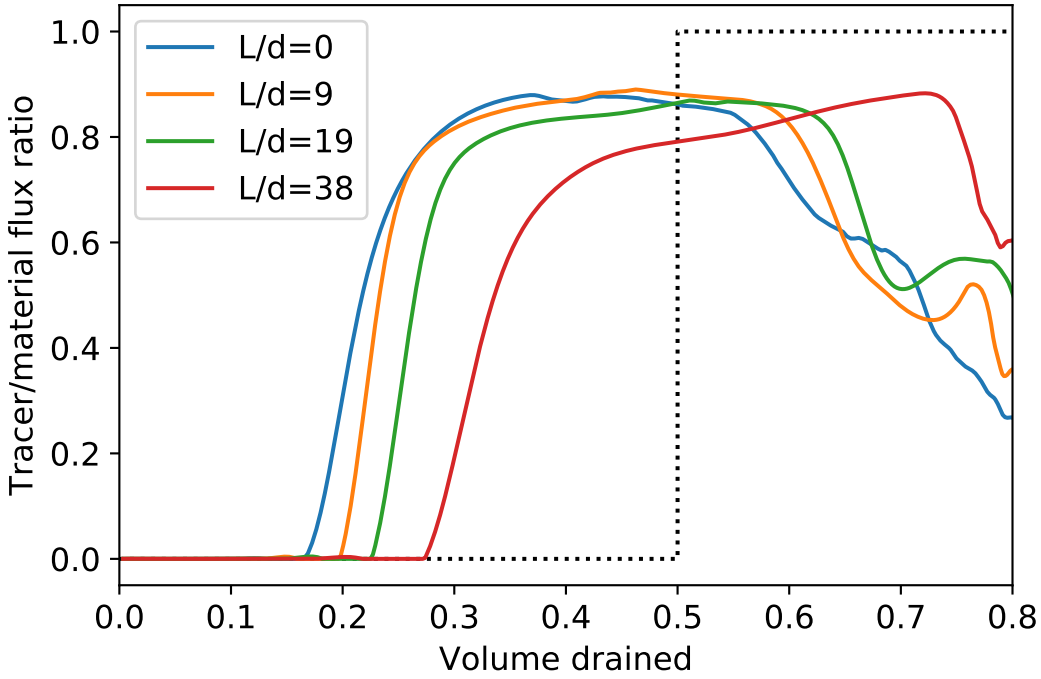

Figure 6.6: Normalised tracer distribution for a double slot silo with various orifice separations L/d. The dotted line indicates the theoretical 'first in first out' zero mixing case, with larger deviations from this line indicating more mixing inside the silo.

flow pattern, with larger separations having a stronger impact. The monotonic shift in the start point of the tracer flow indicates that unlike the flow rate (which can exhibit dipping behaviour), the mixing behaviour seems to have a monotonic response to the separation of the orifices.

Triple opening silo

While many silo-like domains have one orifice, many important domains, such as draw-point mines [124], are similar to a silo with multiple openings. The triple slot silo further develops the pattern of increasing the number of openings from the two orifice silo. Snapshots of the tracer in a triple opening silo with opening widths $W = 75d/16$ and separation distance $L/d = 19$ are given in Figure 6.7.

The triple opening makes the tracer act more as a cohesive whole, with the interface between the tracer and non-tracer coming down as a 'line' rather than as a 'point'. This makes the silo act more like a 'first-in first-out' unmixed silo, which is reflected by the steep slopes in the

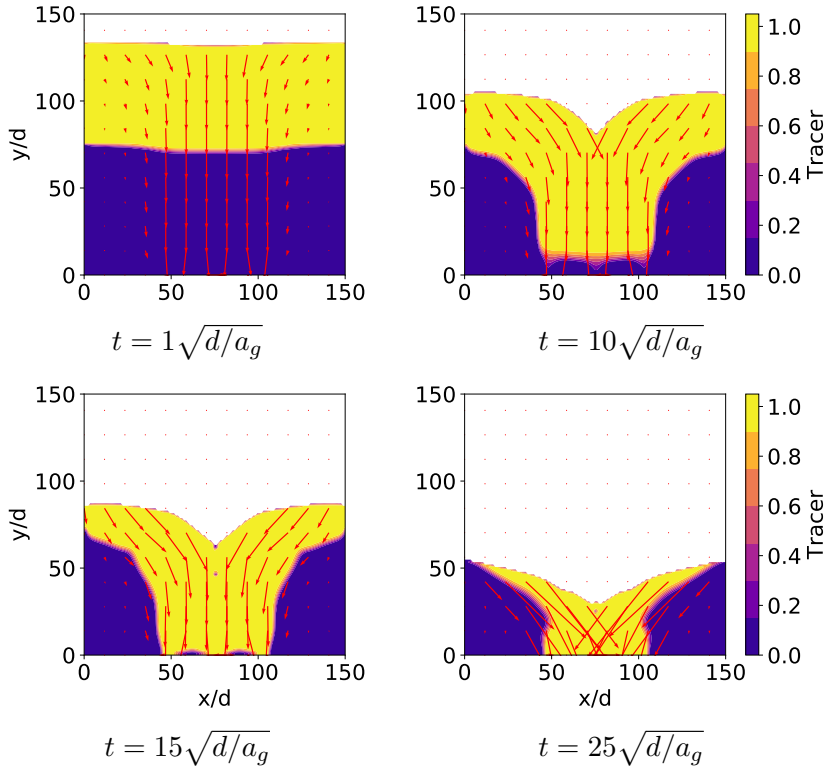

Figure 6.7: Tracer in triple opening silo over time. The tracer initially is placed in the top half of the silo and allowed to drain. The arrows indicate the flow direction and magnitude. Tracer material has identical properties to non-tracer material.

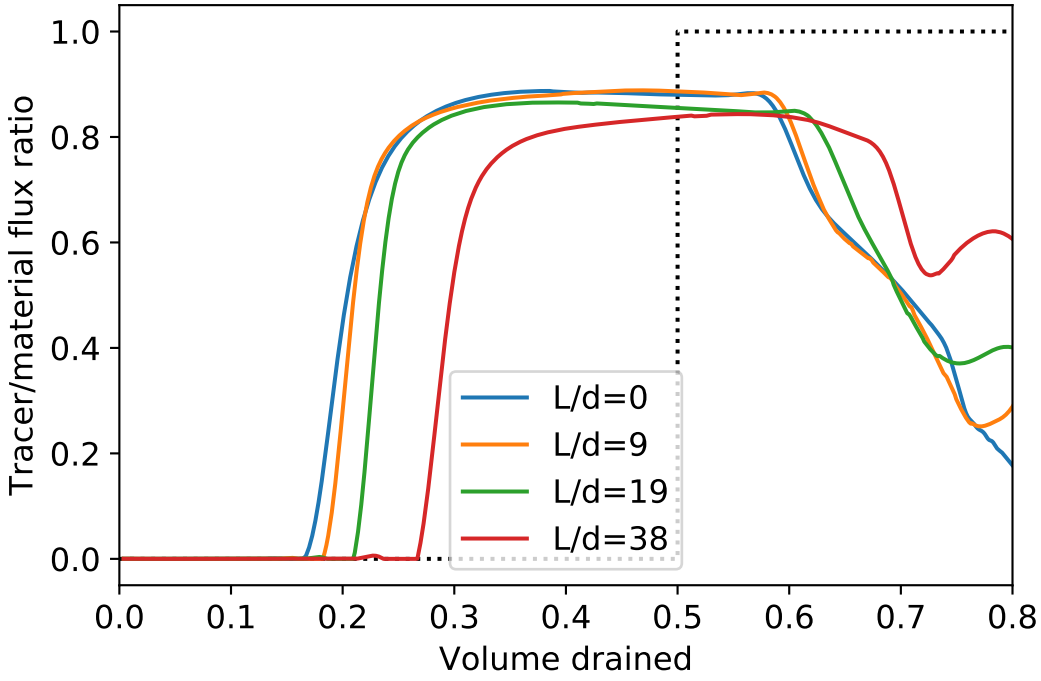

Figure 6.8: Normalised tracer distribution for a triple slot silo with various orifice separations L/d. The dotted line indicates the theoretical 'first in first out' zero mixing case, with larger deviations from this line indicating more mixing inside the silo.

cumulative function shown in Figure 6.8. Both of the low separation cases (i.e. $L/d = 9$ or 19) give steeper slopes than the zero separation (i.e. single opening) case. However when the separation is increased further to $L/d = 38$, the slope of the line is more similar to the zero separation case. This could either be due to the orifices being far apart enough to have reduced impact on the flows of the neighbouring orifices, or due to the influence of the side walls being stronger when orifices are closer to the sides. A similar slope pattern occurs in Figure 6.6 with the double slot silos, indicating that this transition is not confined to just double or triple opening cases.

Another impact of changing the separations is the amount of material that has to drain before tracer starts to drain. Given the initial step change distribution of tracer chosen for these simulations, the zero-separation and small-separation cases require approximately 20% of the material drain before the tracer begins to drain, while the larger separation cases require approximately 30% of the material to drain before the tracer reaches the orifice. This likely

occurs due to the wider area of material that is strongly influenced by the orifices, leading to a larger 'plug' of flow that needs to be drawn in before the tracer reaches the orifice.

Uneven double silo

Another possible domain that may need to be analysed is an uneven opening silo, where one opening is wider than the other. This could occur in a double opening silo where one opening is partially blocked, or could occur in a single opening silo where a 'leak' occurs. Snapshots of an uneven silo with opening widths $W = 75d/16$ and $W = 3 \times 75d/16$ (i.e. the $1:3$ ratio of width sizes) with separation between the orifices $L = 75d/2$ are given in Figure 6.9.

The differing opening widths lead to interesting interactions. Material is mostly drawn to the larger orifice, while a smaller proportion of material is drawn to the smaller orifice. Figure 6.10 shows the cases of a silo with openings of width $W = 2 \times 75d/16$ and $W = 3 \times 75d/16$ (i.e. the $2:3$ ratio case) and a silo with ratios $W = 75d/16$ and $W = 3 \times 75d/16$ (i.e. the $1:3$ ratio case). The separation between the two openings are varied. The $2:3$ ratio case mostly shares characteristics with the ordinary double slot case, however for large separations the tracer seems to have a double step change. The flow of tracer towards the larger orifice in proportion to the overall material flow rate occurs at a similar rate as the ordinary double slot case, leading to a similar 'step change' in the cumulative distribution at a similar point in the draining profile. However, the smaller orifice also has a slower flow towards it. As such, the tracer reaches the small orifice at a later point in the draining profile than the large orifice, creating two distinct areas where the emitted tracer flow rate increases. The $1:3$ case does not have a pronounced step, which agrees with the contours in Figure 6.9 that show the wider orifice dominates the flow and the tracer does not reach the smaller orifice. However, the large step change does not reach the maximum value immediately, and the tracer flow rate increases significantly over the drain cycle for the larger separations.

6.2.2 Differing material properties

When multiple loads of material with different sources are stored in a silo, there is a possibility of these materials having different physical qualities that cause them to flow differently. This

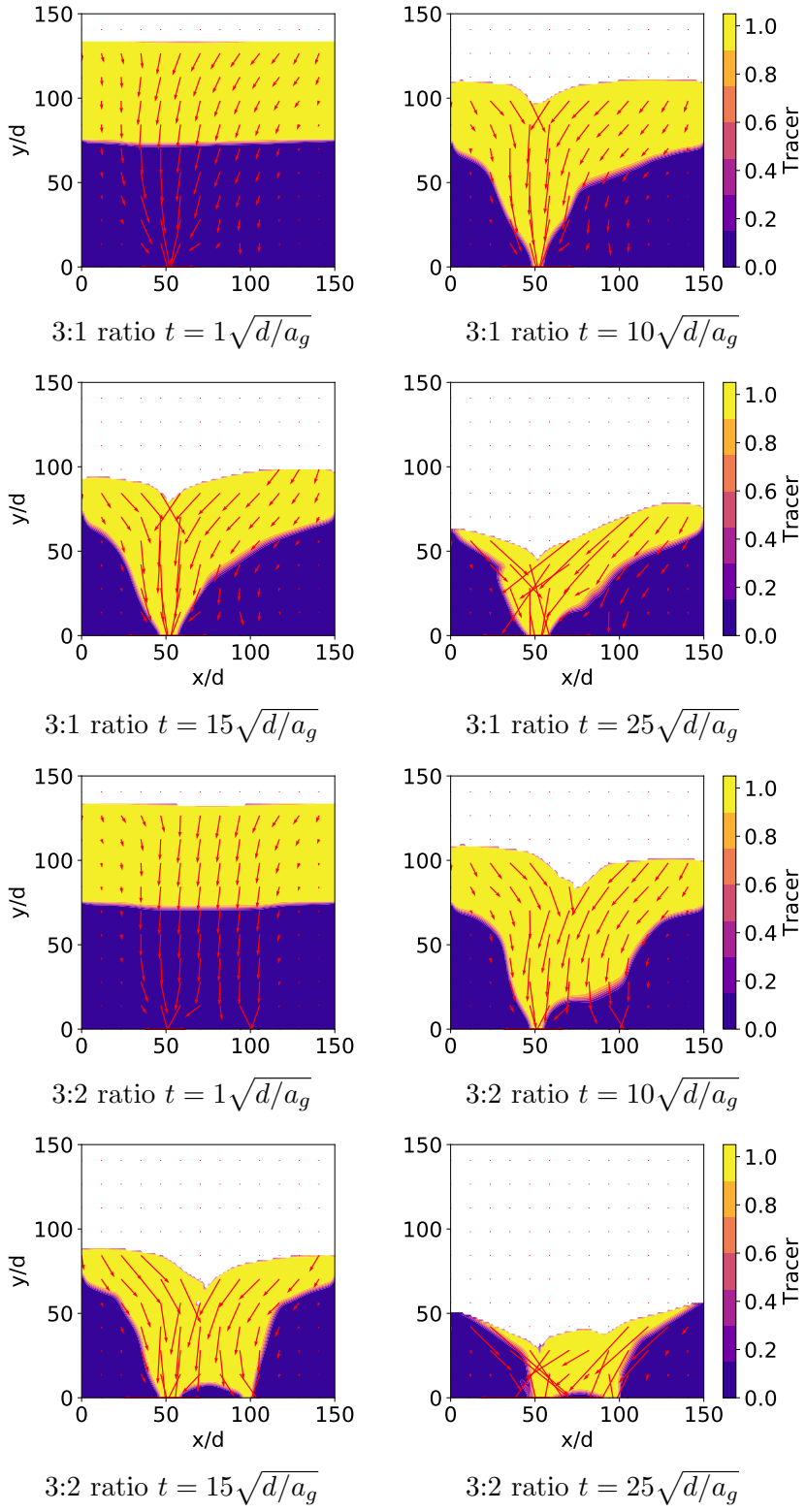

Figure 6.9: Tracer over time in double opening silos with different opening widths. The left orifice is $\frac{450}{32}d$ wide, and the right orifice is $\frac{150}{32}d$ (3:1 ratio top) and $\frac{300}{32}d$ (3:2 ratio bottom) The tracer initially is placed in the top half of the silo and allowed to drain. The arrows indicate the flow direction and magnitude. Tracer material has identical properties to non-tracer material.

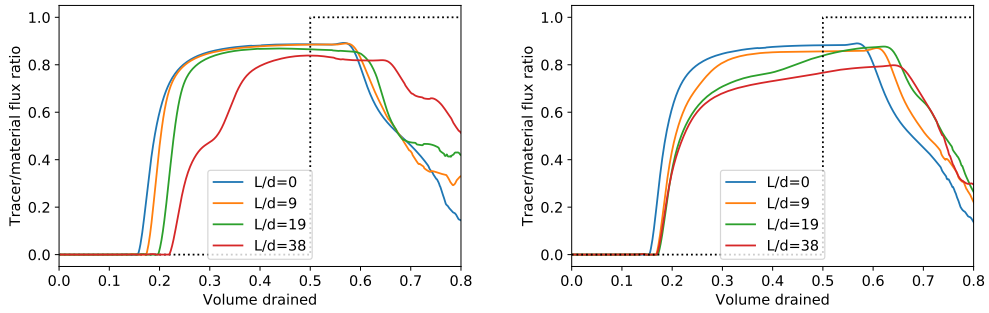

2:3 ratio 1:3 ratio

Figure 6.10: Normalised cumulative distribution for an uneven double slot silo. Both cases have one orifice with width $W = 3 \times 75d/16$, while the other orifice has width $W = 2 \times 75d/16$ for the $2:3$ case and $W = 75d/16$ for the $1:3$ case. The tracer initially is placed in the top half of the silo and allowed to drain, and tracer material has identical properties to non-tracer material.

can also occur with a single source of material, where segregation occurs in the processing of the material before storing it in the silo which leads to areas with variation in the physical quantities and distinct flow behaviour. As such, a model with different parameters for tracer, non-tracer, and blends of materials is required to simulate these situations.

For this work, a blend of material is assumed to have a linearly weighted average of the parameters of the two different materials [21]. A blend of two materials with different $\mu(I)$ parameters (μ_{s_1}, $\Delta\mu_1$, I_{0_1}) and (μ_{s_2}, $\Delta\mu_2$, I_{0_2}) will have an effective $\mu(I)$ parameter set defined by

$$\mu_s = (1-c)\mu_{s_1} + c\mu_{s_2}, \tag{6.3}$$

$$\Delta\mu = (1-c)\Delta\mu_1 + c\Delta\mu_2, \tag{6.4}$$

$$I_0 = (1-c)I_{0_1} + cI_{0_2}, \tag{6.5}$$

where c is the proportion of the second material in the blend of material, with $c = 0$ indicating pure unblended material of the first kind and $c = 1$ indicating an area of purely the second kind of material. A silo containing material with $c = 0.5$ everywhere in the silo would be identical to taking an average of the parameters of the blended material. The linear relationship is assumed based on simulations done in DEM shear cells [21]. While it is possible that a more complicated domain may require a non-linear relationship in blended material, the focus of this section is

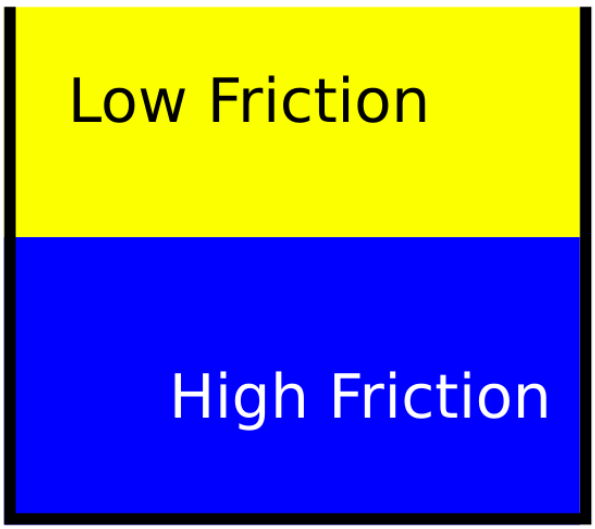

Figure 6.11: Diagram of initial material distribution. A layer of low friction material is initially laid over a layer of high friction material.

mixing of initially separated materials. While simulations involving highly blended materials or modelling segregation could be sensitive to the model used for blended materials, this is not the case for simulations done in this work. For the step change initial distribution used for simulations in this work, the material remains almost completely unblended except along the thin interface of the two materials. As such the impact of the model used for blended material behaviour is minimal, meaning that the linear assumption suggested by the DEM is sufficient for this work.

We simulate two different materials stacked on top of each other with low friction tracer material stacked above high friction non-tracer material, as depicted in Figure 6.11. The $\mu(I)$ parameters (μ_s, $\Delta\mu$, I_0) of these materials are chosen as (0.47, 0.38, 0.6) for the low friction tracer material, and (0.77, 0.58, 0.6) for a high friction material. The cumulative distribution is given in Figure 6.12.

Contours of the high friction and low friction materials are given at key times in Figure 6.13. The cumulative function shows that the low friction material is initially being trapped above the high friction material, emitting material in an almost identical fashion to a silo with only high friction material within. This continues until the low friction tracer reaches the orifice, which happens at $t \approx 5$. After the low friction material reaches the orifice, the total flow rate

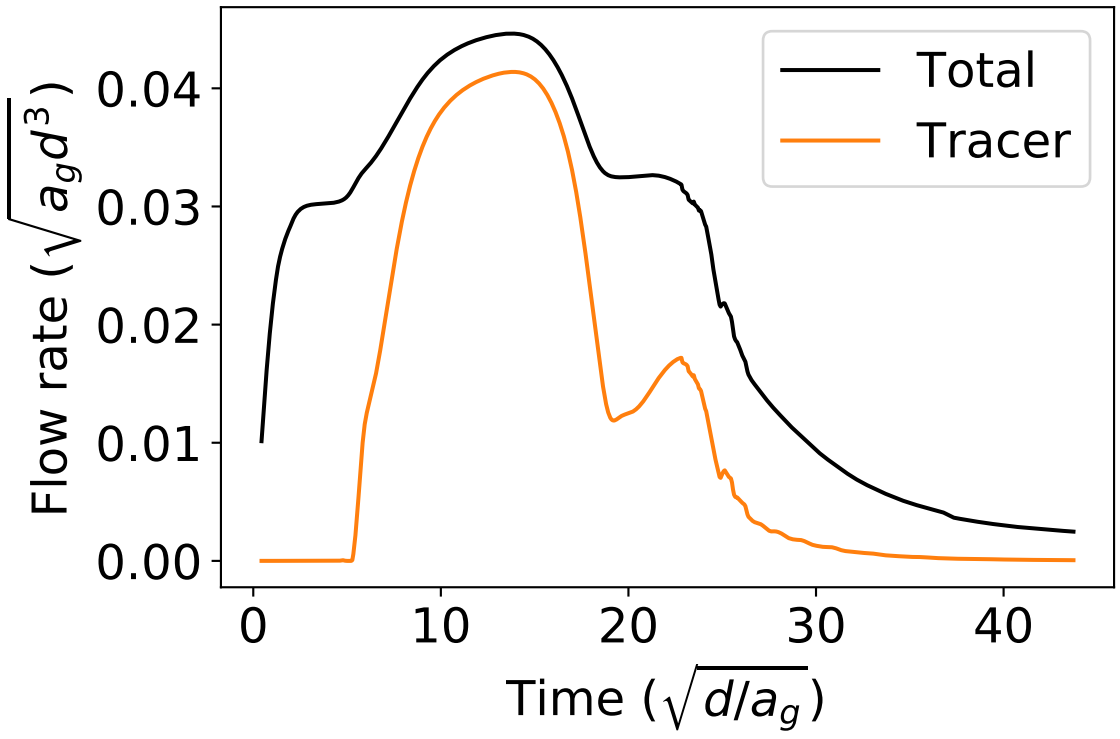

Figure 6.12: Cumulative distribution for a silo with initial material distribution of lower friction tracer material above higher-friction non-tracer material.

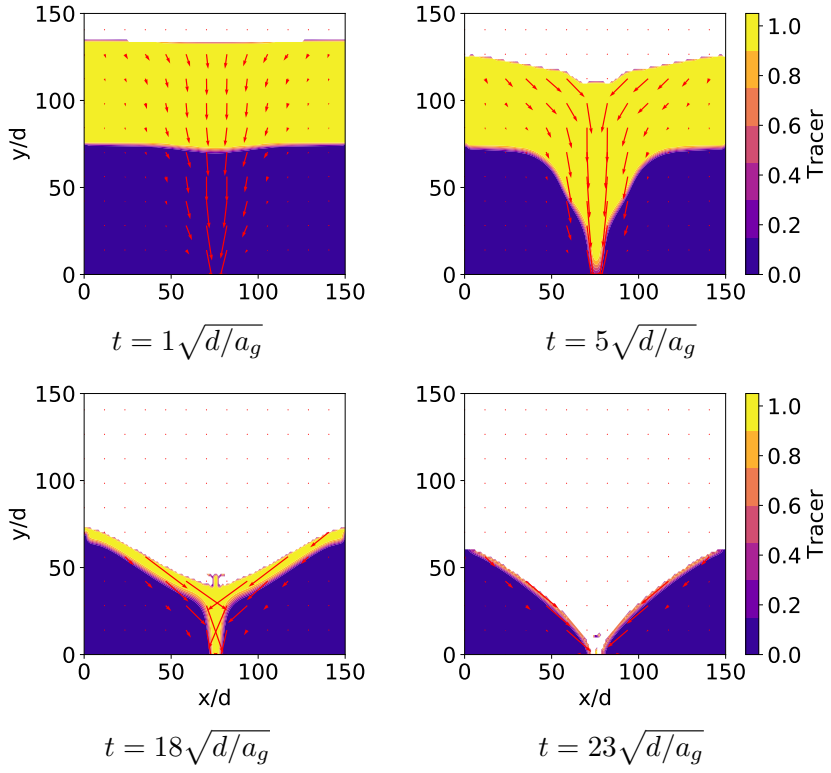

Figure 6.13: Materials with different frictional parameters layered on each other in a silo. The lower friction material (μ_s, $\Delta\mu$, I_0)=(0.47, 0.38, 0.6) is initially is placed in the top half of the silo and high friction material (μ_s, $\Delta\mu$, I_0)=(0.77, 0.58, 0.6) in the bottom half of the silo. The arrows indicate the flow direction and magnitude.

rapidly increases as the lower friction material flows through the orifice more easily. Once the bulk of the low friction tracer has been expelled at $t \approx 18$, the flow rate returns to a similar value as before the tracer broke through, before beginning to decay at $t \approx 23$ as the silo runs out of material.

Normalising the cumulative distribution in the same manner as done for the inert tracer case (seen in Figure 6.4) allows for the comparison in Figure 6.14. The different material friction case results in the tracer being emitted significantly sooner and at a higher proportion than the inert tracer medium friction case. This higher proportion continues until about 60% of the material is drained, at which point the proportion of tracer sharply drops for the different friction case. Shortly afterwards the bulk of the silo is drained and the two cases exhibit similar behaviour as the tracer proportions converge. This occurs as the flow rates decrease as the majority of the material has left the silo and the emitted material slowly eases in from the side.

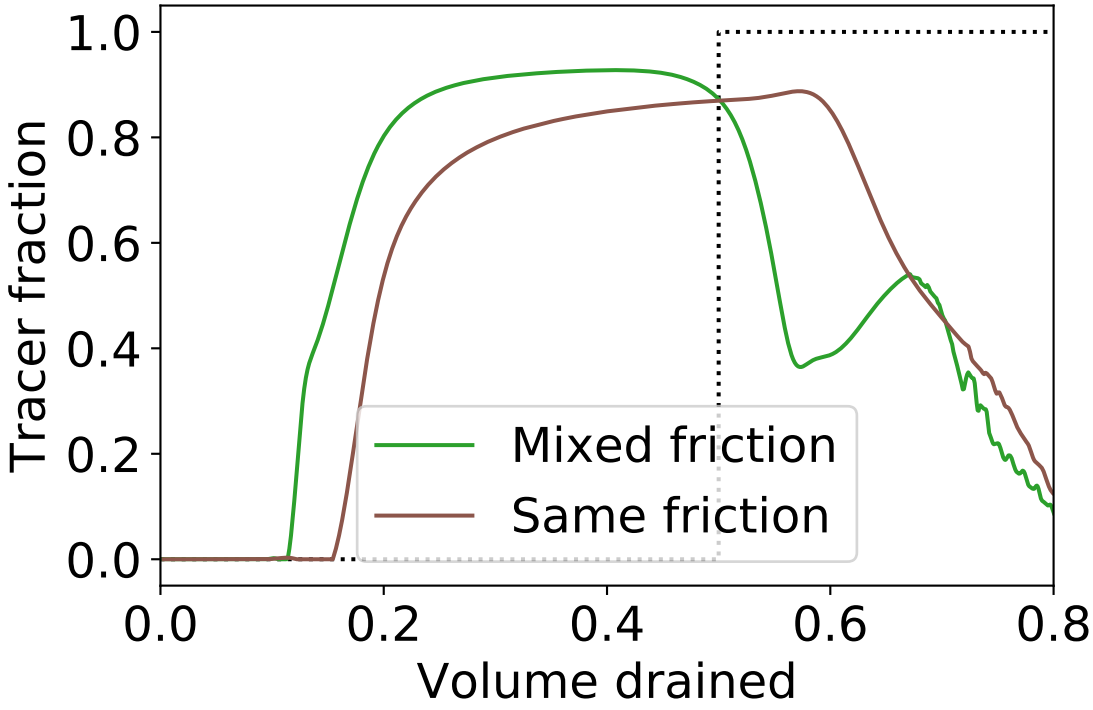

Figure 6.14: Cumulative distribution normalised by flow rate for a silo with initial material distribution of lower friction tracer material above higher-friction non-tracer material compared to a silo with an inert tracer in a medium friction material.

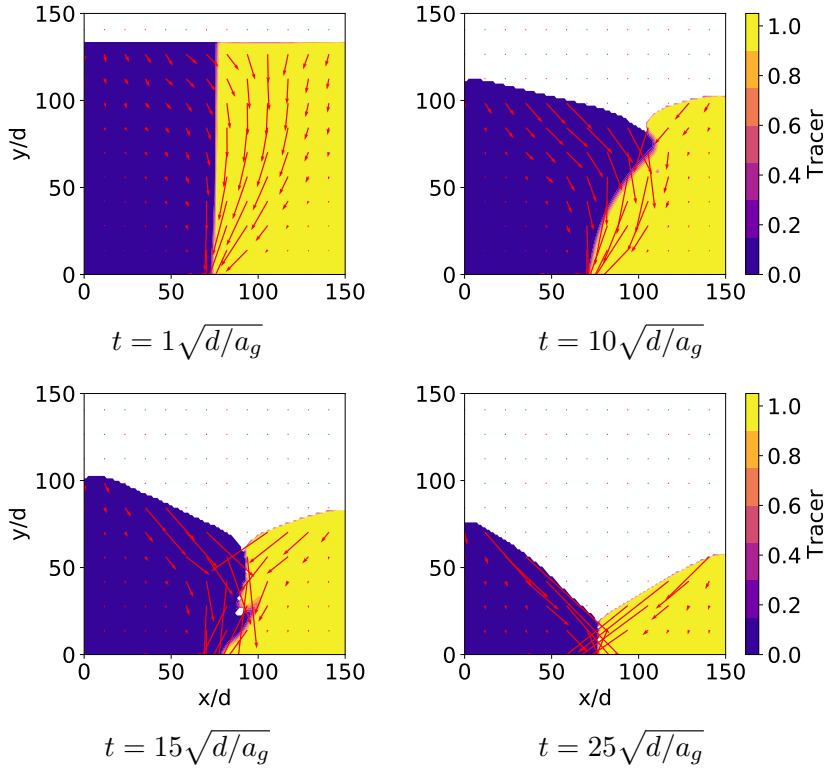

Figure 6.15: Tracer in silo over time for side-by-side split silo with different friction values. The arrows indicate the flow direction and magnitude. The tracer (right) indicates low friction material with $(\mu_s, \Delta\mu) = (0.47, 0.38)$, while the non-tracer material (left) indicates high friction material with $(\mu_s, \Delta\mu) = (0.77, 0.58)$.

6.3 Side-by-side tracer distribution

Material can naturally become vertically segregated via a variety of physical phenomena, however other distributions of material could occur. In this section we test the side-by-side split silo, where the silo materials are different on each side of the silo.

We define a silo that is initially filled with tracer on the right half of the silo and non-tracer material on the left half. The tracer is set to have lower friction parameters $(\mu_s, \Delta\mu, I_0) = (0.47, 0.38, 0.6)$, while the non-tracer material has higher friction parameters $(\mu_s, \Delta\mu, I_0) = (0.77, 0.58, 0.6)$. Contours for this side-by-side silo over time are shown in Figure 6.15 with velocity vectors.

The flow rate behaviour for the split silo is shown in Figure 6.16. Initially the flow favours the side with tracer, as the lower friction material gives less resistance to flow. As the flow

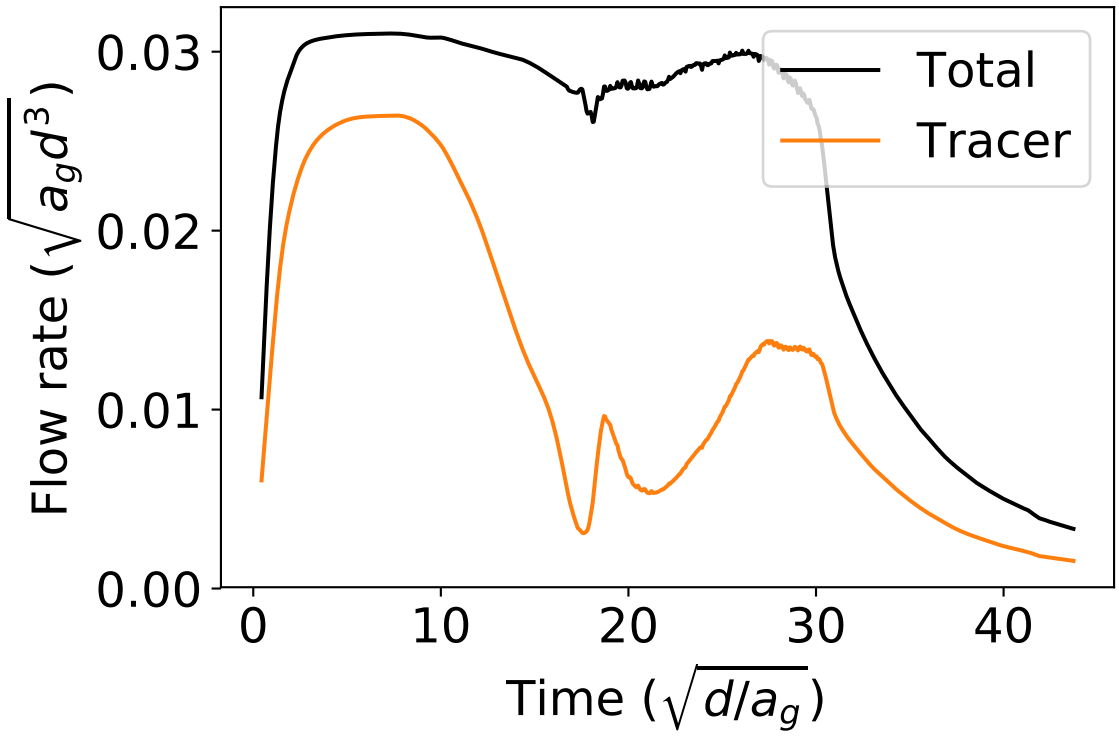

Figure 6.16: Flow rate for tracer and total material for a side-by-side split silo. This uses the same methodology as the cumulative distributions above, except with different initial tracer condition. The tracer indicates low friction material with $(\mu_s, \Delta\mu) = (0.47, 0.38)$, while the non-tracer material indicates high friction material with $(\mu_s, \Delta\mu) = (0.77, 0.58)$.

develops, the higher friction material 'leans' over the lower friction material as it drains faster than the higher friction material. This 'leaning' behaviour leads to some avalanching behaviour, causing layers of different types of material to form. As these layers approach the orifice the proportion of different types of materials change rapidly, resulting in variable flow rates. This can be seen in Figure 6.16 at $t \approx 20\sqrt{d/a_g}$, with the tracer flow demonstrating large swings in flow rate, and the overall material flow rate showing smaller fluctuations. This time period also demonstrates some instability in the total flow rate, possibly related to numerical instability causing 'gaps' in the material as can be seen in the $t = 15\sqrt{d/a_g}$ case of Figure 6.15 After these layers of material are expelled, the flow rates return to a more stable flow before slowing as the silo fully drains.

One interesting aspect of this flow is the small gap that can be seen in the $t = 15\sqrt{d/a_g}$ case of Figure 6.15 (also seen in Figure 6.5). Other simulations show 'splashes' of material at the

free surface of the material, such as in Figures 6.1 and 6.13. These sporadic discontinuities seem to occur at the bottom of the 'valley' made by the two sides of the free surface. The previous simulations have all been symmetric, meaning these events have occurred along the center line, however in Figure 6.15 the larger mass of high friction material 'pushes' the hole to the right of the orifice, as well as interacting with the folds of different components that is seen in this case. These interactions could be caused by fluctuations in the sideways forces at the free surface, resulting in sometimes material being 'squeezed' and creating a splash above the silo material, or being 'pulled' away and creating a gap which propagates down the silo. These effects have minor impact on the flow rate while the free surface is away from the orifice, however as the free surface nears the bottom of the silo these instabilities seem to create instability in the flow rate. The interface between components may also cause these effects, as seen in Figure 6.16 from $t \approx 20\sqrt{d/a_g}$. While these effects seem analogous to cascading material along a granular slope, the mechanisms between this granular model and discrete interactions in real granular materials are quite different, so caution should be taken when applying conclusions drawn from the instabilities seen in this model.

6.4 Conclusions

A synopsis of the topics covered in this chapter is provided in the following bullet points:

- Advective mixing in silos, including silos with multiple openings, were examined using the $\mu(I)$ model.
- Distance between openings was found to affect the mixing behaviour.
- A model for examining material with multiple separated components with different material properties was developed.
- Material with multiple unmixed components was found to act significantly differently from blended materials.

The advective mixing behaviour of granular material in various silo-like domains has been tested using the $\mu(I)$ model. Different domains can significantly change the dynamics of the

residence time within the silo.

Multiple openings with small separations have a very small effect on the mixing behaviour, while large separations have a much larger effect on mixing. Two different and potentially competing factors can determine to what extent a draining silo will mix: the larger area of material that is drawn by larger separations which 'delays' the start of tracer draining, and the blend of material at the orifice once tracer starts to drain. Large separation silos move towards the theoretical perfectly unmixed case due to the first effect, however these simulations also tend to have a smaller tracer fraction once the tracer begins to drain. The second factor could become much more relevant in case of multiple partial drains interspersed with partial loadings.

Material with two unmixed components, each with different material properties were also tested, showing significant differences in behaviour from the homogeneous case. This shows the importance of modelling different material properties in cases where multiple different materials may be loaded into a silo. Furthermore, in material that segregates this could be a significant factor and needs to be considered to accurately model granular segregation. To the author's knowledge, there is no other work using volume-of-fluid methods to examine interactions between multiple types of materials. This model could potentially be extended to vary the density, particle size, dilatation strength, nonlocal fluidity strength, or any other parameter of the components, creating a powerful model applicable to a wide variety of situations.

Chapter 7

Conclusion

Understanding granular flow is vital for many areas of research and industry, and as such many models have been developed to capture many of the various complexities of granular flow. Many of these models work well to describe particular phenomena in simple geometries, however these models can fail in more complex domains, miss other important phenomena, or become computationally infeasible when scaled to realistic sizes. This work has explored and extended the space of continuum models in silo and silo-like domains. The key achievements of this thesis are:

- Applying the $\mu(I)$ model to the two opening silo and replicating the 'flow rate dip'.
- Extending the $\mu(I)$ model to account for Hele-Shaw wall friction, dilatancy, and nonlocal fluidity in one model.
- Examining the mixing and quasi-static behaviour of single opening silos, multiple opening silos, and silos with inserts.
- Creating a model for materials with multiple components with different physical properties.

Combining all of these key achievements results in a powerful model widely applicable to a variety of complex domains, exhibiting many unique granular flow behaviours, and capable of handling combinations of different granular materials.

7.1 Summary of work

The $\mu(I)$ model is capable of capturing many aspects of granular flow in a pseudo-$2D$ silo. In Chapter 4 the radial model, kinematic model, stochastic model, and the $\mu(I)$ model were applied to the $2D$ silo. The $\mu(I)$ model, as a model capable of giving predictions for flow rate, was shown to predict flow rates fitting with the Beverloo-Hagen relation. Each of Hele-Shaw wall friction, nonlocal fluidity, and dilatancy extensions all significantly affected the base $\mu(I)$ flow rate in different ways.

Chapter 4 also shows that the model was capable of capturing realistic frictional behaviour in the presence of multiple openings, resulting in the 'flow rate dip phenomena' demonstrated in practical experiments [50]. The model is also extended to include front and back Hele-Shaw wall friction, nonlocal fluidity, and dilatancy. Each of Hele-Shaw wall friction, nonlocal fluidity, and dilatancy extensions were found to have a significant impact on the dynamics of the flow rate dip. This shows that a model incorporating all of these effects, such as the combination model developed in this work, is required to accurately capture the intricacies of a complex domain like the double slot silo.

In Chapter 5 the $\mu(I)$ model was also tested in more complex domains, i.e. silos with inserts. The model was capable of predicting flow rate behaviour for a variety of insert sizes and shapes. The portion of the silo with stationary or slow moving material was also examined. The flow rate was found to be highly dependant on insert size and position, while the static proportion was much less sensitive. As inserts are used in many industrial silos to avoid aging material, this model could have applications in industries seeking to optimise material age homogeneity without compromising flow characteristics of the silo.

Finally, the residence time of material within the silo was examined in Chapter 6. This was used to track mixing behaviour of layers of material in silos, finding the impact of multiple openings on the mixing in a draining silo.

Chapter 6 also extended the model to material with multiple components, each with different material properties. Many processes can intentionally or unintentionally lead to material that is separated by physical properties, and as such a model capable of extending our understanding

of these kinds of domains is vital for optimising many industrial processes. Silos were filled with material where the components were initially in distinct sections of the silo, and each component had different material parameters. This configuration was shown to make a relevant difference in mixing behaviour and will need to be accounted for when modelling processes which can lead to separated materials. This could involve industrial processes where different types of material are loaded into a silo at different times, but could also occur from an initially homogeneous material which undergoes segregation as it is processed.

7.2 Potential future work

- While the $\mu(I)$ model is a powerful model and has been shown to fit experimental work, regions of stability for this model have not been sufficiently studied. The base $\mu(I)$ model has been shown to be well-posed only for certain combinations of I, I_0, and $\Delta\mu$ [13]. The stability region can be extended with the incorporation of certain assumptions, such as certain forms of compressibility [14, 60]. However, it is unclear what the stability region is for the combined model used throughout this work. The author notes that instabilities occurred in a variety of different simulations, especially when testing extreme values of parameters suggesting that the model is not well-posed for all parameter values. Further work is required to rigorously determine the limits of this model.

- Boundary conditions are also a field of study in need of further attention. Some work has been done in the field [10], however it is unclear what the appropriate boundary conditions are for these simulations. The choice of non-slip boundary conditions has been used throughout this work, with the exception of Section 5.1 where a small non-zero nonlocal fluidity greatly improved stability in the presence of inserts. No clear choice for continuum boundary conditions is currently available, and at this stage the only way to choose an appropriate boundary condition is by comparison with experiment or DEM simulations. Further work could improve the selection of boundary conditions.

- Some of the insert shapes tested in Section 5.2.1 had flat bottoms. In a practical system this would lead to a void, where the interstitial fluid (i.e. air) would replace granular material

just below the insert. The formulation of the $\mu(I)$ model used here is not capable of modelling these voids as the interstitial fluid is blocked by the modelled granular material and the pressure is assumed to be positive. In this work the result is extremely rapid velocities at the lower corners of the insert. While the flow rate did not seem to be significantly affected by these disproportionate local velocities, future work examining these shapes should involve a model capable of capturing these voids.

- While materials with different components were tested in Section 6.2.2, these materials were initially unblended and remained relatively unblended throughout the simulations. In reality, materials with different components often occur in a blended state, and can become less blended through segregation [67]. This work shows that accounting for the individual material properties of different components of the material can have significant effects, however the model was not extended to account for the mechanics that actually cause the separation of components. This work laid the foundation for a more complete segregation model, where the segregated material acts differently than the blended material.

- The base $\mu(I)$ model is assumed to be incompressible, while granular materials are not truly incompressible. While the dilatancy model improves on this assumption, a compressible model could improve modelling of granular materials, particularly near low pressure high speed areas such as material near a silo orifice.

It is hoped that future modelling work will improve upon these gaps in knowledge, further pushing the boundaries of our collective understanding of dense granular flow.

Appendix A

Mohr-Coulomb stress

A Mohr circle describes the relationship between normal stress and shear stress for an element of granular material. Combined with the yield criterion $\tau \geq \mu\sigma$, this can be used to determine the force required to make the material yield, and the slip plane along which it will yield.

Consider a block of material, with a $2D$ example depicted in Figure A.1. The element experiences shear stresses τ_{ij} and normal stresses σ_{ii}. With the assumption that the element is not experiencing a net rotating force, then the shear stress is symmetric, i.e. $\tau_{ij} = \tau_{ji}$. Then the stress $\boldsymbol{\sigma}$ can be represented as a matrix

$$\boldsymbol{\sigma} = \begin{bmatrix} \sigma_{xx} & \tau_{xy} \\ \tau_{xy} & \sigma_{yy} \end{bmatrix} \tag{A.1}$$

for a $2D$ case, or

$$\boldsymbol{\sigma} = \begin{bmatrix} \sigma_{xx} & \tau_{xy} & \tau_{xz} \\ \tau_{xy} & \sigma_{yy} & \tau_{yz} \\ \tau_{xz} & \tau_{yz} & \sigma_{zz} \end{bmatrix} \tag{A.2}$$

for a $3D$ case.

Because $\boldsymbol{\sigma}$ is symmetric, it is possible to find a rotation matrix which diagonalizes $\boldsymbol{\sigma}$. This

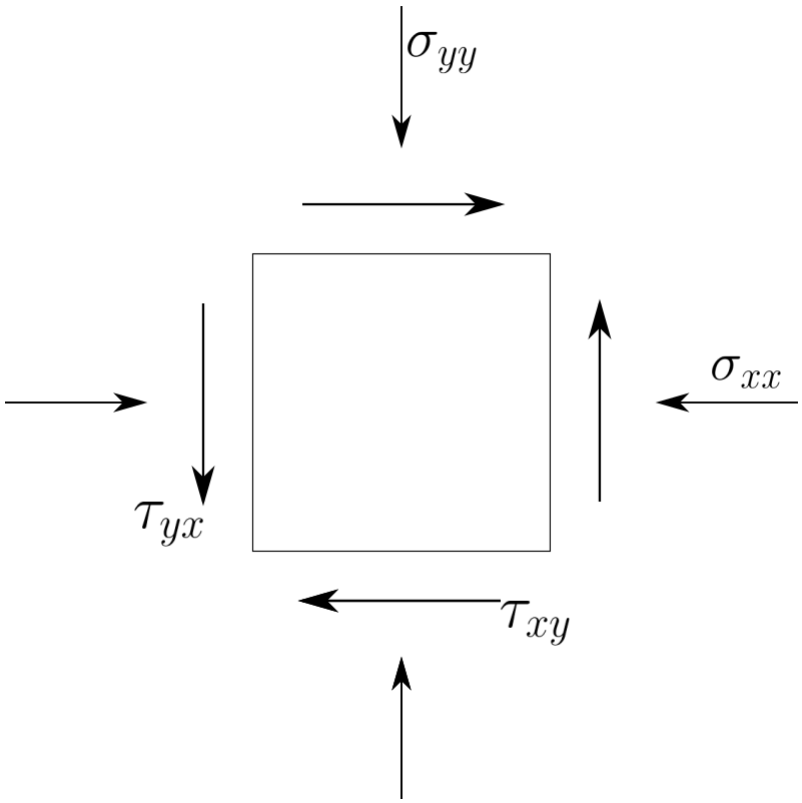

Figure A.1: An illustration of stresses in an arbitrary $2D$ element.

means that a basis exists for which the stresses are only normal stresses, i.e. for a $2D$ case

$$\hat{\boldsymbol{\sigma}} = \begin{bmatrix} \hat{\sigma}_{11} & 0 \\ 0 & \hat{\sigma}_{22} \end{bmatrix} \tag{A.3}$$

or for a $3D$ case

$$\hat{\boldsymbol{\sigma}} = \begin{bmatrix} \hat{\sigma}_{11} & 0 & 0 \\ 0 & \hat{\sigma}_{22} & 0 \\ 0 & 0 & \hat{\sigma}_{33} \end{bmatrix}. \tag{A.4}$$

This enables us to define the major stress σ_{maj} and minor stress σ_{min}, which are the largest and smallest normal stress, respectively, of the diagonalized stress matrix $\hat{\boldsymbol{\sigma}}$.

Given vectors in the direction of the major and minor stresses, a plane containing these two vectors can be defined, as depicted in Figure A.2. Then consider a potential slip line/plane in this plane at some angle θ. If the slip line is aligned with either the major or minor stress, i.e. $\theta = 0$ or $\theta = \pi/2$, then along the slip line there is no shear stress by definition. For angles not aligned with the major or minor stresses, there will be some non-zero shear stress τ with an accompanying normal stress σ. This is given by

$$\tau = \left(\frac{\sigma_{\text{maj}} - \sigma_{\text{min}}}{2}\right) \sin(2\theta), \tag{A.5}$$

$$\sigma = \left(\frac{\sigma_{\text{maj}} + \sigma_{\text{min}}}{2}\right) + \left(\frac{\sigma_{\text{maj}} - \sigma_{\text{min}}}{2}\right) \cos(2\theta). \tag{A.6}$$

The set of all possible values that τ and σ can take when plotted in the (τ, σ) space form a circle, as depicted in Figure A.3. This circle is called the Mohr circle, and represents the forces of possible slip planes. An intersection of any point on this circle with the yield criterion $\tau \geq \mu\sigma$ is a necessary and sufficient condition for the material to slip. The yield criterion in the (τ, σ) plane is represented by a line through the origin with slope μ (or $-\mu$), as represented by the dotted lines in Figure A.3. Then the critical point at which the transition between stationary material and yield can be calculated by considering the point at which the μ line lies tangent to

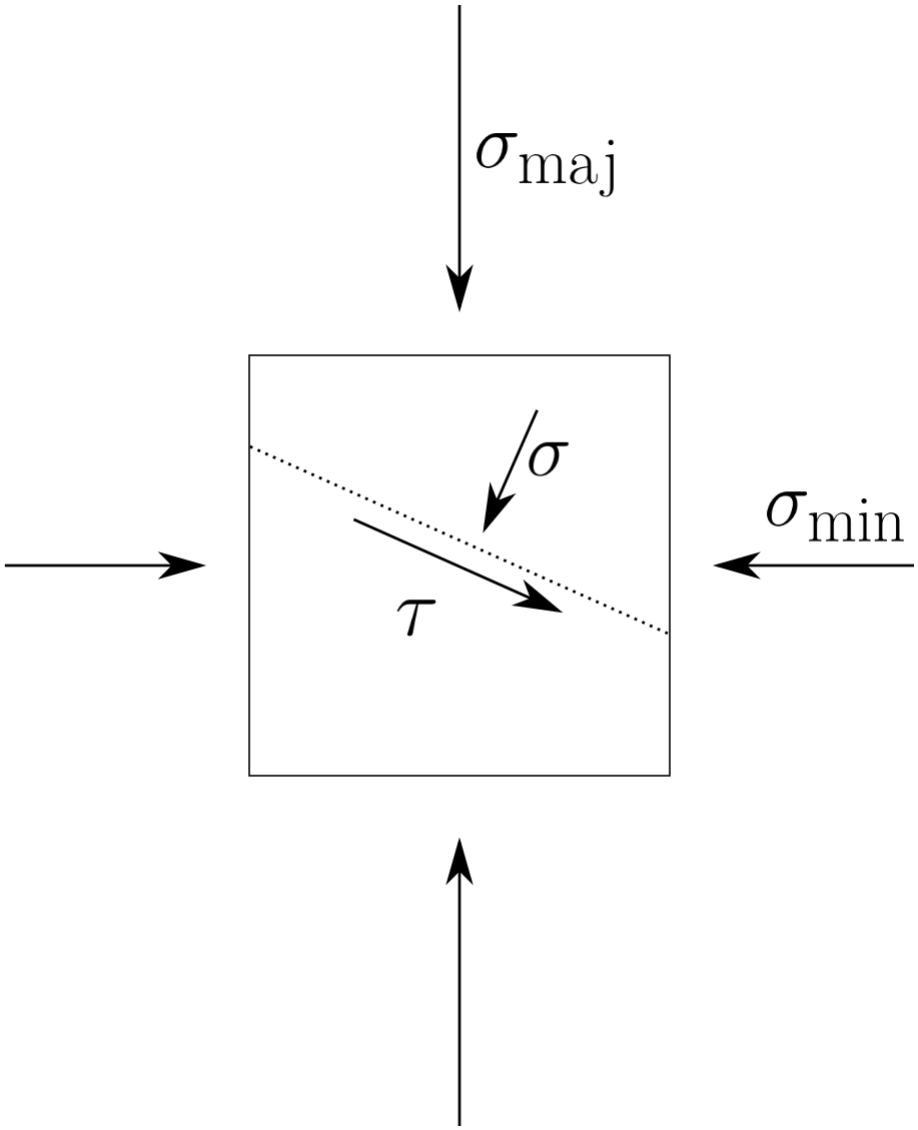

Figure A.2: An illustration of shear stress introduced by difference in major and minor stresses. In the directions of major and minor stresses there is no shear stress, however along angled planes a combination of normal and shear stress is induced which may cause static friction to be overcome.

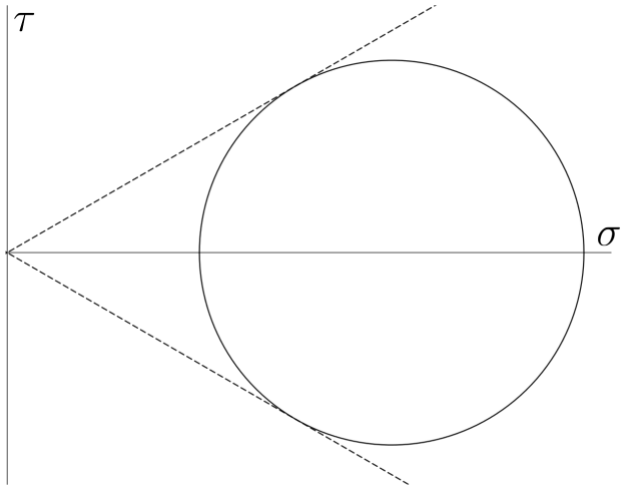

Figure A.3: The Mohr circle. The horizontal axis depicts the normal stress along a potential slip plane, while the vertical depicts the shear stress. All possible slip planes for a block of granular material fall on (or within) the Mohr circle. The yield criterion $\tau \geq \mu\sigma$ is given by the dotted line, and the material yields if and only if the Mohr circle intersects this line.

the Mohr circle. Given $\alpha = \arctan(\mu)$ and minor stress σ_{min}, the critical major stress σ_{maj} is

$$\sigma_{\text{maj}} = \left(\frac{1+\sin(\alpha)}{1-\sin(\alpha)}\right)\sigma_{\text{min}}. \tag{A.7}$$

Note that while the analysis is done in the plane of the major and minor stresses, it is also sufficient for other planes. This is because other planes will have equivalent (τ, σ) circles that are contained within the larger Mohr circle, and so if the yield criterion is met along another plane it will also be met in the plane of the major and minor stresses. As such, the yield analysis of $3D$ systems simplifies to the $2D$ case.

Appendix B

Navier-Stokes numerical method

Many of the simulations done in this work are numerical solutions to the Navier-Stokes equations, in particular the $\mu(I)$ model and its extensions. These simulations are done with the software Basilisk [143]. This Appendix describes some of the mathematics underlying Basilisk [111, 141, 142]. Note that Basilisk uses methods originally developed for Gerris, which was made by the same developers as Basilisk.

The Navier-Stokes equations with incompressible assumption are

$$\begin{aligned} &\frac{\partial \mathbf{u}}{\partial t} + \mathbf{u} \cdot \nabla \mathbf{u} = \frac{1}{\rho} \left[-\nabla P + \nabla \cdot (2\eta \mathbf{D}) \right] - \mathbf{a_g}, \\ &\nabla \cdot \mathbf{u} = 0, \end{aligned} \tag{B.1}$$

where $\mathbf{u}$ is the velocity vector, ρ is the density, $\mathbf{D}$ is the strain rate tensor given by $\mathbf{D} = [\nabla \mathbf{u} + (\nabla \mathbf{u})^T]/2$, and $\mathbf{a_g}$ is the acceleration due to gravity. In addition to the Navier-Stokes equations, a volume-of-fluid (VOF) method is used to track the interface between granular material and the interstitial fluid. Given a tracer c indicating the presence of granular material, the additional equations

$$\begin{aligned} &\frac{\partial \mathbf{c}}{\partial t} + \nabla \cdot (c\mathbf{u}) = 0, \\ &\rho = c\rho_1 + (1-c)\rho_2, \\ &\frac{1}{\eta} = \frac{c}{\eta_1} + \frac{1-c}{\eta_2}, \end{aligned} \tag{B.2}$$

are added, where subscripts 1 and 2 indicate properties of granular material and interstitial fluid respectively. The VOF method is also used to track advective tracers when these are implemented, such as in Chapter 6, by using additional tracers to track components of the material.

The discretization used by Basilisk is a staggered-in-time method, given by

$$\begin{aligned}
&\frac{c_{n+\frac{1}{2}} - c_{n-\frac{1}{2}}}{\Delta t} + \nabla \cdot (c_n \mathbf{u}_n) = 0, \\
&\rho_{n+\frac{1}{2}} \left(\frac{\mathbf{u}_{n+1} - \mathbf{u}_n}{\Delta t} + \mathbf{u}_{n+\frac{1}{2}} \cdot \nabla \mathbf{u}_{n+\frac{1}{2}} \right) = \nabla \cdot (\eta_{n+\frac{1}{2}} \mathbf{D}_{n+1}) - \nabla P_{n-\frac{1}{2}}, \\
&\mathbf{u}_{n+1} = \frac{\Delta t}{\rho_{n+\frac{1}{2}}} \left(\nabla P_{n+\frac{1}{2}} - \nabla P_{n-\frac{1}{2}} \right), \\
&\nabla \cdot \mathbf{u}_{n+\frac{1}{2}} = 0.
\end{aligned} \tag{B.3}$$

The advection term $\mathbf{u}_{n+\frac{1}{2}} \cdot \nabla \mathbf{u}_{n+\frac{1}{2}}$ can be approximated using the Bell-Collela-Glaz advection scheme [16]. The third equation can be rearranged to give an equation in the form of the Poisson equation:

$$\nabla \cdot \left(\frac{\Delta t}{\rho_{n+\frac{1}{2}}} \nabla P_{n+\frac{1}{2}} \right) = \nabla \cdot \left(\mathbf{u}_{n+1} + \frac{\Delta t}{\rho_{n+\frac{1}{2}}} \nabla P_{n-\frac{1}{2}} \right). \tag{B.4}$$

The momentum equation can also be simplified to a Helmholtz problem which gives decoupled scalar equations

$$\frac{\rho_{n+\frac{1}{2}}}{\Delta t} \mathbf{u}_{n+1} - \frac{1}{2} \nabla \cdot (\eta_{n+\frac{1}{2}} \nabla \mathbf{u}_{n+1}) = \rho_{n+\frac{1}{2}} \left(\frac{\mathbf{u}_n}{\Delta t} - \mathbf{u}_{n+\frac{1}{2}} \cdot \nabla \mathbf{u}_{n+\frac{1}{2}} \right) - \nabla P_{n-\frac{1}{2}} + \frac{1}{2} \nabla \mathbf{u}_n^T \nabla \eta_{n+\frac{1}{2}}. \tag{B.5}$$

This can be implemented into a solver based on Poisson solvers [142].

Appendix C

Basilisk code

Here an example Basilisk script is given for those seeking to reproduce some aspect of this work. This script is built upon an existing script, which can be found here: `http://basilisk.fr/sandbox/M1EMN/Exemples/granular_sandglass.c`

```
bool source_dilatancy, wall_friction, non_local;

#include "run.h"
#include "timestep.h"
#include "bcg.h"
#if EMBED
# include "viscosity-embed.h"
#else
# include "viscosity.h"
#endif

scalar rhov[], rhov_delay[];

mgstats project_alternate (struct Project q)
{
  face vector uf = q.uf;
  scalar p = q.p;
  (const) face vector alpha = q.alpha.x.i ? q.alpha : unityf;
  double dt = q.dt ? q.dt : 1.;
  int nrelax = q.nrelax ? q.nrelax : 4;

  scalar div[];
  foreach() {
    div[] = 0.;
    foreach_dimension()
      div[] += uf.x[1] - uf.x[];
    div[] /= dt*Delta;
    if (rhov[] > 0.) {
      foreach_dimension(){
        div[] -= (rhov[1,0] - rhov[])*uf.x[]/Delta/rhov[];
      }
```

```
      div[] -= (rhov[]-rhov_delay[])/dt/rhov[];
    }
  }
  rhov_delay = rhov;

  mgstats mgp = poisson (p, div, alpha,
            tolerance = TOLERANCE/sq(dt), nrelax = nrelax);

  foreach_face()
    uf.x[] -= dt*alpha.x[]*face_gradient_x (p, 0);
  boundary ((scalar *){uf});

  return mgp;
}

scalar p[];
vector u[], g[];
scalar pf[];
face vector uf[];

(const) face vector mu = zerof, a = zerof, alpha = unityf;
(const) scalar rho = unity;
mgstats mgp, mgpf, mgu;
bool stokes = false;

#if EMBED
# define neumann_pressure(i) (alpha.n[i] ? a.n[i]*fm.n[i]/alpha.n[i] :     \
                  a.n[i]*rho[]/(cm[] + SEPS))
#else
# define neumann_pressure(i) (a.n[i]*fm.n[i]/alpha.n[i])
#endif

p[right] = neumann (neumann_pressure(ghost));
p[left]  = neumann (- neumann_pressure(0));

#if AXI
uf.n[bottom] = 0.;
uf.t[bottom] = dirichlet(0); // since uf is multiplied by the metric which
                             // is zero on the axis of symmetry
p[top]    = neumann (neumann_pressure(ghost));
#else // !AXI
#  if dimension > 1
p[top]    = neumann (neumann_pressure(ghost));
p[bottom] = neumann (- neumann_pressure(0));
#  endif
#  if dimension > 2
p[front]  = neumann (neumann_pressure(ghost));
p[back]   = neumann (- neumann_pressure(0));
#  endif
#endif // !AXI

#if TREE && EMBED
void pressure_embed_gradient (Point point, scalar p, coord * g)
{
  foreach_dimension()
    g->x = rho[]/(cm[] + SEPS)*(a.x[] + a.x[1])/2.;
```

```
}
#endif // TREE && EMBED

event defaults (i = 0)
{

  CFL = 0.8;

  p.nodump = pf.nodump = true;

  if (alpha.x.i == unityf.x.i) {
    alpha = fm;
    rho = cm;
  }
  else if (!is_constant(alpha.x)) {
    face vector alphav = alpha;
    foreach_face()
      alphav.x[] = fm.x[];
    boundary ((scalar *){alpha});
  }

#if TREE
  uf.x.refine = refine_face_solenoidal;

#if EMBED
  uf.x.refine = refine_face;
  foreach_dimension()
    uf.x.prolongation = refine_embed_face_x;
  for (scalar s in {p, pf, u, g}) {
    s.restriction = restriction_embed_linear;
    s.refine = s.prolongation = refine_embed_linear;
  }
  for (scalar s in {p, pf})
    s.embed_gradient = pressure_embed_gradient;
#endif // EMBED
#endif // TREE
}

event default_display (i = 0)
  display ("squares (color = 'u.x', spread = -1);");

double dtmax;

event init (i = 0)
{
  boundary ((scalar *){u});
  trash ({uf});
  foreach_face()
    uf.x[] = fm.x[]*face_value (u.x, 0);
  boundary ((scalar *){uf});

  event ("properties");

  dtmax = DT;
  event ("stability");
}
```

```
event set_dtmax (i++,last) dtmax = DT;

event stability (i++,last) {
  dt = dtnext (stokes ? dtmax : timestep (uf, dtmax));
}

event vof (i++,last);
event tracer_advection (i++,last);
event tracer_diffusion (i++,last);

event properties (i++,last) {
  boundary ({alpha, mu, rho});
}

void prediction()
{
  vector du;
  foreach_dimension() {
    scalar s = new scalar;
    du.x = s;
  }

  if (u.x.gradient)
    foreach()
      foreach_dimension() {
#if EMBED
        if (!fs.x[] || !fs.x[1])
      du.x[] = 0.;
    else
#endif
      du.x[] = u.x.gradient (u.x[-1], u.x[], u.x[1])/Delta;
      }
  else
    foreach()
      foreach_dimension() {
#if EMBED
        if (!fs.x[] || !fs.x[1])
      du.x[] = 0.;
    else
#endif
      du.x[] = (u.x[1] - u.x[-1])/(2.*Delta);
    }
  boundary ((scalar *){du});

  trash ({uf});
  foreach_face() {
    double un = dt*(u.x[] + u.x[-1])/(2.*Delta), s = sign(un);
    int i = -(s + 1.)/2.;
    uf.x[] = u.x[i] + (g.x[] + g.x[-1])*dt/4. + s*(1. - s*un)*du.x[i]*Delta/2.;
    #if dimension > 1
    if (fm.y[i,0] && fm.y[i,1]) {
      double fyy = u.y[i] < 0. ? u.x[i,1] - u.x[i] : u.x[i] - u.x[i,-1];
      uf.x[] -= dt*u.y[i]*fyy/(2.*Delta);
    }
    #endif
```

```
    #if dimension > 2
    if (fm.z[i,0,0] && fm.z[i,0,1]) {
      double fzz = u.z[i] < 0. ? u.x[i,0,1] - u.x[i] : u.x[i] - u.x[i,0,-1];
      uf.x[] -= dt*u.z[i]*fzz/(2.*Delta);
    }
    #endif
    uf.x[] *= fm.x[];
  }
  boundary ((scalar *){uf});

  delete ((scalar *){du});
}

event advection_term (i++,last)
{
  if (!stokes) {
    prediction();
    //mgpf = project (uf, pf, alpha, dt/2., mgpf.nrelax);
    if (source_dilatancy) {
        mgpf = project_alternate (uf, pf, alpha, dt/2., mgpf.nrelax);
    } else {
        mgpf = project (uf, pf, alpha, dt/2., mgpf.nrelax);
    }
    advection ((scalar *){u}, uf, dt, (scalar *){g});
  }
}

static void correction (double dt)
{
  foreach()
    foreach_dimension()
      u.x[] += dt*g.x[];
  boundary ((scalar *){u});
}

event viscous_term (i++,last)
{
  if (constant(mu.x) != 0.) {
    correction (dt);
    mgu = viscosity (u, mu, rho, dt, mgu.nrelax);
    correction (-dt);
  }

  if (!is_constant(a.x)) {
    face vector af = a;
    trash ({af});
    foreach_face()
      af.x[] = 0.;
  }
}

event acceleration (i++,last)
{
  trash ({uf});
  foreach_face()
    uf.x[] = fm.x[]*(face_value (u.x, 0) + dt*a.x[]);
```

```
  boundary ((scalar *){uf, a});
}

void centered_gradient (scalar p, vector g) {
  face vector gf[];
  foreach_face()
    gf.x[] = fm.x[]*a.x[] - alpha.x[]*(p[] - p[-1])/Delta;
  boundary_flux ({gf});

  trash ({g});
  foreach()
    foreach_dimension()
      g.x[] = (gf.x[] + gf.x[1])/(fm.x[] + fm.x[1] + SEPS);
  boundary ((scalar *){g});
}

event projection (i++,last) {
  mgp = project (uf, p, alpha, dt, mgp.nrelax);
  centered_gradient (p, g);

  correction (dt);
}

event end_timestep (i++, last);

#if TREE
event adapt (i++,last) {
#if EMBED
  fractions_cleanup (cs, fs);
  foreach_face()
    if (uf.x[] && !fs.x[])
      uf.x[] = 0.;
  boundary ((scalar *){uf});
#endif
  event ("properties");
}
#endif



#include "vof.h"

#define RHOF 1e-3
#define mug  1e-4
#define rho(f) ((f) + RHOF*(1. - (f)))
#define rho_sd(f,I) (dilate(I)/phi_max*f + RHOF*(1. - (f)))
#define dilate(I) (max(phi_max-phi_gradient*I, phi_min))
#define LDOMAIN 5.
#define LEVEL 6 //Determines maximum resolution for the simulation

face vector alphav[], muv[];
scalar f[], eta[], I_array[], D2_array[], poi_lambda[], poi_b[], g_non_loc[], gran_flu[];
scalar * interfaces = {f};

double S,D=1./30,etamax=10000,mu_s=0.62,delta_mu=.48,I0=.6;
double non_local_strength = 0.5, phi_min=0.2,phi_max=0.6,phi_gradient = .2,muwall=0.4,WDOMAIN=2.;
```

```
double H0,R0,D,W,tmax,Q,Wmin,DW,V=1.;
char s[80];
FILE * fpf,*fwq,*ffr;

event init_granul (t = 0) {
    alpha = alphav;
    mu = muv;
    rho = rhov;
}

//convergence outputs
void mg_print (mgstats mg) {
    if (mg.i > 0 && mg.resa > 0.) {
        fprintf (stderr, "#   %d %g %g %g\n", mg.i, mg.resb, mg.resa, mg.resb > 0 ? exp (log (mg.resb/mg.resa)/mg.i) :
    }
}

event properties (i++) {
    trash ({alphav});
    scalar fa[];
    foreach() {
        fa[] = (4.*f[] +
            2.*(f[-1,0] + f[1,0] + f[0,-1] + f[0,1]) +
            f[1,1] + f[-1,1] + f[1,-1] + f[-1,-1])/16.;
    }
    boundary ({fa});

    if (non_local) {
        foreach() {
            eta[] = mug;
            poi_b[] = 0.;
            poi_lambda[] = 0.;
            if (p[] > 0.) {
                double D2 = 0.;
                foreach_dimension() {
                    double dxx = u.x[1,0] - u.x[-1,0];
                    double dxy = (u.x[0,1] - u.x[0,-1] + u.y[1,0] - u.y[-1,0])/2.;
                    D2 += sq(dxx) + sq(dxy);
                }
                D2_array[] = D2;

                if (D2 > pow(10,-30)) {//should be (D2 > 0.) but very small values also break the code?
                    D2 = sqrt(2.*D2)/(2.*Delta); // this D2 is sqrt(2) D2
                    double In = D2*D/sqrt(p[]);
                    I_array[] = In;
                    double muI = mu_s + delta_mu*In/(I0 + In);

                    double g_loc = D2/muI;
                    gran_flu[] = g_loc;
                    double xi = non_local_strength*D*sqrt((mu_s+delta_mu-muI)/(delta_mu*(muI-mu_s)));
                    poi_b[] = -g_loc/(xi*xi);
                    poi_lambda[] = -1./(xi*xi);
                }
            }
        }
```

```
        boundary({poi_lambda, poi_b, g_non_loc});
        mgstats mgnlp = poisson(g_non_loc, poi_b, lambda=poi_lambda);
            mg_print (mgnlp);
        foreach() {
            eta[] = min(max(p[]/g_non_loc[], sqrt(D*D*D)), etamax);
        }
    } else {
        foreach() {
            eta[] = mug;
            if (p[] > 0.) {
                double D2 = 0.;
                foreach_dimension() {
                    double dxx = u.x[1,0] - u.x[-1,0];
                    double dxy = (u.x[0,1] - u.x[0,-1] + u.y[1,0] - u.y[-1,0])/2.;
                    D2 += sq(dxx) + sq(dxy);
                }
                D2_array[] = D2;
                if (D2 > 0.) {
                    D2 = sqrt(2.*D2)/(2.*Delta); // this D2 is sqrt(2) D2
                    double In = D2*D/sqrt(p[]);
                    I_array[] = In;
                    double muI = mu_s + delta_mu*In/(I0 + In);
                    double etamin = sqrt(D*D*D);
                    eta[] = max(muI*p[]/D2, etamin);// this D2 is sqrt(2) D2
                    eta[] = min(eta[],etamax);
                }
            }
        }
    }

    boundary ({eta});

    foreach_face() {
        double fm = (fa[] + fa[-1,0])/2.;
        muv.x[] = (fm*(eta[] + eta[-1,0])/2. + (1. - fm)*mug);
        if (source_dilatancy) {
            alphav.x[] = 1./rho_sd(fm,I_array[]);
        } else {
            alphav.x[] = 1./rho(fm);
        }
    }

    foreach() {
        if (source_dilatancy) {
            rhov[] = rho_sd(fa[],I_array[]);
        } else {
            rhov[] = rho(fa[]);
        }
    }
    boundary ({muv,alphav,rhov});
}

event friction (i++) {
    if (wall_friction) {
        foreach() {
            double m = 2.*muwall*dt*p[]/WDOMAIN;
```

```
            double U = norm(u);
            foreach_dimension()
            u.x[]= U > 0 ? max(U-m,0)*u.x[]/U : 0 ;
        }
    }
}


//Boundary conditions
p[top] = dirichlet(0);
uf.n[top] = neumann(0);

u.t[bottom] =  (fabs(x-LDOMAIN/2-S/2)<= W/2 || fabs(x-LDOMAIN/2+S/2)<= W/2) ? neumann(0): dirichlet(0);
uf.n[bottom] =  (fabs(x-LDOMAIN/2-S/2)<= W/2 || fabs(x-LDOMAIN/2+S/2)<= W/2) ? neumann(0): dirichlet(0);
p[bottom]   =  (fabs(x-LDOMAIN/2-S/2)<= W/2 || fabs(x-LDOMAIN/2+S/2)<= W/2) ? dirichlet(0): neumann(0);

uf.n[right] = dirichlet(0);
u.t[right] = dirichlet(0);

uf.n[left] = dirichlet(0);
u.t[left] = dirichlet(0);
f[left]= neumann(0);

poi_lambda[right] = dirichlet(0);
poi_lambda[left] = dirichlet(0);
poi_lambda[bottom] = (fabs(x-LDOMAIN/2-S/2)<= W/2 || fabs(x-LDOMAIN/2+S/2)<= W/2) ? neumann(0): dirichlet(0);
poi_lambda[top] = neumann(0);

poi_b[right] = dirichlet(0);
poi_b[left] = dirichlet(0);
poi_b[bottom] = (fabs(x-LDOMAIN/2-S/2)<= W/2 || fabs(x-LDOMAIN/2+S/2)<= W/2) ? neumann(0): dirichlet(0);
poi_b[top] = neumann(0);

g_non_loc[right] = dirichlet(0);
g_non_loc[left] = dirichlet(0);
g_non_loc[bottom] = (fabs(x-LDOMAIN/2-S/2)<= W/2 || fabs(x-LDOMAIN/2+S/2)<= W/2) ? neumann(0): dirichlet(0);
g_non_loc[top] = neumann(0);


int main() {
    source_dilatancy = true; //enables dilatancy
    wall_friction = true; //enables wall friction
    non_local = true; //enables nonlocal fluidity
    L0 = LDOMAIN;
    N = 1 << LEVEL;
    DT = 0.01; // maximum timestep
    TOLERANCE = 1e-3;
    H0=4.5;
    R0=20.000;
    W = LDOMAIN/16.; //size of the openings
    DW = LDOMAIN/N;
    S = W + LDOMAIN/32.; //seperation between openings
    const face vector g[] = {0.,-1.};
    a = g;

    ffr = fopen ("flow.txt", "w");
```

```
    fclose (ffr);

    tmax = 4.;

    fwq = fopen ("outWQ", "a");
    fprintf(fwq,"\n");
    fclose (fwq);
    Q = 0;
    fpf = fopen ("interface.txt", "w");
    run();
    fclose (fpf);
    fwq = fopen ("outWQ", "a");
    fprintf(fwq,"%lf\n", Q);
    fclose (fwq);
}

event init (t = 0) {
    scalar phi[];
    //trash({I_array,u,uf,f,eta});
    foreach_vertex() {
        phi[] = min(H0 - y, R0 - x);
        I_array[] = 1;
    }
    fractions (phi, f);
    foreach() {
        p[] = (fabs(x-LDOMAIN/2)<= W && fabs(y)<= .1) ?  0 : max(H0 - y,0);
        u.x[] = (LDOMAIN/2-x)/100.;
        u.y[] = (fabs(x-LDOMAIN/2)<= 1.2*W && fabs(y)<= .1) ?  1. : 0;
        uf.x[] = (LDOMAIN/2-x)/100.;
        uf.y[] = (fabs(x-LDOMAIN/2)<= 1.2*W && fabs(y)<= .1) ?  1. : 0;
        g_non_loc[] = (fabs(x-LDOMAIN/2)<= 1.2*W && fabs(y)<= .1) ?  1./(y+.1) : 0 ;
    }
    boundary({g_non_loc});
    unrefine ((((fabs(x-LDOMAIN/2-S/2)<= W/2 || fabs(x-LDOMAIN/2+S/2)<= W/2) || (y>0.5)) && (level > 6));
    unrefine (((fabs(x-LDOMAIN/2-S/2)<= W/2 || fabs(x-LDOMAIN/2+S/2)<= W/2) && (level > 7)));
}

//convergence stats
event logfile (i++) {
    stats s = statsf (f);
    fprintf (stderr, "%g %d %g %g %g %g\n", t, i, dt, s.sum, s.min, s.max - 1.);
    mg_print (mgp);
    mg_print (mgpf);
    mg_print (mgu);
    fflush (stderr);
}

event interface ( t = 0; t += 1 ; t <= tmax && V>=.25) {
    output_facets (f, fpf);
    char s[80];
    sprintf (s, "field-%g.txt", t);
    FILE * fp = fopen (s, "w");
    scalar l[];
    foreach()
        l[] = level;
    output_field ({f,p,u,uf,pf,eta,I_array,D2_array,g_non_loc,gran_flu,l}, fp, linear = false);
```

```
    fclose (fp);
}

event debit (t += 0.05 ) {
    static double Vold,Qinst=0;
    Vold = V;
    V = 0;
    foreach()
        V = V + f[] * Delta * Delta * dilate(I_array[]);
    Qinst = -(V-Vold)/.05;
    if(Qinst > Q){
        Q = Qinst;
    }

    if(t>=.1) {
        ffr = fopen ("flow.txt", "a");
        fprintf(ffr,"%lf %lf %lf %lf\n",t,V/L0/H0,W,Qinst);
        fclose (ffr);
    }
    fflush (stdout);
}

event stop (t += 1) {
    if (t > 1. && V < .25*L0*H0) {
        return 1;
    }
}
```

Bibliography

[1] Anais Abramian, L Staron, and Pierre-Yves Lagree. The cohesive granular collapse as a continuum: Parametrization study. In *14th World Congress on Computational Mechanics (WCCM)*, volume 300. CIMNE, 2021.

[2] Khan Ahmad and IJ Smalley. Observation of particle segregation in vibrated granular systems. *Powder Technology*, 8(1-2):69–75, 1973.

[3] I Albert, JG Sample, AJ Morss, S Rajagopalan, A-L Barabási, and P Schiffer. Granular drag on a discrete object: Shape effects on jamming. *Physical review E*, 64(6):061303, 2001.

[4] TB Anderson and Roy Jackson. A fluid mechanical description of fluidized bed. *I&EC Fundamentals*, pages 6–4, 1967.

[5] Bruno Andreotti, Yoël Forterre, and Olivier Pouliquen. *Granular media: between fluid and solid*. Cambridge University Press, 2013.

[6] P Artega and U Tüzün. Flow of binary mixtures of equal-density granules in hoppers—size segregation, flowing density and discharge rates. *Chemical Engineering Science*, 45(1):205–223, 1990.

[7] Riccardo Artoni and Patrick Richard. Effective wall friction in wall-bounded 3d dense granular flows. *Physical Review Letters*, 115(15):158001, 2015.

[8] Riccardo Artoni, Andrea Santomaso, and Paolo Canu. Effective boundary conditions for dense granular flows. *Physical Review E*, 79(3):031304, 2009.

[9] Riccardo Artoni, Andrea Santomaso, and Paolo Canu. Coupling between countercurrent gas and solid flows in a moving granular bed: The role of shear bands at the walls. *International journal of multiphase flow*, 37(9):1209–1218, 2011.

[10] Riccardo Artoni, Andrea C Santomaso, Massimiliano Go, and Paolo Canu. Scaling laws for the slip velocity in dense granular flows. *Physical Review Letters*, 108(23):238002, 2012.

[11] Athanasios G Athanassiadis, Marc Z Miskin, Paul Kaplan, Nicholas Rodenberg, Seung Hwan Lee, Jason Merritt, Eric Brown, John Amend, Hod Lipson, and Heinrich M Jaeger. Particle shape effects on the stress response of granular packings. *Soft Matter*, 10(1):48–59, 2014.

[12] Sebastien Aumaître, Christof A Kruelle, and Ingo Rehberg. Segregation in granular matter under horizontal swirling excitation. *Physical Review E*, 64(4):041305, 2001.

[13] Thomas Barker, David G Schaeffer, Patricio Bohórquez, and JMNT Gray. Well-posed and ill-posed behaviour of the-rheology for granular flow. *Journal of Fluid Mechanics*, 779:794–818, 2015.

[14] Thomas Barker, DG Schaeffer, Michael Shearer, and JMNT Gray. Well-posed continuum equations for granular flow with compressibility and μ (I)-rheology. *Proceedings of the Royal Society A: Mathematical, Physical and Engineering Sciences*, 473(2201):20160846, 2017.

[15] G William Baxter, RP Behringer, Timothy Fagert, and G Allan Johnson. Pattern formation in flowing sand. *Physical Review Letters*, 62(24):2825, 1989.

[16] John B Bell, Phillip Colella, and Harland M Glaz. A second-order projection method for the incompressible navier-stokes equations. *Journal of computational physics*, 85(2):257–283, 1989.

[17] Diego Berzi, James T Jenkins, and Patrick Richard. Extended kinetic theory for granular flow over and within an inclined erodible bed. *Journal of Fluid Mechanics*, 885:A27, 2020.

[18] Wim A Beverloo, Hendrik Antonie Leniger, and J Van de Velde. The flow of granular solids through orifices. *Chemical Engineering Science*, 15(3-4):260–269, 1961.

[19] Daniel Bonn, Morton M Denn, Ludovic Berthier, Thibaut Divoux, and Sébastien Manneville. Yield stress materials in soft condensed matter. *Reviews of Modern Physics*, 89(3):035005, 2017.

[20] François Bouchut, Enrique D Fernández-Nieto, Anne Mangeney, Gladys Narbona-Reina, et al. Dilatancy in dry granular flows with a compressible μ(I) rheology. *Journal of Computational Physics*, 429:110013, 2021.

[21] Eric CP Breard, Luke Fullard, and Josef Dufek. The rheology of granular mixtures with varying size, density, particle friction and flow geometry. *arXiv preprint arXiv:2308.06062*, 2023.

[22] John Bridgwater. Mixing of powders and granular materials by mechanical means — a perspective. *Particuology*, 10(4):397–427, 2012.

[23] Stephen G Brush, CW Francis Everitt, and Elizabeth Garber. Maxwell on Saturn's rings. *Cambridge*, 1983.

[24] Justin C Burton, Jason M Amundson, Ryan Cassotto, Chin-Chang Kuo, and Michael Dennin. Quantifying flow and stress in ice mélange, the world's largest granular material. *Proceedings of the National Academy of Sciences*, 115(20):5105–5110, 2018.

[25] Charles S Campbell. Rapid granular flows. *Annual Review of Fluid Mechanics*, 22(1):57–90, 1990.

[26] Jian Chen, Mikito Furuichi, and Daisuke Nishiura. Discrete element simulation and validation of a mixing process of granular materials. *Materials*, 13(5):1208, 2020.

[27] Jaehyuk Choi, Arshad Kudrolli, and Martin Z Bazant. Velocity profile of granular flows inside silos and hoppers. *Journal of Physics: Condensed Matter*, 17(24):S2533, 2005.

[28] Jaehyuk Choi, Arshad Kudrolli, Rodolfo R Rosales, and Martin Z Bazant. Diffusion and mixing in gravity-driven dense granular flows. *Physical Review Letters*, 92(17):174301, 2004.

[29] KW Chu, B Wang, AB Yu, and A Vince. Modelling of multiphase flow in dense medium cyclones. *Powder Technology*, 193(3):235–247, 2009.

[30] Paul W Cleary and Mark L Sawley. DEM modelling of industrial granular flows: 3d case studies and the effect of particle shape on hopper discharge. *Applied Mathematical Modelling*, 26(2):89–111, 2002.

[31] PW Cleary. Discrete element modelling of industrial granular flow applications. *TASK. Quarterly-Scientific Bulletin*, 2:385–416, 1998.

[32] JAS Cleaver and RM Nedderman. Measurement of velocity profiles in conical hoppers. *Chemical Engineering Science*, 48(21):3703–3712, 1993.

[33] JAS Cleaver and RM Nedderman. Theoretical prediction of stress and velocity profiles in conical hoppers. *Chemical Engineering Science*, 48(21):3693–3702, 1993.

[34] A Cliff, LA Fullard, ECP Breard, J Dufek, and CE Davies. Granular size segregation in silos with and without inserts. *Proceedings of the Royal Society A*, 477(2245):20200242, 2021.

[35] P-P Cortet, Daniel Bonamy, François Daviaud, Olivier Dauchot, Bérengère Dubrulle, and Mathieu Renouf. Relevance of visco-plastic theory in a multi-directional inhomogeneous granular flow. *EPL (Europhysics Letters)*, 88(1):14001, 2009.

[36] Charles Augustin Coulomb. *Théorie des machines simples: en ayant égard au frottement de leurs parties, et à la roideur de cordages.* Bachelier, 1785.

[37] Peter A Cundall and Otto DL Strack. A discrete numerical model for granular assemblies. *Geotechnique*, 29(1):47–65, 1979.

[38] Frédéric Da Cruz, Sacha Emam, Michaël Prochnow, Jean-Noël Roux, and François Chevoir. Rheophysics of dense granular materials: Discrete simulation of plane shear flows. *Physical Review E*, 72(2):021309, 2005.

[39] Alberto Di Renzo and Francesco Paolo Di Maio. Comparison of contact-force models for the simulation of collisions in DEM-based granular flow codes. *Chemical Engineering Science*, 59(3):525–541, 2004.

[40] JA Drahun and J Bridgwater. The mechanisms of free surface segregation. *Powder Technology*, 36(1):39–53, 1983.

[41] Daniel Charles Drucker and William Prager. Soil mechanics and plastic analysis or limit design. *Quarterly of applied mathematics*, 10(2):157–165, 1952.

[42] Sachith Dunatunga and Ken Kamrin. Modelling silo clogging with non-local granular rheology. *Journal of Fluid Mechanics*, 940:A14, 2022.

[43] Jacques Duran. *Sands, powders, and grains: an introduction to the physics of granular materials*. Springer Science & Business Media, 2000.

[44] George CMA Ehrhardt, Andrew Stephenson, and Pedro M Reis. Segregation mechanisms in a numerical model of a binary granular mixture. *Physical Review E*, 71(4):041301, 2005.

[45] Abdoulaye Fall, Guillaume Ovarlez, David Hautemayou, Cédric Mézière, J-N Roux, and François Chevoir. Dry granular flows: Rheological measurements of the μ(I)-rheology. *Journal of rheology*, 59(4):1065–1080, 2015.

[46] Yi Fan, Youcef Boukerkour, Thibault Blanc, Paul B Umbanhowar, Julio M Ottino, and Richard M Lueptow. Stratification, segregation, and mixing of granular materials in quasi-two-dimensional bounded heaps. *Physical Review E*, 86(5):051305, 2012.

[47] Dorian Faroux, Kimiaki Washino, Takuya Tsuji, and Toshitsugu Tanaka. Coupling non-local rheology and volume of fluid (VOF) method: a finite volume method (FVM) implementation. In *EPJ Web of Conferences*, volume 249, page 03025. EDP Sciences, 2021.

[48] Kenneth E Fickie, Reza Mehrabi, and Roy Jackson. Density variations in a granular material flowing from a wedge-shaped hopper. *AIChE journal*, 35(5):853–855, 1989.

[49] H Scott Fogler and LF Brown. Distributions of residence times for chemical reactors. *Elements of chemical reaction engineering*, 4, 2006.

[50] LA Fullard, ECP Breard, CE Davies, AJR Godfrey, M Fukuoka, A Wade, J Dufek, and G Lube. The dynamics of granular flow from a silo with two symmetric openings. *Proceedings of the Royal Society A*, 475(2221):20180462, 2019.

[51] LA Fullard, CE Davies, G Lube, AC Neather, ECP Breard, and BJ Shepherd. The transient dynamics of dilation waves in granular phase transitions during silo discharge. *Granular Matter*, 19(1):6, 2017.

[52] LA Fullard, AJR Godfrey, MF Manaf, CE Davies, A Cliff, and M Fukuoka. Mixing experiments in 3d-printed silos; the role of wall friction and flow correcting inserts. *Advanced Powder Technology*, 31(5):1915–1923, 2020.

[53] Luke Fullard, Eric Breard, Clive Davies, Pierre-Yves Lagrée, Stéphane Popinet, and Gert Lube. Testing the μ(I) granular rheology against experimental silo data. In *EPJ Web of Conferences*, volume 140, page 11002. EDP Sciences, 2017.

[54] Luke Fullard and Clive Davies. Minimising the spread of residence-time distribution for flat and heaped powders in a wedge-shaped planar hopper. *Particuology*, 30:102–110, 2017.

[55] Luke A Fullard, Clive E Davies, and Graeme C Wake. Modelling powder mixing in mass flow discharge: a kinematic approach. *Advanced Powder Technology*, 24(2):499–506, 2013.

[56] Mikito Furuichi, Daisuke Nishiura, Osamu Kuwano, Arthur Bauville, Takane Hori, and Hide Sakaguchi. Arcuate stress state in accretionary prisms from real-scale numerical sandbox experiments. *Scientific reports*, 8(1):1–11, 2018.

[57] Adrien Gans, Olivier Pouliquen, and Maxime Nicolas. Cohesion-controlled granular material. *Physical Review E*, 101(3):032904, 2020.

[58] Angel Garcimartín, Iker Zuriguel, Luis A Pugnaloni, and Alvaro Janda. Shape of jamming arches in two-dimensional deposits of granular materials. *Physical review E*, 82(3):031306, 2010.

[59] D Gella, I Zuriguel, and D Maza. Decoupling geometrical and kinematic contributions to the silo clogging process. *Physical Review Letters*, 121(13):138001, 2018.

[60] Linda Gesenhues, José J Camata, Adriano MA Côrtes, Fernando A Rochinha, and Alvaro LGA Coutinho. Finite element simulation of complex dense granular flows using a well-posed regularization of the μ(I)-rheology. *Computers & Fluids*, 188:102–113, 2019.

[61] Dimitri Gidaspow. *Multiphase flow and fluidization: continuum and kinetic theory descriptions*. Academic press, 1994.

[62] Isaac Goldhirsch. Introduction to granular temperature. *Powder Technology*, 182(2):130–136, 2008.

[63] MJV Goldschmidt, JAM Kuipers, and Willibrordus Petrus Maria van Swaaij. Hydrodynamic modelling of dense gas-fluidised beds using the kinetic theory of granular flow: effect of coefficient of restitution on bed dynamics. *Chemical Engineering Science*, 56(2):571–578, 2001.

[64] Shahab Golshan, Reza Zarghami, Hamid Reza Norouzi, and Navid Mostoufi. Granular mixing in nauta blenders. *Powder Technology*, 305:279–288, 2017.

[65] C González-Montellano, F Ayuga, and JY Ooi. Discrete element modelling of grain flow in a planar silo: influence of simulation parameters. *Granular Matter*, 13:149–158, 2011.

[66] Julie Goyon, Annie Colin, G Ovarlez, A Ajdari, and L Bocquet. Spatial cooperativity in soft glassy flows. *Nature*, 454(7200):84, 2008.

[67] JMNT Gray. A hierarchy of particle-size segregation models: From polydisperse mixtures to depth-averaged theories. In *AIP Conference Proceedings*, volume 1542, pages 66–73. AIP, 2013.

[68] JMNT Gray and K Hutter. Pattern formation in granular avalanches. *Continuum Mechanics and Thermodynamics*, 9(6):341–345, 1997.

[69] GM Gutt and PK Haff. Boundary conditions on continuum theories of granular flow. *International journal of multiphase flow*, 17(5):621–634, 1991.

[70] PK Haff. Grain flow as a fluid-mechanical phenomenon. *Journal of Fluid Mechanics*, 134:401–430, 1983.

[71] GHL Hagen. Bericht über die zur Bekanntmachung geeigneten Verhandlungen der Königlich Preussischen Akademie der Wissenschaften zu Berlin, 1852.

[72] Thomas C Halsey and Alex J Levine. How sandcastles fall. *Physical Review Letters*, 80(14):3141, 1998.

[73] David L Henann and Ken Kamrin. A predictive, size-dependent continuum model for dense granular flows. *Proceedings of the National Academy of Sciences*, 110(17):6730–6735, 2013.

[74] Heinrich Rudolf Hertz. *Über die Berührung fester elastischer Körper und über die Härte*. Universitätsbibliothek Johann Christian Senckenberg, 2006.

[75] Joris Heyman, R Delannay, H Tabuteau, and A Valance. Compressibility regularizes the μ(I)-rheology for dense granular flows. *Journal of Fluid Mechanics*, 830:553–568, 2017.

[76] Raúl Cruz Hidalgo, Christian U Grosse, Ferenc Kun, Hans W Reinhardt, and Hans J Herrmann. Evolution of percolating force chains in compressed granular media. *Physical Review Letters*, 89(20):205501, 2002.

[77] Kimberly M Hill, Arvind Caprihan, and James Kakalios. Bulk segregation in rotated granular material measured by magnetic resonance imaging. *Physical Review Letters*, 78(1):50, 1997.

[78] DJ Hornbaker, Réka Albert, István Albert, A-L Barabási, and Peter Schiffer. What keeps sandcastles standing? *Nature*, 387(6635):765–765, 1997.

[79] Lu Huilin, Dimitri Gidaspow, Jacques Bouillard, and Liu Wentie. Hydrodynamic simulation of gas–solid flow in a riser using kinetic theory of granular flow. *Chemical Engineering Journal*, 95(1-3):1–13, 2003.

[80] Lu Huilin, He Yurong, and Dimitri Gidaspow. Hydrodynamic modelling of binary mixture in a gas bubbling fluidized bed using the kinetic theory of granular flow. *Chemical Engineering Science*, 58(7):1197–1205, 2003.

[81] Ryan C Hurley and José E Andrade. Friction in inertial granular flows: competition between dilation and grain-scale dissipation rates. *Granular Matter*, 17(3):287–295, 2015.

[82] Ivan Iordanoff and MM Khonsari. Granular lubrication: toward an understanding of the transition between kinetic and quasi-fluid regime. *J. Trib.*, 126(1):137–145, 2004.

[83] Fridtjov Irgens. *Rheology and non-Newtonian fluids*, volume 190. Springer, 2014.

[84] Kingsley Lawrence Iroba, Jochen Mellmann, Fabian Weigler, Thomas Metzger, and Evangelos Tsotsas. Particle velocity profiles and residence time distribution in mixed-flow grain dryers. *Granular Matter*, 13:159–168, 2011.

[85] Samuel Irvine, Luke Fullard, and Clive Davies. The effect of heaped and sloped powder layers on ejection times and the residence-time distribution of a conical mass-flow hopper. In *Applications+ Practical Conceptualization+ Mathematics= fruitful Innovation*, pages 175–189. Springer, 2016.

[86] Samuel K Irvine, Luke A Fullard, Daniel J Holland, Daniel A Clarke, Thomasin A Lynch, and Pierre-Yves Lagrée. Capturing the dynamics of a two orifice silo with the μ(I) model and extensions. *Advanced Powder Technology*, 34(7):104044, 2023.

[87] Samuel K Irvine, Luke A Fullard, Daniel J Holland, Daniel A Clarke, Thomasin A Lynch, and Pierre-Yves Lagrée. The $\mu(I)$ model and extensions applied to granular material in silo with inserts. *arXiv preprint arXiv:2302.12550*, 2023.

[88] Lucio Isa, Rut Besseling, and Wilson CK Poon. Shear zones and wall slip in the capillary flow of concentrated colloidal suspensions. *Physical Review Letters*, 98(19):198305, 2007.

[89] HA Janssen. Versuche uber Getreidedruck in Silozellen. *Z. Ver. Dtsch. Ing.*, 39(35):1045–1049, 1895.

[90] AW Jenike. A theory of flow of particulate solids in converging and diverging channels based on a conical yield function. *Powder technology*, 50(3):229–236, 1987.

[91] JT Jenkins and MW Richman. Boundary conditions for plane flows of smooth, nearly elastic, circular disks. *Journal of Fluid Mechanics*, 171:53–69, 1986.

[92] Richard P Jensen, Peter J Bosscher, Michael E Plesha, and Tuncer B Edil. DEM simulation of granular media—structure interface: effects of surface roughness and particle shape. *International Journal for Numerical and Analytical Methods in Geomechanics*, 23(6):531–547, 1999.

[93] Gordon R Johnson and William H Cook. Fracture characteristics of three metals subjected to various strains, strain rates, temperatures and pressures. *Engineering fracture mechanics*, 21(1):31–48, 1985.

[94] Kenneth Langstreth Johnson. *Contact mechanics*. Cambridge University Press, 1987.

[95] Pierre Jop, Yoël Forterre, and Olivier Pouliquen. Crucial role of sidewalls in granular surface flows: consequences for the rheology. *Journal of Fluid Mechanics*, 541:167–192, 2005.

[96] Pierre Jop, Yoël Forterre, and Olivier Pouliquen. A constitutive law for dense granular flows. *Nature*, 441(7094):727, 2006.

[97] Sandesh Kamath, Amit Kunte, Pankaj Doshi, and Ashish V Orpe. Flow of granular matter in a silo with multiple exit orifices: jamming to mixing. *Physical Review E*, 90(6):062206, 2014.

[98] Ken Kamrin. A hierarchy of granular continuum models: Why flowing grains are both simple and complex. In *EPJ Web of Conferences*, volume 140, page 01007. EDP Sciences, 2017.

[99] Ken Kamrin and Martin Z Bazant. Stochastic flow rule for granular materials. *Physical Review E*, 75(4):041301, 2007.

[100] Ken Kamrin and David L Henann. Nonlocal modeling of granular flows down inclines. *Soft matter*, 11(1):179–185, 2015.

[101] Ken Kamrin and Georg Koval. Nonlocal constitutive relation for steady granular flow. *Physical Review Letters*, 108(17):178301, 2012.

[102] Kenneth Norman Kamrin. *Stochastic and deterministic models for dense granular flow.* PhD thesis, Massachusetts Institute of Technology, 2008.

[103] William R Ketterhagen, Jennifer S Curtis, Carl R Wassgren, and Bruno C Hancock. Modeling granular segregation in flow from quasi-three-dimensional, wedge-shaped hoppers. *Powder Technology*, 179(3):126–143, 2008.

[104] William R Ketterhagen, Jennifer S Curtis, Carl R Wassgren, and Bruno C Hancock. Predicting the flow mode from hoppers using the discrete element method. *Powder technology*, 195(1):1–10, 2009.

[105] William R Ketterhagen, Jennifer S Curtis, Carl R Wassgren, Angela Kong, Padma J Narayan, and Bruno C Hancock. Granular segregation in discharging cylindrical hoppers: a discrete element and experimental study. *Chemical Engineering Science*, 62(22):6423–6439, 2007.

[106] Hassan Abbas Khawaja, Stuart A Scott, Muhammad Shakeel Virk, and Mojtaba Moatamedi. Quantitative analysis of accuracy of voidage computations in CFD-DEM simulations. *The Journal of Computational Multiphase Flows*, 4(2):183–192, 2012.

[107] James B Knight, Heinrich M Jaeger, and Sidney R Nagel. Vibration-induced size separation in granular media: The convection connection. *Physical Review Letters*, 70(24):3728, 1993.

[108] V Kumaran. Dense granular flow down an inclined plane: from kinetic theory to granular dynamics. *Journal of Fluid Mechanics*, 599:121–168, 2008.

[109] Amit Kunte, Pankaj Doshi, and Ashish V Orpe. Spontaneous jamming and unjamming in a hopper with multiple exit orifices. *Physical Review E*, 90(2):020201, 2014.

[110] Joseph F Labuz and Arno Zang. Mohr-Coulomb failure criterion. *Rock mechanics and rock engineering*, 45:975–979, 2012.

[111] P-Y Lagrée, L Staron, and S Popinet. The granular column collapse as a continuum: validity of a two-dimensional Navier-Stokes model with a μ(I)-rheology. *Journal of Fluid Mechanics*, 686:378–408, 2011.

[112] Samira Laidaoui, Pascale Aussillous, Mohammed Djermane, and Blanche Dalloz-Dubrujeaud. Discharge flow of granular media from rectangular silos: role of an obstacle and modelling by an orifice at the corner. *Mechanics & Industry*, 21(5):516, 2020.

[113] Thierry Le Pennec, Knut Jørgen Måløy, Eirik G Flekkøy, Jean Claude Messager, and Madani Ammi. Silo hiccups: Dynamic effects of dilatancy in granular flow. *Physics of Fluids*, 10(12):3072–3079, 1998.

[114] Daren Liu and David L Henann. Size-dependence of the flow threshold in dense granular materials. *Soft matter*, 14(25):5294–5305, 2018.

[115] Yujia Liu, Jeremy Marquardt, Sifan Peng, Liang Ge, Nan Gui, XT Yang, JY Tu, SY Jiang, and Seungjin Kim. Neural network prediction of residence time distribution for quasi-2d pebble flow. *Chemical Engineering Science*, 250:117363, 2022.

[116] JM López-Herrera, AM Gañán-Calvo, S Popinet, and MA Herrada. Electrokinetic effects in the breakup of electrified jets: A volume-of-fluid numerical study. *International Journal of Multiphase Flow*, 71:14–22, 2015.

[117] Cli KK Lun, Stuart B Savage, DJ Jeffrey, and Nicholas Chepurniy. Kinetic theories for granular flow: inelastic particles in couette flow and slightly inelastic particles in a general flowfield. *Journal of fluid mechanics*, 140:223–256, 1984.

[118] C Mankoc, A Janda, Roberto Arevalo, JM Pastor, Iker Zuriguel, A Garcimartín, and

Diego Maza. The flow rate of granular materials through an orifice. *Granular Matter*, 9(6):407–414, 2007.

[119] D Matuszek and M Tukiendorf. Application of roof shaped and double cone inserts in mixing of granular elements in the flow process. *International Agrophysics*, 22(1):147–150, 2008.

[120] Dominika Matuszek. Modelling selected parameters of granular elements in the mixing process. *International Agrophysics*, 29(1), 2015.

[121] Joseph J McCarthy, Devang V Khakhar, and Julio M Ottino. Computational studies of granular mixing. *Powder Technology*, 109(1-3):72–82, 2000.

[122] Steven W Meier, Richard M Lueptow, and Julio M Ottino. A dynamical systems approach to mixing and segregation of granular materials in tumblers. *Advances in Physics*, 56(5):757–827, 2007.

[123] F Melo, F Vivanco, C Fuentes, and V Apablaza. On drawbody shapes: from bergmark–roos to kinematic models. *International Journal of Rock Mechanics and Mining Sciences*, 44(1):77–86, 2007.

[124] F Melo, F Vivanco, C Fuentes, and V Apablaza. Kinematic model for quasi static granular displacements in block caving: Dilatancy effects on drawbody shapes. *International Journal of Rock Mechanics and Mining Sciences*, 45(2):248–259, 2008.

[125] GDR MiDi. On dense granular flows. *The European Physical Journal E*, 14(4):341–365, 2004.

[126] Noriko K Mitani, Hans-Georg Matuttis, and Toshihiko Kadono. Density and size segregation in deposits of pyroclastic flow. *Geophysical research letters*, 31(15), 2004.

[127] SBM Moreea and RM Nedderman. Exact stress and velocity distributions in a cohesionless material discharging from a conical hopper. *Chemical Engineering Science*, 51(16):3931–3942, 1996.

[128] Christoph R Müller, Daniel J Holland, Andrew J Sederman, Stuart A Scott, John S Dennis, and Lynn F Gladden. Granular temperature: comparison of magnetic resonance measurements with discrete element model simulations. *Powder Technology*, 184(2):241–253, 2008.

[129] WW Mullins. Stochastic theory of particle flow under gravity. *Journal of Applied Physics*, 43(2):665–678, 1972.

[130] Fernando J Muzzio, Troy Shinbrot, and Benjamin J Glasser. Powder technology in the pharmaceutical industry: the need to catch up fast, 2002.

[131] Humair Nadeem and Theodore J Heindel. Review of noninvasive methods to characterize granular mixing. *Powder Technology*, 332:331–350, 2018.

[132] RM Nedderman and U Tüzün. A kinematic model for the flow of granular materials. *Powder Technology*, 22(2):243–253, 1979.

[133] Ronald Midgley Nedderman. *Statics and kinematics of granular materials*, volume 352. Cambridge University Press Cambridge, 1992.

[134] Charles S Nickerson and Julia A Kornfield. A "cleat" geometry for suppressing wall slip. *Journal of Rheology*, 49(4):865–874, 2005.

[135] Vitaliy Ogarko and Stefan Luding. A fast multilevel algorithm for contact detection of arbitrarily polydisperse objects. *Computer physics communications*, 183(4):931–936, 2012.

[136] Julio M Ottino and DV Khakhar. Mixing and segregation of granular materials. *Annual review of fluid mechanics*, 32(1):55–91, 2000.

[137] Mickael Pailha and Olivier Pouliquen. A two-phase flow description of the initiation of underwater granular avalanches. *Journal of Fluid Mechanics*, 633:115–135, 2009.

[138] AA Pena, R Garcia-Rojo, and Hans Jürgen Herrmann. Influence of particle shape on sheared dense granular media. *Granular Matter*, 9(3-4):279–291, 2007.

[139] Gongwen Peng and Hans J Herrmann. Density waves of granular flow in a pipe using lattice-gas automata. *Physical Review E*, 49(3):R1796, 1994.

[140] JF Peters, M Muthuswamy, J Wibowo, and A Tordesillas. Characterization of force chains in granular material. *Physical review E*, 72(4):041307, 2005.

[141] Stéphane Popinet. Gerris: a tree-based adaptive solver for the incompressible Euler equations in complex geometries. *Journal of Computational Physics*, 190(2):572–600, 2003.

[142] Stéphane Popinet. An accurate adaptive solver for surface-tension-driven interfacial flows. *Journal of Computational Physics*, 228(16):5838–5866, 2009.

[143] Stéphane Popinet and collaborators. Basilisk. `http://basilisk.fr`, 2015.

[144] Olivier Pouliquen. Scaling laws in granular flows down rough inclined planes. *Physics of fluids*, 11(3):542–548, 1999.

[145] Olivier Pouliquen and Yoel Forterre. A non-local rheology for dense granular flows. *Philosophical Transactions of the Royal Society A: Mathematical, Physical and Engineering Sciences*, 367(1909):5091–5107, 2009.

[146] Farhang Radjai, Jean-Noël Roux, and Ali Daouadji. Modeling granular materials: century-long research across scales. *Journal of engineering mechanics*, 143(4):04017002, 2017.

[147] Pedro M Reis, G Ehrhardt, A Stephenson, and T Mullin. Gases, liquids and crystals in granular segregation. *EPL (Europhysics Letters)*, 66(3):357, 2004.

[148] Osborne Reynolds. LVII. On the dilatancy of media composed of rigid particles in contact. With experimental illustrations. *The London, Edinburgh, and Dublin Philosophical Magazine and Journal of Science*, 20(127):469–481, 1885.

[149] Patrick Richard, Mario Nicodemi, Renaud Delannay, Philippe Ribiere, and Daniel Bideau. Slow relaxation and compaction of granular systems. *Nature materials*, 4(2):121, 2005.

[150] Vincent Richefeu, Moulay Saïd El Youssoufi, and Farhang Radjai. Shear strength properties of wet granular materials. *Physical Review E*, 73(5):051304, 2006.

[151] James Robinson, Daniel Holland, and Luke Fullard. Evidence of a non-local ø (I) response. In *EPJ Web of Conferences*, volume 249, page 03028. EDP Sciences, 2021.

[152] Chris H Rycroft, Gary S Grest, James W Landry, and Martin Z Bazant. Analysis of granular flow in a pebble-bed nuclear reactor. *Physical review E*, 74(2):021306, 2006.

[153] Guilherme Salvador-Vieira, Lydie Staron, Stéphane Popinet, Stéphanie Deboeuf, and Pierre-Yves Lagrée. Modeling flow arrest using a non-local rheology? In *EPJ Web of Conferences*, volume 140, page 03045. EDP Sciences, 2017.

[154] Azadeh Samadani, A Pradhan, and A Kudrolli. Size segregation of granular matter in silo discharges. *Physical Review E*, 60(6):7203, 1999.

[155] Stuart B Savage. The mechanics of rapid granular flows. *Advances in Applied Mechanics*, 24:289–366, 1984.

[156] Jennifer Saxton, Philip Fralick, Umed Panu, and Keith Wallace. Density segregation of minerals during high-velocity transport over a rough bed: implications for the formation of placers. *Economic Geology*, 103(8):1657–1664, 2008.

[157] Michael Schirber. Self-spinning grains prove granular theory. *Physics*, 10:54, 2017.

[158] DA Serrano, G Ruiz-Chavarría, M Pliego, CA Vargas, and A Medina. On the validity of the Hagen and Beverloo formulas for grains discharge through thin sidewalls of bins. *Revista Mexicana de física*, 65(2):139–147, 2019.

[159] Irena Sielamowicz and Michał Czech. Analysis of the radial flow assumption in a converging model silo. *Biosystems engineering*, 106(4):412–422, 2010.

[160] Leonardo E Silbert, Deniz Ertaş, Gary S Grest, Thomas C Halsey, Dov Levine, and Steven J Plimpton. Granular flow down an inclined plane: Bagnold scaling and rheology. *Physical Review E*, 64(5):051302, 2001.

[161] Cezary Slominski, Maciej Niedostatkiewicz, and Jacek Tejchman. Application of particle image velocimetry (piv) for deformation measurement during granular silo flow. *Powder Technology*, 173(1):1–18, 2007.

[162] Matthias Sperl. Experiments on corn pressure in silo cells–translation and comment of janssen's paper from 1895. *Granular Matter*, 8(2):59–65, 2006.

[163] L Staron, P-Y Lagrée, and S Popinet. Continuum simulation of the discharge of the granular silo. *The European Physical Journal E*, 37(1):5, 2014.

[164] Lydie Staron, Anais Abramian, and Pierre-Yves Lagrée. Capturing the failure of a cohesive granular step. In *EPJ Web of Conferences*, volume 249, page 08006. EDP Sciences, 2021.

[165] Lydie Staron, P-Y Lagrée, and Stéphane Popinet. The granular silo as a continuum plastic flow: The hour-glass vs the clepsydra. *Physics of Fluids*, 24(10):103301, 2012.

[166] Zhu Tang, Theodore A Brzinski, Michael Shearer, and Karen E Daniels. Nonlocal rheology of dense granular flow in annular shear experiments. *Soft matter*, 14(16):3040–3048, 2018.

[167] Patricia A Thomas and Jonathan D Bray. Capturing nonspherical shape of granular media with disk clusters. *Journal of Geotechnical and Geoenvironmental Engineering*, 125(3):169–178, 1999.

[168] Anthony Richard Thornton, Dinant Krijgsman, Ate te Voortwis, Vitaliy Ogarko, Stefan Luding, Rudi Fransen, Sebastian Gonzalez, Onno Bokhove, Olukayode Imole, and Thomas Weinhart. A review of recent work on the discrete particle method at the university of twente: An introduction to the open-source package mercurydpm. *Discrete Element Methods*, 6, 2013.

[169] U Tüzün and RM Nedderman. Gravity flow of granular materials round obstacles—i: Investigation of the effects of inserts on flow patterns inside a silo. *Chemical Engineering Science*, 40(3):325–336, 1985.

[170] J Antoon Van Hooft, Stéphane Popinet, Chiel C Van Heerwaarden, Steven JA Van der Linden, Stephan R de Roode, and Bas JH Van de Wiel. Towards adaptive grids for atmospheric boundary-layer simulations. *Boundary-layer meteorology*, 167(3):421–443, 2018.

[171] Loic Vanel, Daniel Howell, D Clark, RP Behringer, and Eric Clément. Memories in sand:

Experimental tests of construction history on stress distributions under sandpiles. *Physical Review E*, 60(5):R5040, 1999.

[172] Bernhard Vowinckel, Edward Biegert, Eckart Meiburg, Pascale Aussillous, and Élisabeth Guazzelli. Rheology of mobile sediment beds sheared by viscous, pressure-driven flows. *Journal of Fluid Mechanics*, 921:A20, 2021.

[173] Xuewen Wang, Zhaojian Yang, Xuefeng Shu, and Jiling Feng. The static contact statuses between granular materials and flat-bottomed steel silos. *Powder technology*, 235:1053–1059, 2013.

[174] Thomas Ward and William Hourigan. Granular segregation in a tilted-rotating drum. *Powder technology*, 215:227–234, 2012.

[175] NS Weerasekara, MS Powell, PW Cleary, Luís Marcelo Tavares, M Evertsson, RD Morrison, Johannes Quist, and RM Carvalho. The contribution of DEM to the science of comminution. *Powder Technology*, 248:3–24, 2013.

[176] Thomas Weinhart, Remco Hartkamp, Anthony R Thornton, and Stefan Luding. Coarse-grained local and objective continuum description of three-dimensional granular flows down an inclined surface. *Physics of fluids*, 25(7), 2013.

[177] Thomas Weinhart, Carlos Labra, Stefan Luding, and Jin Y Ooi. Influence of coarse-graining parameters on the analysis of DEM simulations of silo flow. *Powder technology*, 293:138–148, 2016.

[178] J. C Williams. The mixing of dry powders. *Powder Technology*, 2(1):13–20, 1968.

[179] Hongyi Xiao, Paul B Umbanhowar, Julio M Ottino, and Richard M Lueptow. Modelling density segregation in flowing bidisperse granular materials. *Proceedings of the Royal Society A: Mathematical, Physical and Engineering Sciences*, 472(2191):20150856, 2016.

[180] Cheng Xu, Fei-Liang Wang, Li-Peng Wang, Xiao-Shuang Qi, Qing-Fan Shi, Liang-Sheng Li, and Ning Zheng. Inter-orifice distance dependence of flow rate in a quasi-two-dimensional hopper with dual outlets. *Powder technology*, 328:7–12, 2018.

[181] Xuezhi Zhang, Sheng Zhang, Guanghui Yang, Ping Lin, Yuan Tian, Jiang-Feng Wan, and Lei Yang. Investigation of flow rate in a quasi-2d hopper with two symmetric outlets. *Physics Letters A*, 380(13):1301–1305, 2016.

[182] Y Zhou, P-Y Lagrée, S Popinet, P Ruyer, and Pascale Aussillous. Experiments on, and discrete and continuum simulations of, the discharge of granular media from silos with a lateral orifice. *Journal of Fluid Mechanics*, 829:459–485, 2017.

[183] Yixian Zhou. *Ejection de gaz et de grains suite à la rupture d'un crayon de combustible nucléaire: modélisation de la dynamique*. PhD thesis, Aix-Marseille, 2016.

[184] HP Zhu, AB Yu, and YH Wu. Numerical investigation of steady and unsteady state hopper flows. *Powder Technology*, 170(3):125–134, 2006.

[185] Z Zou, Pierre Ruyer, P-Y Lagrée, and Pascale Aussillous. Discharge of a silo through a lateral orifice: Role of the bottom inclination versus friction. *Physical Review E*, 102(5):052902, 2020.

[186] Zhenhai Zou, Pierre Ruyer, P-Y Lagrée, and Pascale Aussillous. Nonsteady discharge of granular media from a silo driven by a pressurized gas. *Physical Review Fluids*, 7(6):064306, 2022.

[187] Iker Zuriguel, Angel Garcimartín, Diego Maza, Luis A Pugnaloni, and JM Pastor. Jamming during the discharge of granular matter from a silo. *Physical Review E*, 71(5):051303, 2005.